Physical constraints on the stratospheric injection of trace gases from wildfires

Simulation of the 2019/2020 Australian New Year event

Master's Thesis in
Physics
by

Tabea Unser

December 2024

INSTITUTE OF METEOROLOGY AND CLIMATE RESEARCH
KARLSRUHE INSTITUTE OF TECHNOLOGY (KIT)

Supervisor:	Prof. Dr. Corinna Hoose
Co-supervisor:	Prof. Dr. Peter Braesicke

Abstract

The Australian New Year (ANY) event refers to a time period during the 2019/2020 "Black Summer" wildfire season, when a particularly intense pyrocumulonimbus activity was recorded. This resulted in a direct injection of aerosols and chemical trace gases into the upper troposphere and lower stratosphere. Emissions at these heights enhance the lifetime of the aerosols and therefore enable long-range transport. Furthermore, they had profound impacts on Earth's radiation budget, stratospheric chemistry and local circulations.

Wildfires interact with the atmosphere in numerous ways. The sensible heat released by the fire creates buoyancy, which can enable pyrocumulus or pyrocumulonimbus formation. This strongly impacts the emission height and the subsequent transport of the emitted chemical tracers and aerosols. When it comes to modeling wildfire emissions, the injection height is a key parameter. In this study, the ICOsahedral Nonhydrostatic model with Aerosols and Reactive Trace gases (ICON-ART), which incorporates a so-called plume rise model, is used to simulate the fire emission height and transport for the extreme fire event ANY.

The simulation lasts for seven days starting on the December 29, 2019. In a first step, I try to reproduce the extreme plume injection heights that have been observed and are connected to extreme pyrocumulonimbus activity with a low-resolution global simulation in ICON-ART. To achieve larger injection heights of the plume, the sensible heat release by the fire is accounted for in the simulation and enhanced by a constant factor of 6.8 to match the plume heights observed with satellite instruments. CALIOP cross-sections indicate that plume signals around or above 15 km can only be reproduced when accounting for fire-induced sensible heat release. Furthermore, the plume and cloud top heights for this factor get closest to the maxima of the MODIS cloud top height.

The impact of aerosol-radiation interaction is investigated, especially with regard to the self-lofting effect which made the plume ascend for a longer time period after its injection. The self-lofting counteracts the sedimentation of the plume and enables it to rise to greater heights. The magnitude of the self-lofting is heavily influenced by the initial injection heights, as they determine whether the plume gets above cloud level or whether cirrus clouds can be located above them and inhibit warming by scattering solar radiation. Furthermore, the local temperature and vertical wind anomalies caused by the aerosol-radiation interaction are identified in the model data. A diurnal velocity variation of the self-lofting is found and an overall self-lofting rate of almost 500 m per day is derived.

For this thesis, the wildfire emission parameterization in ICON-ART, which currently only considers aerosols, is extended to include chemical trace gases. Therefore, it is now possible not only to simulate the impact of wildfire smoke on atmospheric chemistry but also to analyze the aging effect of aerosols. This permits tracking the transport of the plume by emitting CO and using a lifetime chemistry approach, which can, for example, be compared to IASI CO column load data or to timelines measured by MLS on several pressure levels. Another possibility is to emit more trace gases; these can react and impact the aerosol aging processes. The aerosol aging changes the optical properties; therefore, new optical properties are derived for the mixed soot particles. An

analysis of the aerosol aging finds a coating fraction of approximately 15% and a median diameter of 150 nm. These values are used to calculate the new optical properties, which lead to a slight reduction in self-lofting due to the aging.

Zusammenfassung

Das Australian New Year (ANY) Ereignis bezeichnet einen Zeitraum während der "Black Summer" Waldbrandsaison 2019/2020, in dem eine besonders intensive Pyrocumulonimbus-Aktivität aufgezeichnet wurde. Dies führte zu einer direkten Injektion von Aerosolen und chemischen Spurengasen in die obere Troposphäre und untere Stratosphäre. Emission in diesen Höhen verlängert die Lebensdauer der Aerosole und ermöglicht daher einen Transport über weite Strecken. Darüber hinaus hat sie tiefgreifende Auswirkungen auf das Strahlungsbudget der Erde, die Stratosphärenchemie und die lokalen Zirkulationen.

Waldbrände interagieren auf vielfältige Weise mit der Atmosphäre. Die durch das Feuer freigesetzte fühlbare Wärme erzeugt Auftrieb, der die Bildung von Pyrocumulus- oder Pyrocumulonimbuswolken ermöglichen kann. Dies beeinflusst stark die Emissionshöhe und den anschließenden Transport der emittierten chemischen Spurengase und Aerosole. Bei der Modellierung von Waldbrandemissionen ist die Injektionshöhe ein wichtiger Parameter. In dieser Arbeit wird das ICOsahedral Nonhydrostatic - Aerosols and Reactive Trace gases (ICON-ART) Modell, das ein sogenanntes Plume-Rise Modell beinhaltet, verwendet, um die Emissionshöhe des Feuers und den Transport für das extreme Feuerereignis ANY zu simulieren.

Die Simulation umfasst sieben Tage und beginnt am 29. Dezember 2019. In einem ersten Schritt versuche ich, die extremen Injektionshöhen der Rauchfahne, die beobachtet wurden und die mit extremer Pyrocumulonimbus-Aktivität verbunden sind, mit einer globalen Simulation in niedriger Auflösung in ICON-ART zu reproduzieren. Um größere Injektionshöhen der Rauchfahne zu erreichen, wird die durch das Feuer freigesetzte fühlbare Wärme in der Simulation berücksichtigt und um einen konstanten Faktor von 6,8 erhöht, um die mit Satelliteninstrumenten beobachteten Rauchfahnenhöhen zu erreichen. CALIOP-Querschnitte zeigen, dass Signale um oder über 15 km nur reproduziert werden können, wenn die durch das Feuer verursachte fühlbare Wärme berücksichtigt wird. Darüber hinaus kommen die Rauchfahnen- und Wolkenobergrenzen für diesen Faktor den Maxima der MODIS-Wolkenobergrenzen am nächsten.

Die Auswirkungen der Aerosol-Strahlungs-Wechselwirkung werden untersucht, besonders in Bezug auf den Selbstauftriebseffekt, der die Rauchfahne nach ihrer Injektion über einen längeren Zeitraum aufsteigen ließ. Der Selbstauftrieb wirkt der Sedimentation der Rauchfahne entgegen und ermöglicht es ihr, größere Höhen zu erreichen. Das Ausmaß des Selbstauftriebs wird stark von den anfänglichen Injektionshöhen beeinflusst, da sie bestimmen, ob die Rauchfahne über die Wolkenhöhe hinaus gelangt oder ob Cirruswolken darüber liegen und die Erwärmung durch Streuung des Sonnenlichts verhindern können. Darüber hinaus werden die lokalen Temperatur- und vertikalen Windanomalien, die durch die Aerosol-Strahlungs-Wechselwirkung verursacht werden, in den Modelldaten identifiziert. Eine tägliche Geschwindigkeitsschwankung des Selbstauftriebs wird identifiziert und eine Gesamtrate von fast 500 m pro Tag abgeleitet.

Für diese Arbeit wird die Waldbrandemissionsparametrisierung in ICON-ART, die derzeit nur Aerosole berücksichtigt, erweitert, um chemische Spurengase einzubeziehen. Daher ist es nun möglich, nicht nur die Auswirkungen des Rauchs auf die Atmosphärenchemie zu simulieren, sondern auch den Alterungseffekt von Aerosolen zu untersuchen. Dies ermöglicht das Verfolgen des Transports

der Rauchfahne durch die Emission von CO und die Verwendung einer Lifetime-Chemie, was beispielsweise mit IASI CO Column Load Daten oder mit Zeitreihen der Konzentrationen, die von MLS auf mehreren Druckniveaus gemessen wurden, verglichen werden kann. Eine weitere Möglichkeit besteht darin, mehr Spurengase zu emittieren; diese können reagieren und die Aerosolalterungsprozesse beeinflussen. Die Aerosolalterung verändert die optischen Eigenschaften, daher werden neue optische Eigenschaften für die gemischten Rußpartikel abgeleitet. Eine Untersuchung der Aerosolalterung ergibt einen Coating-Anteil von etwa 15% und einen Mediandurchmesser von 150 nm. Diese Werte werden verwendet, um die neuen optischen Eigenschaften zu berechnen, die zu einer leichten Reduktion des Selbstauftriebs aufgrund der Alterung führen.

Contents

1 Introduction

Wildfires are a natural part of functioning ecosystems worldwide (Bowman et al., 2009). Some wildfires develop from natural causes such as lightning strikes, while others are anthropogenic. Because wildfires vary strongly in their location and intensity, they are the largest contributor to short-term tropospheric composition variability (Voulgarakis et al., 2015). Emissions from wildfires make up a large part of the global aerosol burden. Wildfire particulate matter is an important pollutant and carries health risks (Cascio, 2018). It also impacts the Earth's energy balance due to aerosol-radiation and aerosol-cloud interactions (e.g. Morgan et al., 2006). Furthermore, wildfires emit chemical trace gases, for example carbon monoxide (CO), carbon dioxide (CO_2), methane (CH_4) and nitrogen oxides (NOx).
The Australian New Year (ANY) event was a particularly intense burning period during the extreme "Black Summer" wildfire season of 2019/2020, when record-breaking amounts of land were burned especially in southeastern Australia. The strong heat release and subsequent fire-induced convection transported the smoke plume to up to 16 km (Kablick et al., 2020), with pyrocumulonimbus (pyroCb) clouds forming due to moist convection. Due to self-lofting, the plume further ascended to an altitude of 35 km in 3 months (Khaykin et al., 2020). Consequently, dramatic changes occurred in many parts of the climate system, such as the radiative balance (Sellitto et al., 2022) and the stratospheric chemistry, with Bernath et al. (2022) linking the ANY event with ozone destruction. Due to its intensity and the magnitude of its impacts, ANY has been compared to moderate volcanic eruptions (Peterson et al., 2021). The topic of intense wildfires is only becoming more important in times of a changing climate, as Di Virgilio et al. (2019) expect a higher occurrence of pyroCb wildfires in Australia due to climate change.

To predict air quality degradation, changes in chemical composition and radiative properties due to smoke emissions, numerical weather modeling can be applied. However, the processes happen at different scales and they are difficult to be unified in one model system. The plume dynamic processes are complicated due to the many interactions between the fire, plume and atmosphere and they happen on a small scale. For example, Trentmann et al. (2006) use a horizontal resolution of ≈ 100 m to explicitly resolve them. The plume dynamic processes determine the initial injection height of the wildfire emissions, which in turn affects their atmospheric transport, lifetime and impacts (Val Martín et al., 2006). Most models have a too coarse grid spacing to resolve the processes. A parameterization, the plume-rise model, is then needed to derive the injection heights. Paugam et al. (2016) offers an overview of the different approaches that have been developed so far for this issue.
Accurate observation data about wildfires are needed as input data for plume-rise parameterizations, but also to verify the results produced by models. It is challenging to obtain such data because

wildfires have a high temporal and spatial variability. Satellite data can fill the gaps and provide information on the fires, such as their location, timing and intensity (Kaiser et al., 2012). Satellites can also be used to obtain many different types of information about the plumes that originate from wildfires, such as their aerosol and trace gas concentrations, their location or height. However, they also have significant issues, such as limited overpass times or that wildfire plumes are often masked by clouds. Therefore, the retrieved parameters are associated with large uncertainties.

Several studies point to the self-lofting of the ANY plume without explaining the detailed processes, such as the connection between the initial injection height and the subsequent self-lofting or the impact of aerosol aging. The goal of this thesis is therefore to further investigate the different processes that transported the plume of the 2019/2020 Australian wildfires to the large heights that were observed. The ANY event is modeled with ICON-ART in a setup that makes use of a plume rise model implementation by Walter et al. (2016) in COSMO-ART based on Freitas et al. (2006). Val Martin et al. (2012) showed that the Freitas plume rise model was not able to reproduce plume heights that were measured by the Multi-angle Imaging Spectroradiometer (MISR), generally underestimating the heights. The issue has already been investigated in Muth (2024) at regional scale (with 6.5 km horizontal resolution) by accounting for fire-induced sensible heat release. This thesis aims to show how the sensible heat release translates to global scale (with 50-100 km horizontal resolution). In its current implementation in ICON-ART, the plume rise model can only emit aerosols in the form of soot. However, as outlined, fires also emit a variety of trace gases that impact not only atmospheric chemistry but also aerosol aging. To account for this, the emission of chemical trace gases is implemented in ICON-ART.
The thesis aims to answer the following research questions:

1. How can the extreme injection heights of the 2019/2020 ANY event be reached with the plume rise model in low-resolution simulations?

2. How large is the impact of aerosol-radiation interaction for the further transport of the smoke plume in the simulation and can a realistic self-lofting rate be produced?

3. How does the emission of chemical trace gases and subsequent aerosol aging influence the optical properties and, as a result, the self-lofting?

In this context, several comparisons to satellite data will be performed to verify the results.
The thesis is structured in the following way. In the second chapter, the theoretical background will be outlined, with a more general discussion about aerosols and the interactions between wildfires and the atmosphere through their aerosol and chemical trace gas emissions. Chapter 3 gives an overview of the ANY event and its impacts. In the fourth chapter, the ICON-ART model is described along with its plume rise implementation, and the simulation setup is explained together with the changes that were made to the model. In the two subsequent chapters, the results of the experiments are described and discussed with regard to the research questions. Lastly, the work is concluded in chapter 7 and an outlook is given.

2 Theoretical background

2.1 Atmospheric aerosols

Aerosols are an important part of the atmosphere and have a large impact on weather and climate processes, but also air quality. They form when small liquid or solid particles are suspended in air. Aerosols originate from a variety of different sources that can be natural or anthropogenic. Primary aerosols are directly emitted, whereas secondary aerosols form from precursor gases that have transformed to the liquid or solid phase (Raes et al., 2000).
Due to their wide range of sizes, it would be very complex to keep track of the diameters of the many particles an aerosol system contains, such that simplifications are needed. One possibility is to divide the particle size range into discrete sections and calculate the histogram, but this leads to a loss of information about the distribution within each bin (Seinfeld and Pandis, 2016). Another way is to approximate the aerosol size distribution by lognormal distributions that depend on the median diameter d_{pm} and the geometric standard deviation σ_{g}. The three moments of the lognormal distribution function describe the aerosol number, surface and volume (mass) distributions, respectively.
Distinct size ranges can be differentiated, they are then represented each by their own distribution or mode. Whitby (1978) divides aerosol sizes into three modes. With ascending particle diameter, there is the Aitken mode at 0.01 µm to 0.1 µm, the accumulation mode at 0.1 µm to 2.5 µm and the coarse mode at >2.5 µm (Seinfeld and Pandis, 2016). While Aitken and accumulation mode dominate the aerosol number concentration, the accumulation and coarse mode dominate the aerosol mass. Aerosols can be externally or internally mixed. Internal mixing means that the aerosol particles themselves are a combination of different chemical species. An externally mixed aerosol is made up of particles that belong to different species but that are themselves chemically pure (Boucher, 2015).

2.1.1 Aerosol microphysics

The properties of the aerosols such as their concentration, composition, size and morphology can change due to aerosol microphysics. These chemical and physical processes contribute to the aging of aerosol particles. Sometimes, they are more effective for particular size ranges (Seinfeld and Pandis, 2016). An overview of such processes is given in Figure 2.1.
Several trace gases can transform into aerosols after chemical reactions and subsequent nucleation. Nucleation means that new aerosol particles are produced from a clustering of molecules that were originally in the gas phase. From a particular size called the critical size, the cluster is stable

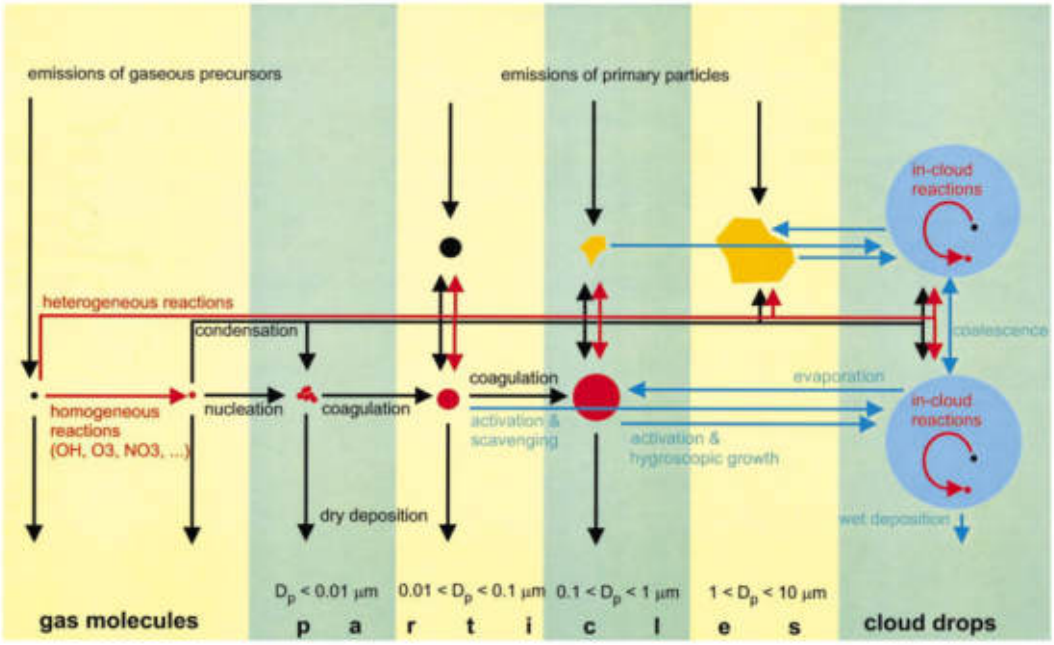

Figure 2.1: Illustration of aerosol microphysical processes that have an impact on the size distribution and chemical composition (Raes et al., 2000).

because its rate of growth then equals its rate of decay (Seinfeld and Pandis, 2016). Typically, nucleation results in very small aerosols.

In addition, chemical trace gases can modify existing aerosols by transforming from the gaseous to the liquid phase on their surfaces, which is called condensation. Condensation leads to an increase in the diameter of the original aerosol particle and changes to the particle size and mass distributions. For example, a soluble shell may form around the insoluble core of aerosol particles. The aerosol is then considered internally mixed. For both condensation and nucleation, the gas phase species involved needs to be supersaturated (Boucher, 2015).

A further process to be considered is coagulation, the process that describes two particles that stick together after colliding. The reason for the particles coming into contact can either be their Brownian motion, or a motion that is a result of external forces, for example due to gravitational settling (Seinfeld and Pandis, 2016). The higher the concentration of an aerosol, the higher is the probability for a collision. After their contact, the particles form a new, larger particle.

Particles in the accumulation mode tend to have the longest lifetimes in the atmosphere (Seinfeld and Pandis, 2016). Small particles tend to be transferred to the accumulation mode by coagulation and condensation processes, whereas large particles are more likely to be removed from the atmosphere by washout and sedimentation processes.

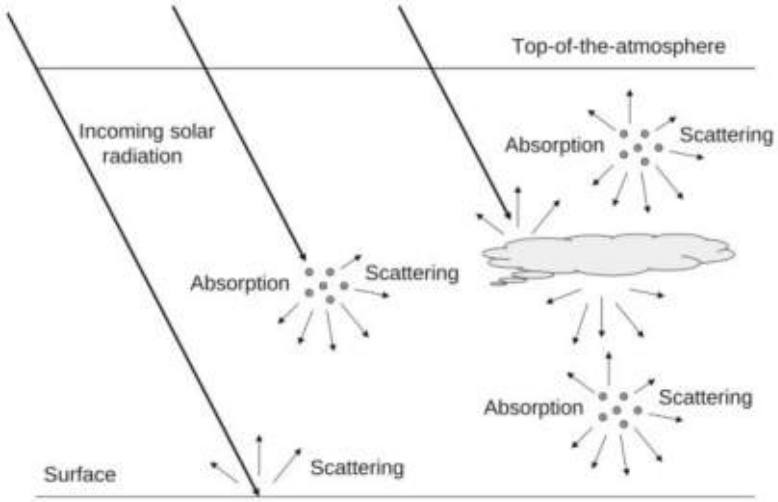

Figure 2.2: Overview of direct aerosol-radiation interactions. Aerosols can absorb solar radiation or scatter it in all directions. Depending on the solar zenith angle, the altitude, local surface properties and the location of clouds, the amount and properties of the radiation that interacts with the aerosols varies (Boucher, 2015).

2.1.2 Aerosol-radiation interactions

Atmospheric radiation is usually divided into long- and shortwave radiation. The incoming solar radiation predominantly contains short wavelengths, whereas the outgoing radiation from the Earth due to thermal emission is mostly long-wave. When radiation hits matter, it can be scattered, reflected or absorbed. Scattering means that the radiative energy is sent back into all directions. Absorption and scattering together are called extinction and can be quantified for an aerosol by its mass extinction coefficient k. The relationship between scattering and absorption is given by the single scattering albedo (SSA) ω, which is defined as the ratio between the scattering and the extinction efficiency σ

$$\omega = \frac{\sigma_{\text{sca}}}{\sigma_{\text{ext}}}. \tag{2.1}$$

The asymmetry factor g is the mean of the cosine of the scattering-angle weighted by the scattered intensity at a particular angle $P(\theta)$ (Seinfeld and Pandis, 2016)

$$g = \frac{1}{2}\int_0^{\pi} \cos\theta P(\theta)\sin\theta \mathrm{d}\theta. \tag{2.2}$$

g has a value of 1 if the light is scattered entirely in the forward direction, -1 for the backward direction and 0 if the light is scattered isotropically.

The size, shape and composition of aerosols determine these optical properties and, as a result, how they interact with radiation. This is why aerosol aging significantly alters the optical properties of aerosols, which affects their radiative effects. According to Jacobson (2000), particles with a highly absorptive core exhibit a higher absorption when surrounded by a less absorptive shell compared to the same components being externally mixed. The reason for this is that the coating increases the core absorption cross section by focusing the photons onto the core, which is called the lensing effect.

Aerosol-radiation interactions describe processes by which aerosols affect the radiation balance of the Earth and, as a result, either cool or warm the atmosphere. Direct, semi-direct and indirect effects are differentiated. An aerosol layer can prevent parts of the solar radiation from reaching the Earth surface by scattering it back up, cooling the surface as a consequence. Figuratively speaking, the aerosol layer casts a shadow on the Earth. This is called the **direct effect** of aerosols on atmospheric radiation. As Figure 2.2 illustrates, the direct radiative effect of aerosols is also influenced by how many clouds are present and where they are located (Chand et al., 2009).
When absorbed, the radiation is transformed into thermal energy in the particle, warming the aerosol layer. This is the aerosol **semidirect effect** (Hansen et al., 1997). Local warming due to absorbing aerosols can lead to cloud evaporation and a reduction in cloud cover, but also change the atmospheric stability. Depending on the vertical distribution of the absorbing aerosols, the radiative heating may lead to an increase or decrease in cloud thickness (Koch and Del Genio, 2010). The sign and extent of the semidirect effects varies a lot between different estimates (Morgan et al., 2006).
The **indirect effects** further influence the radiation budget by aerosols seeding clouds (Lohmann and Feichter, 2005). If more aerosols are present to act as cloud condensation nuclei (CNN) or ice nuclei (IN), overall more cloud droplets or ice particles can form. If the same water amount inside the cloud is distributed among more droplets, their diameter becomes smaller. This has several consequences. First, clouds with more and smaller droplets appear brighter because they reflect more light. This is called the cloud albedo or Twomey effect (Twomey, 1974). Furthermore, the precipitation efficiency is reduced for smaller droplets. This increases their residence time in the atmosphere and prolongs cloud lifetime, which is called the cloud lifetime effect (Albrecht, 1989).

2.2 Interactions between wildfires and the atmosphere

The term "biomass burning" describes combustion processes of living or dead vegetation. In this thesis, the discussion of biomass burning is limited to wildfires. In contrast for example to prescribed burning, which is used as a forest management tool (Morgan et al., 2020), wildfires are forest fires that are unpredictable and uncontrolled.
The combustion depends on many factors, which results in a high complexity and a high spatiotemporal variability of the associated processes. Wildfires occur when four preconditions are met (Bradstock, 2010): First, there needs to be enough combustible material available. Secondly, the combustible material needs to be sufficiently dry, which makes it easier to ignite. Furthermore, favorable meteorological conditions that favor fire spread ("fire weather") are required, for example strong winds or low humidity. Finally, it takes an ignition cause, which can be either natural (e.g. lightnings) or anthropogenic (e.g. arson or accidents). A different combination of these factors leads to different combustion products. Often, many distinct biomass burning processes happen in close proximity under various circumstances, with several vegetation types and fuels being distributed over the burning area.
The combustion occurs in three phases. In the ignition phase, only small pieces of vegetation combust, heating up larger pieces in their environment. This enables the ignition for larger vegetation pieces, as the water vapor they contain evaporates. During the flaming phase, larger pieces of vegetation are burned and the gases that originate from the solid fuels react with surrounding O_2 (Akagi et al., 2011). Later, when most volatiles have exited the fuel, smoldering combustion becomes more important. This process is slower and generally happens at lower temperatures (Akagi et al., 2011).
The emissions that originate from wildfires impact many atmospheric processes, via aerosol-radiation and aerosol-cloud interactions, but also chemical reactions. To understand the impacts in detail, knowing the composition of wildfire smoke is important.

2.2.1 Emission of chemical trace gases

Organic material generally consists of carbon bonds. During the combustion process, they react with the oxygen. Combustion processes can be complete or incomplete. A complete combustion primarily produces carbon dioxide (CO_2) and water (H_2O). For incomplete combustion, several further chemical species are produced. The percentages of complete and incomplete combustion are quantified in the combustion efficiency, which is defined as the fraction of fuel carbon which is converted to carbon in CO_2. The combustion efficiency increases when the contribution of flaming compared to smoldering combustion grows (Akagi et al., 2011). Due to the inhomogeneity of the fire and the complex reaction chains, it is generally difficult to determine the exact percentages of any combustion products.
Carbon monoxide (CO) forms after an incomplete combustion of carbon containing compounds. It is a toxic, colorless gas with a relatively short average lifetime in the troposphere of around 30-90 days. As a consequence, it usually has quite low background concentrations, with mixing ratios in the troposphere ranging between 40 and 200 ppb (Seinfeld and Pandis, 2016). After large wildfires,

elevated concentrations of CO can be observed in the smoke area (Edwards et al., 2006). With less anthropogenic sources than in the Northern hemisphere, CO emissions in the Southern hemisphere are dominated by biogenic sources and biomass burning (Fisher et al., 2015).
Other gaseous compounds that are emitted from wildfires include methane (CH_4), nitric oxide (NO) and volatile organic compounds (VOCs). Further chemical reactions can produce additional trace gases. Nitrogen dioxide (NO_2) is emitted in small amounts compared to NO during combustion processes, but a larger part is formed when NO is oxidized in the atmosphere (Seinfeld and Pandis, 2016). The sum of $NO + NO_2$ is often denoted by NO_x. When CH_4 and non-methane VOCs are oxidized, CO can be formed from secondary organic production and add to the concentrations that are directly emitted from the fire. Besides, NO_x, CO, CH_4 and VOCs contribute to tropospheric ozone (O_3) production through photochemical reactions. Jaffe and Wigder (2012) estimate that 3.5% of global tropospheric O_3 production can be attributed to wildfire emissions. At elevated concentrations, O_3 can have harmful effects on respiratory health and impact plant growth.
For more extreme wildfire events, the perturbations in atmospheric chemistry due to smoke emissions are not limited to the troposphere. In the stratosphere, wildfire events have been linked to ozone loss (Bernath et al., 2022). With climate change increasing the risk for extreme wildfire events (Di Virgilio et al., 2019), they can possibly delay the recovery of the stratospheric ozone.

2.2.2 Emission of aerosols

The carbon that remains from the combustion processes stays in the form of soot. Seinfeld and Pandis (2016) define soot as clusters of carbon particles that originate from incomplete combustion of carbonaceous material. According to Reid et al. (2005), organic carbon (OC), a mixture of pure carbon with several organic compounds, makes up around 80% of the mass of fresh dry soot particles. Only around 5-9% of the mass is pure elemental or black carbon (BC). The rest is trace inorganic species, which account for 12-15% of the mass.
Aerosol composition strongly affects its optical properties and radiative impacts. As its name indicates, black carbon has a high absorptivity for both long- and shortwave radiation and is a strong warming radiative forcing agent (Thornhill et al., 2021). Despite being present only at a small percentage, BC significantly influences the absorption properties of wildfire smoke. The higher the BC fraction, the more solar radiation is absorbed by the plume. For this reason, the BC/OC ratio is commonly used to describe the aerosol optical properties (Novakov et al., 2005).
Several trace gases originate from wildfires that can contribute to aerosol aging or form secondary aerosol particles themselves. Wildfires have been connected to elevated concentrations of sulfur dioxide (SO_2), which produces sulfate (SO_4^{2-}) or nitrogen oxides (NO_x) that transform into nitrates (NO_3^-) via a reaction with OH (e.g. Rickly et al., 2022; Campbell et al., 2022). The sulfates, nitrates, but also ammonia (from NH_3) and organics (from hydrocarbons and VOCs) are then available to nucleate and form liquid aerosol particles or to condensate onto preexisting particles.

2.2.3 Vertical transport of wildfire plumes

The impact of wildfire smoke emissions on the atmosphere also depends on the height at which they are released. The transport of a smoke plume up to the upper troposphere - lower stratosphere (UTLS) region during extreme wildfire events is a complicated process where many different factors need to be taken into consideration. However, two main mechanisms that can cause the plume to reach the UTLS can be distinguished: pyroCb convection and self-lofting. Both need to be correctly represented in the model in order to get the smoke transport right.

Uplift due to heat release

The heat flux generated by wildfires is influenced by factors such as fuel load, fuel water content and weather conditions. Generally, wildfires release substantial amounts of heat, causing the resulting plumes to be significantly warmer than their environment. This is particularly true for larger, intense fires. The temperature difference between the plume and the ambient air creates an updraft due to positive buoyancy. According to Viegas (1998), the definition of the buoyancy flux F is

$$F = \frac{gR}{c_{\mathrm{p}} p_0} Q_{\mathrm{c}} \tag{2.3}$$

with the gravity constant g, the ideal gas constant R, the heat capacity at constant pressure c_{p}, the ambient surface pressure p_0 and the convective heat flux Q_{c}. In many large-scale models, the convective and the radiative heat flux are related with a constant factor (e.g. Freitas et al., 2007) that has been derived experimentally. The quantitative information of the buoyancy flux can be used to derive further information on the plume dynamics.

As shown in Figure 2.3, the plume dynamics depend not only on the heat from the fire, but also on environmental conditions such as temperature, thermodynamic stability, humidity and horizontal wind speed (Kahn et al., 2007). The atmospheric stability influences the buoyancy of the plume. As the plume rises, it interacts with the surrounding atmosphere. The fire size determines the surface area of the plume where this interaction happens (Freitas et al., 2007). At the edge of the plume, turbulent mixing occurs with the colder ambient air, which increases the radius of the plume and dilutes it, thereby reducing the buoyancy (Freitas et al., 2006). Strong winds can even bend the smoke plume and inhibit further ascend.

Within the plume, gases and aerosols are carried upward into the atmosphere. Initially, this transport typically happens semi-vertically or vertically. Afterwards, the smoke tends to accumulate in layers of relative stability (Kahn et al., 2007). The injection height has a strong impact on how the biomass burning emissions are transported further. Its value depends on the plume dynamics that have been described above. Advection away from the source region happens faster for pollutants that reach elevated altitudes, where winds speeds are higher. Furthermore, the aerosol lifetime depends on the height at which they are released. In lower altitudes within the boundary layer, they are more efficiently removed. For these reasons, injection heights in the free troposphere enable atmospheric transport of several hundreds or thousands of kilometers (Val Martín et al., 2006).

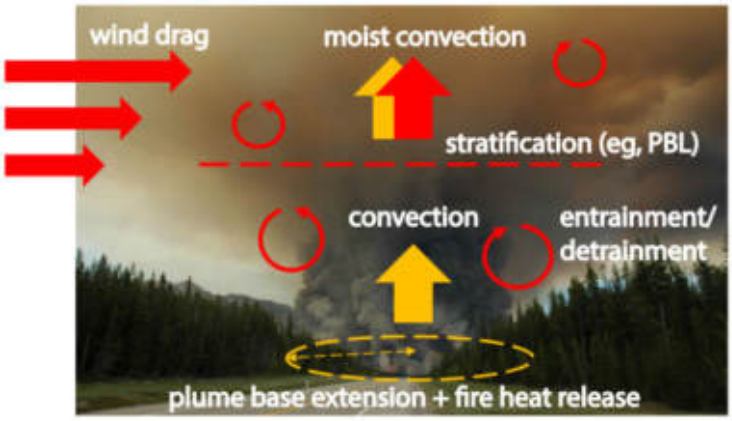

Figure 2.3: Illustration of processes that are relevant for fire plume dynamics. Atmospheric processes are marked with red, fire processes with yellow colors (Paugam et al., 2016).

Pyrocumulonimbus injection

The plume often transports moisture, which either originates from the combustion itself or which is entrained from the surrounding air (Trentmann et al., 2006). In case of condensation, sensible heat is released and clouds form. Because the heat release from the wildfires can trigger convection at locations where such strong convection would not occur normally, the uplift process is also called pyroconvection and the resulting clouds are called pyrocumulus or pyrocumulonimbus (pyroCb) clouds. PyroCb clouds are a specific type of thunderstorm cloud which appears over sources of extreme heat and under favorable atmospheric conditions. Often, they are smoke-infused. PyroCbs typically form in an anvil shape over the heat source and they contain elevated concentrations of small cloud droplets and ice particles due to the smoke supplying large amounts of cloud condensation nuclei (CCN) and ice nuclei (IN) (Rosenfeld et al., 2007). These distributions towards smaller sizes prevent precipitation and reduce scavenging of the smoke from the air. Therefore, most of the smoke particles are transported up efficiently and are exhausted into high altitudes from the cloud top.

The latent heat release and additional energy which is released during the ice formation further enforce the updraft. Tarshish and Romps (2022) showed that dry firestorm plumes originating from nuclear blast simulations are not able to reach the stratosphere and that only the latent heat release enables this ascent. In extreme cases, the updraft velocities can reach up to $58\,\mathrm{m\,s^{-1}}$ (Rodriguez et al., 2020). In conclusion, pyrocumulonimbus (pyroCb) activity offers an efficient pathway to transport the smoke to the UTLS quickly. Due to its intensity, it has been compared to an explosive volcanic eruption (Peterson et al., 2018).

Apart from the size and intensity of the fire itself, certain meteorological conditions favor pyroCb formation. In order to achieve the necessary fire activity for pyroCb development, dry and hot air is needed near the surface. However, midtropospheric moisture is required for condensation and latent heat release to occur in the rising smoke plume (Peterson et al., 2017). Furthermore, an unstable lower atmosphere (Kahn et al., 2007) and an approaching cold front (Luderer et al., 2006) have been attributed to pyroCb development. As a consequence of some of these conditions, pyroCb development is favored during local afternoon. At this time, the surface temperature and

sensible heat from fires reach their respective maxima. Furthermore, strong surface winds favor fire spread and the increased atmospheric instability during daytime enhances the pyroconvective processes. Reaching the stratosphere becomes most probable for smoke plumes that originate from several large wildfires closely together that each produce intense convective updrafts at similar times (Peterson et al., 2018).

Self-Lofting

As has already been mentioned, BC is highly absorbing in the shortwave wavelength range. The absorption can cause self-lofting effects on the plume. This generally works in the following way: Incoming solar radiation hits the smoke plume. A part of the radiation might be scattered, but a large portion is absorbed by the smoke plume, heating it up. The heating creates instability and the plume begins to move upward, this movement is called self-lofting (Radke et al., 1990).
The self-lofting rate, or the velocity of the upward movement for the smoke plume, depends on several factors (Boers et al., 2010; Ohneiser et al., 2023). First, the vertical potential temperature gradient plays a crucial role, because the temperature contrast against the atmospheric background is what drives the upward movement. Furthermore, the aerosol optical properties and the aerosol concentration within the plume determine the amount of radiation absorbed, which contributes to the warming.
The self-lofting rate depends on the incoming solar radiation, which is in turn affected by clouds. Due to their high albedo, clouds reflect solar radiation very effectively. For thin smoke layers above clouds, this leads to a part of the radiation passing the aerosol layer twice. This is the reason why the lofting rate above clouds is increased by about 70% (Ohneiser et al., 2023). Conversely, when the clouds are above the smoke plume they may prevent a large part of the solar radiation from reaching it.
The lofting rate can be written as (Holton, 2004)

$$\frac{\mathrm{d}z}{\mathrm{d}t} = \frac{\Theta}{T\Gamma} \cdot \frac{\mathrm{d}T}{\mathrm{d}t} \tag{2.4}$$

with the potential temperature Θ, the potential temperature gradient Γ, the temperature T and the heating rate $\frac{\mathrm{d}T}{\mathrm{d}t}$. Self-lofting generally becomes faster at greater heights both in the troposphere and in the stratosphere, because the heating rate increases exponentially with height, as less dense air can be heated up more efficiently (Ohneiser et al., 2023). However, there is a lofting inhibition at the tropopause level which slows down or may even stop the self-lofting of smoke plumes. Ohneiser et al. (2023) explain this in the following way: The heating rate in the troposphere is low compared to that in the stratosphere. In the troposphere, the potential temperature gradient Γ by which the heating rate is divided in Equation 2.4 is also low. Therefore, even weak heating rates enable smoke lofting in the troposphere. In the upper troposphere (3-4 km below the tropopause in the case of Ohneiser et al. (2023)), the potential temperature gradient grows more quickly than the heating rate with height. This slows down the lofting speed, which reaches its minimum close to the tropopause. If the plume passes above the tropopause, the heating rate increases further until it dominates the lofting rate, even if the potential temperature gradient in the stratosphere is enhanced as well.

In general, it is important to note that ascent time due to self-lofting is of the order of days for smoke injection heights of 2-6 km to reach the tropopause (Ohneiser et al., 2023). For example, in Boers et al. (2010), the plume is lifted by 3-5 km in 3 days. Self-lofting is thus much slower than ascent due to pyroCb activity, where transport from the near-surface to the tropopause is in the order of 1 h). However, it persists for a longer time period than the pyroCb injection and permits smoke plumes to reach even greater heights after their initial injection. In fact, pyroCb convection is not always needed for intense smoke plumes to reach the tropopause. It has been shown that, in principle, self-lofting alone is capable of transporting them from an injection height in the lower or middle free troposphere to this height (Ohneiser et al., 2023). For plumes that have already reached the stratosphere, self-lofting increases their residence time there by counteracting the sedimentation and removal of the aerosols (Ohneiser et al., 2022).

3 The 2019/2020 Australian New Year Event

3.1 Background: The 2019/20 Australian wildfire season

The term "bushfire" is commonly used for wildfires that occur in Australia. Wildfires are a natural part of the Australian ecosystem (Bowman et al., 2009). In terms of vegetation, grassy fuels dominate for the entire continent, especially in the savannas in northern Australia. In southeastern Australia, the vegetation is dominated by forests that mainly contain eucalyptus trees. In this region, wildfires occur less regularly than for example in northern Australia but generally more intensely. The "Black Summer" wildfire season of 2019/2020 profoundly impacted the forests of Southeastern

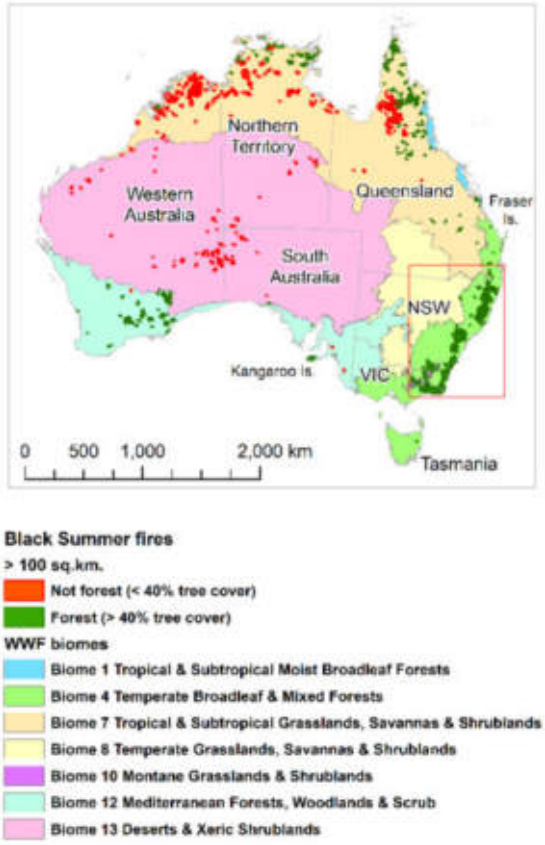

Figure 3.1: Map of "Black Summer" fires between September 2019 and mid-February 2020. The points in green and red colors indicate forest and non-forest fires which are differentiated based on tree cover. Additionally, the biomes that occur in Australia are shown (Levin et al., 2021).

Figure 3.2: Carbon aerosol emissions for different bushfire seasons in Southeastern Australia, accumulated over the entire season (September-March) and calculated based on data from the global fire assimilation system (GFAS, Kaiser et al. (2012)), image from Heinold et al. (2022).

Australia (see Figure 3.1). This fire season was unprecedented in terms of size, intensity, and impacts. Prolonged dry conditions rendered these regions particularly susceptible to wildfires, resulting in widespread outbreaks across several states and territories. In New South Wales and Victoria, 5.8 million ha were burned between September 2019 and early January 2020, which corresponds to 21% of the Australian temperate forest biome (Boer et al., 2020). During this time period, almost twice the area was burned compared to previous extreme fire events on record in Australia (Heinold et al., 2022; Morgan et al., 2020). The eucalyptus forests affected by the fires likely exacerbated their severity, since they favor a more rapid fire ignition and spread (Murphy et al., 2013). Figure 3.2 shows how much the aerosol emissions accumulated over this season differ from previous fire seasons.

3.2 Development and characteristics of the Australian New Year Event

The Australian New Year (ANY) event, which was part of the Australian Black Summer, was a phase of particularly strong pyroCb activity and was therefore termed a pyroCb "super outbreak". The ANY event also lasted for an unusually long time. In total, 38 individual pyroCb pulses were recorded (Peterson et al., 2021) that developed each over a respective group of intense wildfires. Figure 3.3 shows a map of the blow-up fires in southeastern Australia that contributed to the ANY event and, in comparison, to the entire 2019/20 wildfire season.

The event can be divided into two phases, with the first between the 29th and 31st December 2019 and the second on the 4th January 2020. In between, there were three days without pyroCb activity. The first phase is quite extraordinary for its overall duration of around 45 h (Peterson et al., 2021). There was intense pyroCb activity during nighttime, which is not typical for these events (see 2.2.3). 33 distinct pyroCb pulses were recorded, and all of them injected smoke into the UTLS. The activity maximum was reached on 30th December 2019, where the pyroCb activity extended over an entire 24 h period. The second ANY phase had more blow-up fires overall, but less pyroCb activity, with only five additional pulses. Additionally, its duration of only around six hours was

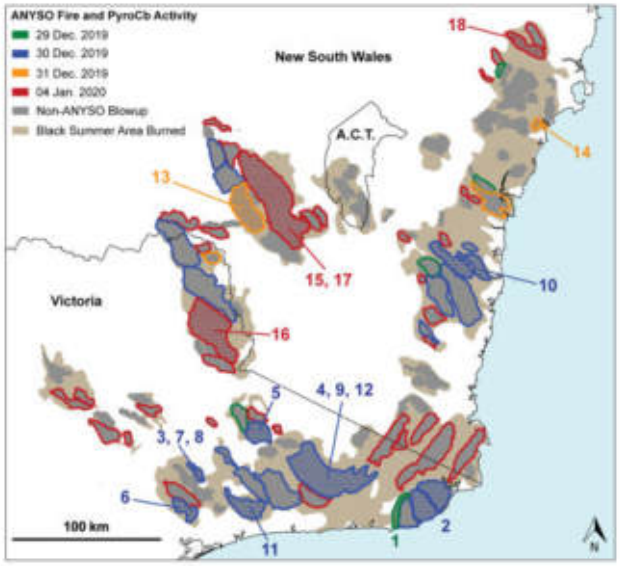

Figure 3.3: Map of the fires in southeastern Australia that contributed to the pyroCb activity during the ANY event color-coded by the date at which they occurred. The numbers correspond to the order of 18 pyroCb sub-events during ANY that the 38 pyroCb pulses can be grouped into. The total area burned during the 2019/2020 "Black Summer" fire season is indicated by light brown shadings (Peterson et al., 2021).

more typical for this type of event. Peterson et al. (2021) estimate the stratospheric smoke injection for the first phase to $0.2-0.8\,\mathrm{Tg}$ and to $0.1-0.3\,\mathrm{Tg}$ for the second phase.

3.3 Atmospheric Impacts

The pyroCb events during ANY injected smoke into the UTLS region, to heights of up to 16 km (Kablick et al., 2020). The great emission heights enabled the smoke to remain airborne for longer time periods and to be transported farther. Due to self-lofting, the ANY plume reached even greater heights well after its injection into the atmosphere (Ohneiser et al., 2023). Furthermore, the absorptive heating caused the formation of a quasi-ellipsoidal anticyclonic vortex that confined trace gases and aerosols within. This preserved the compactness of the smoke plume, which made it ascend more quickly (Khaykin et al., 2020). The plumes that originated from the ANY event travelled 66 000 km and reached heights of up to 35 km altitude in the stratosphere after 3 months (Khaykin et al., 2020).

Due to the smoke injection into high altitudes, the stratospheric aerosol optical depth (AOD) in the southern extratropics tripled (Khaykin et al., 2020). The stratospheric smoke concentrations beat the previous record from the Pacific Northwest Event (PNE) that was caused by intense wildfires in western North America in 2017 (Peterson et al., 2018). Sellitto et al. (2022) estimate the area-weighted global-equivalent clear-sky radiative forcing (RF) for the 2019/20 Australian wildfires to be in the range of $-0.35 \pm 0.21\,\mathrm{W\,m^{-2}}$ at the top of the atmosphere and $-0.94 \pm 0.26\,\mathrm{W\,m^{-2}}$ for the surface. The forest vegetation in Australia includes many oil-containing eucalyptus trees, which might have enhanced its BC fraction compared to plumes originating from other regions and, as a consequence, made it more absorptive (Ohneiser et al., 2022).

Furthermore, chemical trace gases were emitted, several of which had an impact on stratospheric ozone loss (Bernath et al., 2022). Trace gases such as CO, hydrogen cyanide (HCN) and VOCs were detected in connection to the fires (Kloss et al., 2021).

3.4 Satellite observations of the Australian New Year event

The ANY event was observed using several satellite instruments. In this thesis, retrievals from IASI, MLS, CALIOP and MODIS will be used to validate and compare model results.

To verify the position and development of the CO distribution, its column load can be compared with several satellite retrievals. One such possibility is the Infrared Atmospheric Sounding Interferometer (IASI) onboard the Meteorological Operational (MetOp) satellite (Clerbaux et al., 2009). This instrument measures outgoing infrared radiation from the Earth surface with a Fourier transform spectrometer between wavelengths of 3.62 µm to 15.5 µm to observe chemical species such as CO, SO_2 and O_3. IASI offers a global coverage of the Earth's surface twice a day, with its pixels having a diameter of around 12 km on the ground at nadir.

The Microwave Limb Sounder (MLS) is operated onboard the Aura satellite (Waters et al., 2006). This instrument measures mixing ratio profiles of chemical species such as CO, H_2O, HCN, N_2O, OH and O_3 in the high atmosphere. Its vertical resolution is 1.5 km in the altitude range from 5 to 120 km. The satellite is polar-orbiting and sun-synchronous, such that it always performs measurements at the same two local times for any given latitude. This makes it possible that it misses events with a short duration and limited spatial extent.

The Cloud-Aerosol Lidar with Orthogonal Polarization (CALIOP) onboard the CALIPSO satellite (Winker et al., 2009), which is part of the A-train satellite constellation, is commonly used to estimate plume heights. It collects attenuated backscatter signals at 532 nm and 1064 nm wavelength on a 70 m wide ground track and provides a height profile from the results. CALIOP offers a high vertical resolution that ranges between 30 and 300 m depending on the altitude, but its narrow ground track limits the amount of plume observations. Additionally, it can classify the signals into different aerosol categories based on their depolarization ratio. Here, the total attenuated backscatter profiles at 532 nm are used for comparison with the model data.

The Moderate Resolution Imaging Spectroradiometer (MODIS) is a sensor operated on the Aqua and Terra satellites that covers the spectral range of 0.42 µm to 14.24 µm. In this thesis, MODIS cloud top height data is used for comparison with simulation data. The MODIS cloud top height product is derived using an algorithm that applies a CO_2-slicing method and it has a spatial resolution of 1 km (Baum et al., 2012).

4 Model description

Numerical weather modeling aims to establish a system of differential equations that describe the physical, meteorological and chemical laws governing the atmosphere. By solving these equations numerically for each time step and grid point, statements about future developments of the atmosphere and its components can be made. To achieve this, a temporal and spatial numerical discretization is required. Ideally, the equations would be solved for as many points in space and time as possible to resolve all the processes that happen in the atmosphere. In reality, this is limited by computation resources which makes it necessary to represent unresolved processes with parameterizations. Recent advancements in computational power enable to represent increasingly complex processes in models, leading to improvements in weather predictions.
For this thesis, the ICON-ART model system is used to model the aerosols and chemical tracers that are emitted by wildfires. In this chapter, the ICON-ART model system is described.

4.1 The ICON Modelling Framework

The ICOsahedral Nonhydrostatic (ICON) modelling framework (Zängl et al., 2015) has been developed by the German Weather Service, Deutscher Wetterdienst (DWD) together with the Max Planck Institute for Meteorology (MPI-M), the German Climate Computing Center (DKRZ), the Karlsruhe Institute of Technology (KIT) and the Center for Climate Systems Modeling (C2SM). It is suitable for both global Numerical Weather Prediction (NWP) and climate modelling. Since 2016, ICON is operational in DWD's forecast system. This chapter aims to give a very short overview based on Zängl et al. (2015), where a more detailed description can be found.
Weather models need a grid to divide the continuous space of the atmosphere into discrete sections. In contrast to previous models which apply longitude-latitude grids, ICON uses an icosahedral-triangular C grid. An icosahedron is a platonic body that consists of 20 equilateral triangles. A longitude-latitude grid has numerical stability issues because the meridians converge in the pole regions and cause singularities. For a triangular grid, this is not the case.
To create this grid, the spherical icosahedron is taken as a basis, it is placed around the Earth and projected onto the Earth surface. Afterwards, differently sized grids can be produced by subsequently dividing its spherical triangles. The grids are given a name RnBk based on how many times the original icosahedron needs to be divided to get a certain grid. The process works as follows: First, the edges of the initial spherical icosahedron are divided via root division into n sections of the same length. By connecting the new triangle corners, n^2 equilateral triangles are produced inside each of the old triangles. Then, k further edge bisections are performed,

Table 4.1: Number of cells, number of edges and effective grid resolution of some global grids commonly used with ICON, based on Zängl et al. (2015) (adapted)

Grid	Number of cells	Number of edges	Effective grid resolution (km)
R2B04	20480	30720	157.8
R2B05	81920	122880	78.9
R2B06	327680	491520	39.5
R2B07	1310720	1966080	19.7

dividing each triangle into four smaller triangles per step. The resulting number of cells n_{cell} can be calculated from n and k with

$$n_{\text{cell}} = 20n^2 \cdot 4^k. \tag{4.1}$$

This process creates different grid resolutions for different RnBk grids. The effective grid resolution $\overline{\Delta x}$ is

$$\overline{\Delta x} = \sqrt{\overline{A_{\text{cell}}}} = \sqrt{\frac{\pi}{5}} \frac{r_{\text{Earth}}}{n\,2^k} \tag{4.2}$$

with the average cell area A_{cell} and the Earth's radius r_{Earth}. Table 4.1 contains some examples for common global grids and their properties.
The vertical direction of the grid is obtained by adding other horizontal grids on top. The lower vertical levels follow the terrain more closely, but higher levels gradually become constant height levels (Weimer et al., 2017).

ICON has some important advantages compared to pre-existing global models. First, it has better conservation properties, with an exact local mass conservation and mass-consistent transport. Furthermore, it offers a better scalability when used in future parallel high-performance computing architectures. The model uses a non-hydrostatic dynamical core. This permits to apply the model not only to global, but also to regional scales with grid sizes where the hydrostatic approximation is not valid anymore. By avoiding the use of the hydrostatic approximation, overall consistency over different scales is improved.
ICON aims to solve the following equation system based on the prognostic variables suggested by Gassmann and Herzog (2008):

$$\frac{\partial \hat{v}_{\text{n}}}{\partial t} + \frac{\partial \hat{K}_{\text{h}}}{\partial n} + (\hat{\zeta} + f)\hat{v}_{\text{t}} + \hat{w}\frac{\partial \hat{v}_{\text{n}}}{\partial z} = -c_{\text{pd}}\hat{\theta}_{\text{v}}\frac{\partial \overline{\pi}}{\partial n} - F(\hat{v}_{\text{n}}) \tag{4.3}$$

$$\frac{\partial \hat{w}}{\partial t} + \hat{\mathbf{v}}_{\mathbf{h}} \cdot \nabla \hat{w} + \hat{w}\frac{\partial \hat{w}}{\partial z} = -c_{\text{pd}}\hat{\theta}_{\text{v}}\frac{\partial \overline{\pi}}{\partial z} - g - F(\hat{w}) \tag{4.4}$$

$$\frac{\partial \overline{\rho}\hat{\theta}_{\text{v}}}{\partial t} + \nabla \cdot (\overline{\rho}\hat{\mathbf{v}}\hat{\theta}_{\text{v}}) = \overline{Q} - F(\hat{\theta}_{\text{v}}) \tag{4.5}$$

$$\frac{\partial \overline{\rho}}{\partial t} + \nabla \cdot (\overline{\rho}\hat{\mathbf{v}}) = 0 \tag{4.6}$$

$$\frac{\partial \overline{\rho}\hat{q}_{\text{k}}}{\partial t} + \nabla \cdot (\overline{\rho}\hat{q}_{\text{k}}\hat{\mathbf{v}}) = -\nabla \cdot (\overline{\mathbf{J}}_{\text{k}} + \overline{\rho q_{\text{k}}'' \mathbf{v}''}) + \overline{\sigma}_{\text{k}}. \tag{4.7}$$

This formulation uses Hesselberg averaging, where a field ϕ is divided into the barycentric mean with respect to the air density ρ,

$$\widehat{\phi} = \frac{\overline{\rho\phi}}{\overline{\rho}} \tag{4.8}$$

and the fluctuation ϕ'' such that

$$\phi = \hat{\phi} + \phi''. \tag{4.9}$$

$\overline{\phi}$ is the Reynolds average $\phi = \overline{\phi} + \phi'$. Equation 4.3 and Equation 4.4 are the horizontal and vertical momentum equation, respectively. Equation 4.5 is the first law of thermodynamics, Equation 4.6 the continuity equation and Equation 4.7 the continuity equation of the constituents.
The prognostic variables in ICON are the horizontal wind velocity component normal to the triangle edges $\hat{v}_\mathrm{n}$, the vertical wind component $\hat{w}$, the air density $\hat{\rho}$ and the virtual potential temperature $\hat{\theta}_\mathrm{v}$. The three-dimensional wind vector $\hat{\mathbf{v}}$ consists of the tangential wind component $\hat{v}_\mathrm{t}$, $\hat{v}_\mathrm{n}$, and $\hat{w}$, which form a right-handed system $(\hat{v}_\mathrm{t}, \hat{v}_\mathrm{n}, \hat{w})$ together. The horizontal wind-vector is represented by $\hat{\mathbf{v}}_\mathbf{h}$. Furthermore, there is the vertical vorticity component $\hat{\zeta}$, the Coriolis parameter f, the horizontal part of the kinetic energy $\hat{K}_h = \frac{1}{2}(\hat{v}_\mathrm{n}^2 + \hat{v}_\mathrm{t}^2)$, the specific heat capacities of dry air at constant pressure or constant volume c_pd and c_vd and the gravitational constant g. The Exner function $\overline{\pi}$ is defined as

$$\pi = \left(\frac{R_\mathrm{d}}{p_{00}}\rho\theta_\mathrm{v}\right)^{R_\mathrm{d}/c_\mathrm{vd}} \tag{4.10}$$

with the gas constant of dry air R_d and the reference pressure at 1000 hPa p_{00}. Additionally, $F(\hat{v}_\mathrm{n})$, $F(\hat{w})$ and $F(\hat{\theta}_\mathrm{v})$ are turbulent momentum fluxes and $\overline{Q}$ is a source term for diabatic heat. $\frac{\partial}{\partial n}$ is the horizontal edge-normal derivative.

4.2 The ART Module

The Aerosol and Reactive Trace gases (ART) extension to the ICON model is developed at the Institute of Meteorology and Climate Research at KIT in cooperation with the DWD. It permits to simulate the spatiotemporal evolution of aerosols and trace gases and to understand their interaction with the atmosphere online in a numerical weather prediction model (Rieger et al., 2015; Schröter et al., 2018).
ART is included into ICON with interface modules that are part of the ART code. Inside these modules, routines are called which belong to the ART code. The process order is visualized in Figure 4.1. During one time integration process, many different processes need to be calculated and all of them influence the atmospheric state, such as emission, advection, sedimentation, deposition, washout, chemical reactions and subscale vertical convective transport. In ICON-ART, the processes are calculated subsequently. For the time integration process in ICON, dynamics and then tracer advection are called first. In between, the ART processes start by calculating aerosol and trace gas emissions, which are then added to the tracers that are advected within the ICON tracer framework. Furthermore, the sedimentation is calculated. The processes thereafter are divided based on whether they are calculated for each time step (fast physics) or only after longer time periods (slow physics). ICON contributes for example turbulent diffusion and microphysics to the fast physics processes, and ART includes deposition, washout and chemical reactions. Convection, radiation and gravity wave drag belong to the slow physics processes.
The scalability of ICON is preserved for ICON-ART (Rieger et al., 2015). In the case that ART is not used, the integration ensures that ICON can be used without it being affected.

4.2.1 Basic equations

This section, which aims to present the basic equation in ICON-ART, is based on Rieger et al. (2015). By applying Reynolds and Hesselberg averaging, the time derivative can be written as

$$\frac{\widehat{\mathrm{d}}}{\mathrm{d}t} = \frac{\partial}{\partial t} + \widehat{\mathbf{v}} \cdot \nabla \tag{4.11}$$

with the barycentric mean velocity $\widehat{\mathbf{v}}$ and the continuity equation becomes

$$\frac{\widehat{\mathrm{d}\overline{\rho}}}{\mathrm{d}t} = -\overline{\rho} \nabla \cdot \widehat{\mathbf{v}}. \tag{4.12}$$

Ψ is a mass-specific variable and it can take different forms:
For **gaseous tracers**, $\Psi_{\mathrm{g,l}}$ is the mass mixing ratio of a gas l, defined as the ratio of the partial density of l and the total density. Its barycentric mean $\widehat{\Psi_{\mathrm{g,l}}}$ is then

$$\widehat{\Psi_{\mathrm{g,l}}} = \frac{\overline{\rho_{\mathrm{l}}}}{\overline{\rho}}. \tag{4.13}$$

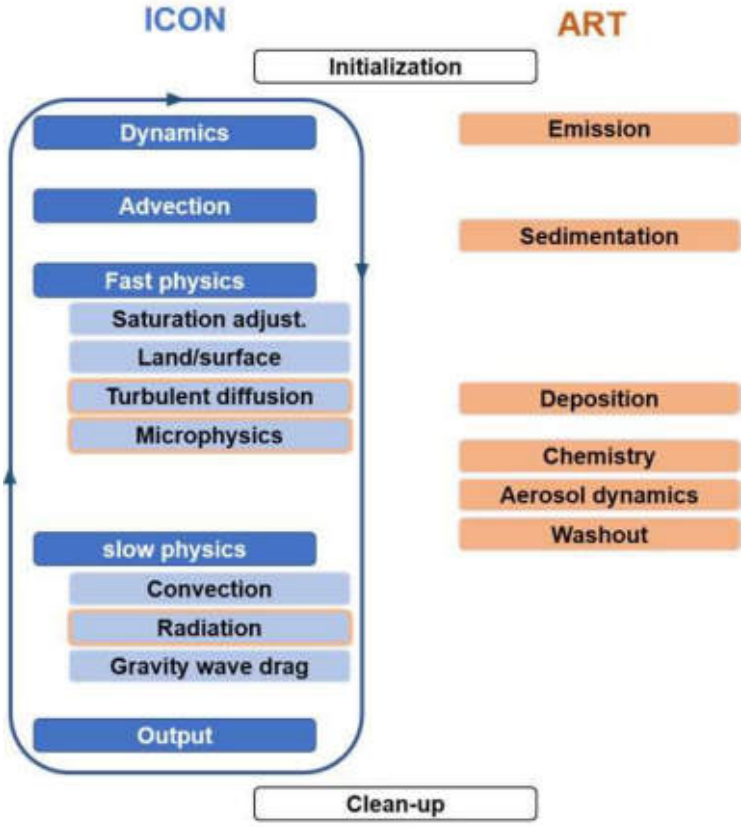

Figure 4.1: Illustration of the coupling between ICON and ART. ICON processes are represented by blue boxes, ART processes by orange boxes. Orange frames around blue boxes mean that ART tracers are treated inside an ICON tracer framework (Rieger et al., 2015, modified).

The flux form of the spatiotemporal evolution of gaseous tracers can be derived with Equation 4.11 and Equation 4.12

$$\frac{\partial(\overline{\rho}\widehat{\Psi_{g,l}})}{\partial t} = -\nabla\cdot(\widehat{\mathbf{v}\rho}\widehat{\Psi_{g,l}}) - \nabla\cdot\overline{(\rho\mathbf{v}''\Psi''_{g,l})} + P_l - L_l + E_l. \tag{4.14}$$

$\nabla\cdot\overline{(\rho\mathbf{v}''\Psi''_{g,l})}$ represents turbulent fluxes, which are included in ICON with a one-dimensional prognostic turbulent kinetic energy (TKE) scheme (Raschendorfer, 2001). $\nabla\cdot(\widehat{\mathbf{v}\rho}\widehat{\Psi_{g,l}})$ is the flux divergence. It contains the horizontal and vertical advection of the gaseous compound. P_l is the production rate and L_l the loss rate due to chemical reactions, emissions are given by E_l.

For **polydisperse aerosols**, several different lognormally distributed modes are used to represent them. The relevant moments that are used to calculate the barycentric mean are the specific number $\widehat{\Psi_{0,l}}$ and the mass mixing ratio $\widehat{\Psi_{3,l}}$

$$\widehat{\Psi_{0,l}} = \frac{\overline{N_l}}{\overline{\rho}} \tag{4.15}$$

$$\widehat{\Psi_{3,l}} = \frac{\overline{M_l}}{\overline{\rho}} \tag{4.16}$$

with the number concentration N_l and the mass concentration M_l. The prognostic equations (without aerosol dynamics processes) are then:

$$\frac{\partial(\widehat{\overline{\rho}\Psi_{0,l}})}{\partial t} = -\nabla\cdot(\widehat{\mathbf{v}\overline{\rho}\Psi_{0,l}}) - \nabla\cdot\overline{(\rho\mathbf{v}''\Psi''_{0,l})} + \frac{\partial}{\partial z}(v_{\text{sed},0,l}\widehat{\overline{\rho}\Psi_{0,l}}) - W_{0,l} + E_{0,l} \tag{4.17}$$

$$\frac{\partial(\widehat{\overline{\rho}\Psi_{3,l}})}{\partial t} = -\nabla\cdot(\widehat{\mathbf{v}\overline{\rho}\Psi_{3,l}}) - \nabla\cdot\overline{(\rho\mathbf{v}''\Psi''_{3,l})} + \frac{\partial}{\partial z}(v_{\text{sed},3,l}\widehat{\overline{\rho}\Psi_{3,l}}) - W_{3,l} + E_{3,l} \tag{4.18}$$

with the sedimentation velocities $v_{\text{sed},0,l}$ and $v_{\text{sed},3,l}$, the loss of particles (mass) due to below-cloud scavenging $W_{0,l}$ ($W_{3,l}$) and the number (mass) emission flux of mode l $E_{0,l}$ ($E_{3,l}$).
The emission term plays an important role for chemical trace gases and aerosols and it needs to be parameterized. Sedimentation is treated as an additional vertical advection, but its vertical velocity $v_{\text{sed},l}$ can only take a direction downward. Depending on whether the aerosol is monodisperse or polydisperse, different parameterizations of washout are used.

4.2.2 Representation of aerosol dynamics

In ICON-ART, the module AERODYN (AEROsol DYNamics) is used to calculate the aerosol microphysics. This section will cover the most important points based on Muser et al. (2020).
In contrast to the three modes that were already mentioned in 2.1 (Aitken, accumulation and coarse mode), AERODYN uses four modes with an additional giant mode for especially large particles. The modes are further divided into insoluble, soluble and mixed modes. The mixed mode contains particles that have an insoluble core with a soluble shell. Figure 4.2 provides an overview of the different species and modes that are covered by AERODYN. Via several processes such as condensation and coagulation, aerosols can shift from one mode to another.
To model this, AERODYN solves the prognostic equations for the number density and mass concentration for each mode whilst keeping the standard deviations constant:

$$\frac{\partial}{\partial t}M_{0,i} = -\text{Ca}_{0,ii} - \text{Ca}_{0,ij} + \text{Nu}_0 \tag{4.19}$$

$$\frac{\partial}{\partial t}M_{3,i} = -\text{Ca}_{3,ij} - \text{Co}_{3,i} + \text{Nu}_3 \tag{4.20}$$

with the number density $M_{0,i}$ and the mass concentration $M_{3,i}$ of mode i, intra- and intermodal coagulation in the moment m $\text{Ca}_{m,ii}$ and $\text{Ca}_{m,ij}$, condensation Co and nucleation Nu. AERODYN calculates the nucleation, condensation and coagulation, but it does not take into account every mode for each process to save computing power. For example, nucleation is assumed to only be relevant for the Aitken mode. When particles shift modes, they either shift into a larger mode when a threshold diameter is exceeded, or they shift from insoluble to mixed modes when the mass of a soluble coating exceeds a threshold.
To determine how species are partitioned onto the liquid or gaseous phases in thermal equilibrium, the extension ISORROPIA II (Fountoukis and Nenes, 2007) is coupled with ICON-ART. ISORROPIA is an thermal equilibrium model which treats inorganic aerosol species, more specifically the thermodynamics of K^+, Ca^{2+}, Mg^{2+}, NH_4^+, Na^+, SO_4^{2-}, NO_3^-, Cl^- and H_2O.

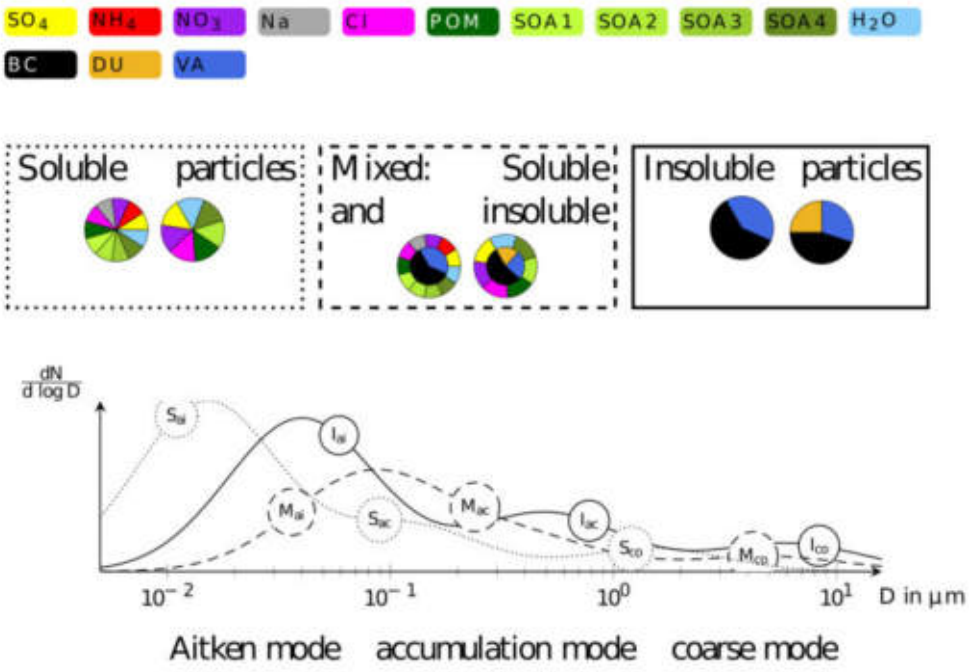

Figure 4.2: Top: Different components of soluble (first row) and insoluble (second row) aerosol modes. Middle: mixing states for the different modes. Bottom: Particle size distributions for all modes except the giant mode and for soluble (dotted line), mixed (dashed line) and insoluble (solid line) particles. POM: primary organic matter, SOA: secondary organic aerosol, BC: black carbon, DU: desert dust, VA: volcanic ash (Muser et al., 2020).

4.2.3 Aerosol optical properties

Accurately simulating energy flows due to radiation is a crucial part of weather modelling. As radiation travels vertically through the entire atmosphere, the optical properties of the surface and of various atmospheric components, such as gases, aerosols and clouds need to be taken into consideration. NWP models employ radiative transfer models to calculate radiation exchanges in the atmosphere. They parameterize the optical properties for the different components and apply a radiation solver to determine how the radiation travels through the optical medium. In ICON, different radiation schemes are available. The standard radiation scheme ecRad (Hogan and Bozzo, 2018) is used in this thesis.

The optical properties of aerosols depend on the wavelength. To account for the aerosol effect on radiation, the local radiative transfer parameters are therefore calculated for every mode i in 30 wavelength bands between 0.2 and 1000 µm. Out of the 30 bands, 16 are in the longwave spectrum and 14 are in the shortwave spectrum. The radiative transfer parameters are the mass extinction coefficient k_i, the single scattering albedo ω_i and the asymmetry parameter g_i. For the calculations, the aerosol mass concentrations and their optical properties are needed at every grid point. The optical properties are obtained offline from Mie calculations and they are then directly provided to the radiation scheme. Mie theory assumes perfectly spherical particles, which only reflects reality to a limited extent.

All optical properties are provided to the radiation solver inside ecRad, which calculates the reflection, transmission and internal radiation sources for each grid box and model level. This

results in the upward and downward radiation fluxes. Additionally, it computes the radiative heating and cooling, which in turn influences the dynamics and physics.

4.2.4 Representation of chemistry

ICON-ART distinguishes two different types of tracers, passive and chemically active tracers (Schröter et al., 2018). Passive tracers do not interact with other tracers and only change due to transport, they also have a theoretically infinite lifetime because they have no losses. Chemically active tracers interact and even participate in feedback processes. They experience source and loss processes and, as a consequence, have a limited lifetime.
In Schröter et al. (2018), a full gas-phase chemistry approach is described, utilizing the MECCA module (Module Efficiently Calculating the Chemistry of the Atmosphere). Because this approach is quite complicated and uses many equations, simplifications are often applied. One such simplified approach is to use the lifetime to derive an idealized loss rate of a chemical species. The lifetime-based chemistry is described in Rieger et al. (2015).
In Weimer et al. (2017), another simplified approach is described. There, the lifetime is no longer constant, but it is calculated based on reactions involving the hydroxyl (OH) radical, which is one of the most important reactants in the atmosphere. In the troposphere, it is produced by photolytic destruction of O_3, which produces an oxygen atom in an excited state $O(^1D)$. The $O(^1D)$ is either quenched by colliding with N_2 or O_2 or it reacts with H_2O and produces OH (Jacob, 1986):

$$\begin{aligned}
O_3 + h\nu &\xrightarrow{J_{O_3}} O(^1D) + O_2, \\
N_2 + O(^1D) &\xrightarrow{k_{N_2}} O(^3P) + N_2, \\
O_2 + O(^1D) &\xrightarrow{k_{O_2}} O(^3P) + O_2, \\
H_2O + O(^1D) &\xrightarrow{k_{H_2O}} 2\,OH
\end{aligned}$$

with the reaction rate k and the photolysis rate J. The main sinks for OH are reactions with CH_4 and CO (Jacob, 1986),

$$\begin{aligned}
OH + CH_4 &\xrightarrow{k_{CH_4}} H_2O + CH_3, \\
&\longrightarrow \ldots \longrightarrow CO + HO_2, \\
OH + CO &\xrightarrow{M,\,k_{CO,1}} H + CO_2, \\
OH + CO &\xrightarrow{M,\,k_{CO,2}} HOCO.
\end{aligned}$$

The OH number concentration then follows as

$$[OH] = \frac{2\,[O(^1D)]\,k_{H_2O}\,[H_2O]}{k_{CH_4}\,[CH_4] + (k_{CO,1} + k_{CO,2})\,[CO]} \tag{4.21}$$

with the concentration of O(^{1}D)

$$[\mathrm{O}(^1\mathrm{D})] = \frac{J_{\mathrm{O}_3}[\mathrm{O}_3]}{k_{\mathrm{O}_2}[\mathrm{O}_2] + k_{\mathrm{N}_2}[\mathrm{N}_2] + k_{\mathrm{H}_2\mathrm{O}}[\mathrm{H}_2\mathrm{O}]}. \tag{4.22}$$

Because this chemistry mechanism overestimates the OH concentration for the stratosphere, different parameterizations of the lifetime need to be used there (Weimer et al., 2017). For the ozone chemistry, the linearized ozone chemistry (LINOZ) can be used (McLinden et al., 2000). It is a first-order Taylor expansion which linearizes the ozone concentration tendency with respect to the local ozone mixing ratio ξ, the temperature of the grid box T and the density of the ozone column above the point which is considered c_{O_3}:

$$\frac{\mathrm{d}\xi}{\mathrm{d}t} = (P-L)^0 + \left.\frac{\partial(P-L)}{\partial\xi}\right|_0 (\xi - \xi^0) + \left.\frac{\partial(P-L)}{\partial T}\right|_0 (T - T^0) + \left.\frac{\partial(P-L)}{\partial c_{\mathrm{O}_3}}\right|_0 (c - c^0_{\mathrm{O}_3}). \tag{4.23}$$

The ozone tendency $(P-L)$ is represented by the difference between the production P and the loss term L. The superscript ^{0} indicates climatological values and the subscript $_0$ the evaluation of a partial derivative at the climatological value. LINOZ is only applied at heights above 10 km.

4.3 Treatment of biomass burning in ICON-ART

The simulation of biomass burning emission requires information on the location, time and the emission strength to correctly capture the transport. To get this information, ICON-ART uses the Global Fire Assimilation System (GFAS), which is described in the following.

4.3.1 The Global Fire Assimilation System

The Global Fire Assimilation System (GFAS) (Kaiser et al., 2012) contains information on emissions originating from biomass burning. They are calculated based on the Fire Radiative Power (FRP) observed by the Moderate Resolution Imaging Spectroradiometer (MODIS), onboard the polar orbiting satellites Aqua and Terra. The FRP quantifies how much thermal radiation a fire releases. The FRP (in units of Watt) is measured for each satellite pixel. The GFAS filters out false observations, for example from volcanic or industrial sources. If gaps occur because of clouds covering the area, it fills them with a Kalman filter. Furthermore, a land fraction mask is used to account for errors introduced by water bodies.
The FRP is then used to derive the combustion rate of the fires with land-cover specific conversion factors. Different emission factors for specific fuel types represent the mass of an emission type (for example CO, BC,...) per mass of combusted fuel. They permit to calculate various emission fluxes (in $\mathrm{kg\,m^{-2}\,s^{-1}}$) from the combustion rate. The accuracy of the emission factor may vary for different species, depending on how much data is available about them.
The emission estimates are available for a global longitude-latitude grid with a 0.5° resolution. The temporal resolution of the FRP is limited to one day because MODIS is on board of polar-orbiting and not geostationary satellites and therefore each instrument only performs one to two measurements per grid cell per day. For this reason, GFAS uses the daily FRP mean value of these measurements and does not provide any information on its diurnal cycle.
MODIS FRP measurements are only reliable for cloud-free regions. Convective clouds often at least partially obscure the satellite view onto the fires, for an example of this see Figure 4.3. Kaiser et al. (2012) apply an enhancement factor of 3.4 to the organic matter and BC emissions to better match their global distribution to reality.

4.3.2 The plume rise model

The plume rise parameterization that is used in ICON-ART is based on Freitas et al. (2006) and Freitas et al. (2007). It is implemented analogous to how Walter et al. (2016) implemented it in COSMO-ART. Its goal is to include the sub-grid vertical transport of aerosols and trace gases to models that do not have a resolution high enough to resolve it explicitly. The plume rise parameterization is best applicable for low-resolution atmospheric transport models. In this case, the assumption that the fires do not significantly influence the dynamics and thermodynamics at the larger scale is valid (Freitas et al., 2006). The remaining way in which they influence the atmospheric state is then solely via the emissions that they cause.

Figure 4.3: MODIS image of southeastern Australia and New Zealand for the 31st December 2019. Fires and thermal anomalies that were detected by MODIS onboard Aqua are marked by orange dots. A mixture of clouds and smoke is visible originating from ANY fires which had their intensity maximum the day before (NASA Worldview Snapshot, ESDIS)

The plume rise model does not take the entire fire dynamics into consideration, Freitas et al. (2006) rather identify the additional heat flux at the ground caused by the fire as a crucial parameter for plume rise. With the values for fire size (to estimate the plume radius) and total fire heat flux, the plume rise model derives the initial buoyancy. Because the heat flux depends on the vegetation type, the information about the fire location are combined with a land-use dataset to divide the fires into three categories: forest, woody savanna and grassland. For each category, the heat flux is assigned an upper and a lower value, as shown in Table 4.2. This range of fire intensity values is justified by the variability of the combustion process itself. A maximum fire size of 50 ha that they reach during their peak activity throughout the day is assigned to each fire (Walter et al., 2016).

Table 4.2: Lower and upper heat flux bounds for different vegetation types, adapted from Freitas et al. (2006)

Biome type	Lower bound [$\mathrm{kW\,m^{-2}}$]	Upper bound [$\mathrm{kW\,m^{-2}}$]
Tropical forest	30.	80.
Woody savanna	4.4	23.
Grassland, pasture, cropland	3.3	-

Diurnal cycle

As has already been described, the conditions at daytime such as reduced surface humidity and higher wind speeds favor wildfire development. To reflect this diurnal cycle with peak emissions in the early afternoon between 10:00 and 15:00 local time and minimum emissions at night, a weighted normal distribution can be used:

$$d(t_1) = w + \frac{1}{\sigma\sqrt{2\pi}} \exp\left(-\frac{1}{2}\left(\frac{t_1 - t_0}{\sigma}\right)^2\right). \tag{4.24}$$

w is a weighting which depends on the vegetation type, because for each vegetation type the percentage which is burnt during peak fire activity differs. For forests, the weighting is set to

$w = 0.039$, for savannas $w = 0.018$ and for grasslands $w = 0.003$. Furthermore, t_1 is the local solar time, $t_0 = 12.5$ is the expected value of maximum emission and $\sigma = 2.5$ is the standard deviation. The emissions during an hour are kept constant. The diurnal cycle can be applied to the values of fire intensity, fire size and emission that the plume rise model uses. Because the total daily emissions are known, the diurnal cycle for the emissions is normalized with its sum, whereas the fire intensity and size diurnal cycles are normalized with their respective maxima.
This step incorporates the diurnal cycle into the calculation of aerosol and trace gas emissions at specific heights and times, transforming previously constant parameters into time-dependent ones.

Plume height and vertical emission distribution

Grid points where the soot emission flux is above a threshold of $0.005 \cdot 10^{-9}\,\mathrm{kg\,s^{-1}}$ are identified as active fires and the plume rise parameterization is switched on for them. The plume rise model then calculates the upper and lower bounds of the plume and its resulting one-dimensional vertical distribution for the respective grid point.
The general outline is the following (Freitas et al., 2006, 2007; Walter et al., 2016): A one-dimensional box model is embedded into the columns of the large-scale model. In the vertical direction, this 1D plume rise model has 200 layers with a grid spacing of 100 m. The large-scale model passes the environmental conditions to the plume rise model for every grid point with an active fire. The plume rise model needs the heat fluxes, the fire sizes, the emission fluxes and the meteorological conditions (T, p, u, v and q_v) as input parameters. The maximum plume height is set to where the vertical velocity w is below $1\,\mathrm{m\,s^{-1}}$. 100 m is set as a minimum thickness of the plume. When the calculations are done, the plume rise model returns the upper and lower limits of the plume to the host model.
In the vertical direction, the emission distribution is represented by a parabola between the upper and lower bounds of the emission layer (Walter et al., 2016)

$$f(z^*) = 6z^* \cdot (1 - z^*) \tag{4.25}$$

with the dimensionless height z^*

$$z^* = \frac{z - z_\mathrm{bot}}{z_\mathrm{top} - z_\mathrm{bot}}. \tag{4.26}$$

z is the model layer height, z_top and z_bot are the upper and lower bounds of the plume. As a consequence, for points inside the plume z^* can only have values in the interval $[0,1]$. The emissions from each grid cell k can be obtained by integrating over the emission profile f from the lower to the upper limit of the grid cell, under the condition that the grid cell is inside the plume. Outside of the plume, so for z^* outside of the interval $[0,1]$, there are no emissions. In conclusion, the emission weighting function $W_\mathrm{emis,k}(z^*)$ for a specific grid cell is then

$$W_\mathrm{emis,k}(z^*) = \begin{cases} \int_{z^*_\mathrm{bot,k}}^{z^*_\mathrm{top,k}} f(z^*)\mathrm{d}z^* & \text{if } 0 < z^* < 1 \\ 0 & \text{else.} \end{cases} \tag{4.27}$$

The total emissions from a grid cell k are obtained via the integration from the lower z^*_{lolev} to the upper grid cell level z^*_{uplev}: The vertical emission distribution for a species s and grid cell k follows then as

$$E_{\text{s,k}} = F_{\text{s}} \cdot W_{\text{emis,k}} \cdot d_{\text{emis}} \cdot \frac{1}{\Delta z} \tag{4.28}$$

with the total emission flux F_{s} of the species s, the diurnal cycle of the emission d_{emis} and the vertical layer thickness Δz.

4.4 Modifications in ICON-ART

4.4.1 Emission of chemical trace gases

At present, the plume rise model in ICON-ART only emits aerosols in the form of soot. To be able to investigate chemical trace gases, it is necessary to add their emission to the plume rise model. To achieve this, a strategy was applied similar to the already existing soot emission mechanism. In the following, the soot emission flux denotes the sum of the BC and OC emission fluxes which are emitted together. However, the emission fluxes are imported not only for the soot, but also for the chemical trace gases that are emitted. In the scope of this thesis, these are CO, CH_4, NH_3, SO_2 and NO_2. All these gases except for NO_2 are available within the GFAS dataset. NO_2 is derived from the NO_x emission flux in GFAS with the assumption $NO_2 = 0.75 \cdot NO_x$, as for example in Schreier et al. (2014).
For the same grid points where soot is emitted (where the soot emission flux values are above $0.005 \cdot 10^{-9}\ \mathrm{kg\,s^{-1}}$), the chemical trace gases can be emitted as well. Using the same plume rise calculation, their emission profile is derived. Subsequently, the emission values are added to the respective chemical trace gas concentrations.
As described in subsection 4.3.1, Kaiser et al. (2012) applied an enhancement factor of 3.4 to soot emissions. Muth (2024) confirmed that this enhancement factor improves the model-observation comparison. Consequently, the same factor was applied in our simulations, however not only to the soot emissions, but also to the chemical trace gases.

4.4.2 Additional sensible heat release

Furthermore, an additional sensible heat release term sh_{fire} from Muth (2024) was added. sh_{fire} is derived from the FRP, which can be read into ICON from the GFAS dataset. Since the FRP represents the radiative fraction of the total heat release, it is multiplied by 10 to convert it into the total energy which is released by the fire, then it is multiplied by 0.55 to convert the total energy to the convective energy. Furthermore, the diurnal cycle $d(t)$ is applied to the heat flux in $\mathrm{W\,m^{-2}}$,

$$sh_{\mathrm{Fire}} = \mathrm{FRP} \cdot 10 \cdot 0.55 \cdot d(t). \tag{4.29}$$

Lastly, the sh_{fire} is added to the surface sensible heat flux that is calculated in ICON.

4.5 Simulation setup

For the simulations, a global setup with approximately 80 km grid spacing is run on a R02B05 ICON grid. The runs start on the 29th December 2019 at 00:00 UTC and continue for seven days until the 5th January 2020 at 00:00 UTC. The simulations therefore cover both phases of the ANY event. The runs are initialized for the 29th December with DWD analysis data.
For the emission data, GFAS retrievals are used (CAMS, 2021). To make it easier to track the fire plumes and to not have emissions from fires outside Australia interfering with the results, emissions are only enabled for the Australian region. To achieve this, emissions outside Australia are set to zero in the GFAS data. Then, the emission data is interpolated onto the model grid using conservative remapping (Jones, 1999). This is a method where the integral of the original data field is preserved across the remapping. When tested against other remapping methods, conservative remapping preserved the spatial distribution of the fires in comparison to the original, unremapped data best. Afterwards, the GFAS data is read into ICON-ART for each day separately. The soot, again defined as the sum of OC and BC, is emitted only into the insoluble accumulation mode with a median number diameter of $d_n = 70\,\text{nm}$ and a standard deviation of $\sigma = 2$. The optical properties of the insoluble accumulation mode are taken from Muth (2024).
The chemical trace gas values for the 29th December are initialized with CAM-chem data (Buchholz et al., 2019; Emmons et al., 2020) to ensure that there are already elevated background values present at the beginning of the simulation. The initialization is performed for all gases that are emitted in the respective setup (see below). This is especially important since the ANY event was already preceded by a season of extremely high wildfire activity and thus, elevated background values for example in CO.

Two different kinds of simulations are performed:
At first, the simulations are conducted without aerosol aging, which means no condensation, no coagulation and no nucleation. In addition to soot, only CO is emitted to track the emissions, their height and transport. The CO is initialized with CAM-chem data and its decay is calculated using the lifetime chemistry approach.
In another simulation, the aerosol aging is enabled. To achieve this, further chemical trace gases are emitted (CO, CH_4, NH_3, SO_2 and NO_2) and undergo chemical reactions via the OH-chemistry. Above 10 km, the LINOZ chemistry is applied. Nucleation is enabled for SO_4; condensation, coagulation and ISORROPIA are switched on.

5 Validation of the simulation data

5.1 Validating the injection heights

The first objective is to validate injection heights with the ICON-ART simulation setup. Studies like Val Martin et al. (2012) have shown that plume rise models cannot reproduce injection heights reliably. For extreme fires there is a systematical underestimation. This issue is addressed by Muth (2024), primarily through the development of the sensible heat release term. In that study, a limited area was simulated for almost three days with a high resolution of around 6.6 km. Extending this work, the simulations presented here are global and utilize a much coarser grid. This chapter will evaluate how well the sensible heat release term translates to these coarser resolutions.
This section focuses on the sensible heat release term and its role in achieving realistic injection heights. The impact of aerosol-radiation-interaction (ARI) and the self-lofting effect will be addressed in the subsequent chapter. The experiments discussed in the following sections were conducted with the setup without aerosol aging. They differ in terms of their application of the wildfire sensible heat release. The different experiments are denoted by the abbreviations which are outlined in Table 5.1. The abbreviation SHFL is used for simulations where the additional sensible heat release from Muth (2024) is activated. Additionally, multiplying sh_{fire} with an enhancement factor was tested. In a first approach, the factor 3.4 was used because this is the assumed underestimation of the GFAS for soot emission (Kaiser et al., 2012). If we assume that this factor is needed due to an underestimation of the FRP in GFAS, the factor would apply to both the sensible heat release term and the soot emission flux as they are proportional to the FRP. For another experiment, the factor was doubled to a value of 6.8 to investigate a larger enhancement.
All output is interpolated by ICON onto a lon-lat grid with a 1° resolution, therefore all analyses of the output are performed on the lon-lat grid instead of the native ICON grid.

Table 5.1: Names of the experiments that are compared in this thesis

Experiment name	Aerosol-Radiation Interaction (ARI)	Sensible heat flux (SHFL)
No ARI	No	No
ARI	Yes	No
ARI + SHFL	Yes	×1
ARI + SHFL*3.4	Yes	×3.4
SHFL*6.8	No	×6.8
ARI + SHFL*6.8	Yes	×6.8

5.1.1 Sensitivity to the sensible heat release

Different simulations will be compared to analyze the impact of the additional sensible heat release term and the consequences of enhancing this term by a constant factor.
To get a first impression, the mass-weighted height (MWH) of the plume is calculated. The points that are inside the plume are identified by their concentrations: Only points which exceed a threshold of $0.05\,\mu g\,m^{-3}$ in the concentration of soot in the insoluble accumulation mode are assumed to belong to the plume. Afterwards the MWH is calculated with

$$\mathrm{MWH} = \frac{\sum_n z_\mathrm{n} \cdot m_\mathrm{n}}{\sum_n m_\mathrm{n}}. \tag{5.1}$$

n is a grid point which belongs to the plume, z_n is its height, m_n is the soot concentration at the grid point.
The ARI experiment, which is depicted in red in Figure 5.1 and which does not include any additional sensible heat release yet, will serve as a reference to the other experiments. Its overall evolution of the mass-weighted heights matches what is known about the ANY event. The largest ascent of 1.3 km in one day is visible during the second day of the simulation. This corresponds to the 30th of December, which is known to be the day with the most intense pyroCb activity during ANY. The heights increase further during the third day, the 31st of December which is the last day of the first phase of pyroCb activity. They reach a maximum of around 3.6 km on the 1st January 2020 at 01:00 UTC. Then, the heights decrease again. This can be attributed to two factors. First, the sedimentation of the elevated plume lowers its center of mass. Second, during the days without any pyroCb activity, emissions occur at lower heights. These emissions are included in the mass-weighted height calculations, thereby lowering the height. During the seventh simulation day, the mass-weighted heights abruptly increase again. This corresponds to the 4th of January 2020, another day of intense pyroCb activity and the second phase of ANY.
Adding sh_fire to the surface heat flux in the ARI + SHFL experiment leads to a very similar evolution of the MWH, but its values are shifted upwards. The fastest ascent by 1.4 km again happens during the second simulation day. On average, the MWH is enhanced by 9.8% compared to the previously discussed simulation. At the maximum on the 1st January 2020, the mass-weighted height now reaches around 3.8 km. Overall, the MWH values are still much below those reported by Muth (2024).
This trend is continued for ARI + SHFL*3.4 experiment, where the MWH on average is 23.0% higher compared to the ARI experiment. The curve still follows a similar trend, but its largest increase on the 30th December is by 1.6 km. It reaches a maximum value of around 4.1 km. In the ARI + SHFL*6.8 experiment, the mean difference of the MWH in comparison to the ARI experiment is 47.7%. The MWH rises by 1.1 km on the 30th December and later reaches a maximum value of around 4.8 km.

Additionally, the plume top height is calculated and shown in panel (b) of Figure 5.1. In this case, the plume is not defined by its soot concentration but by its AOD. The top height is identified as the highest level where the soot AOD at the 550 nm wavelength exceeds a threshold of 0.001. This calculation is repeated for each time step, producing a curve that represents the development over

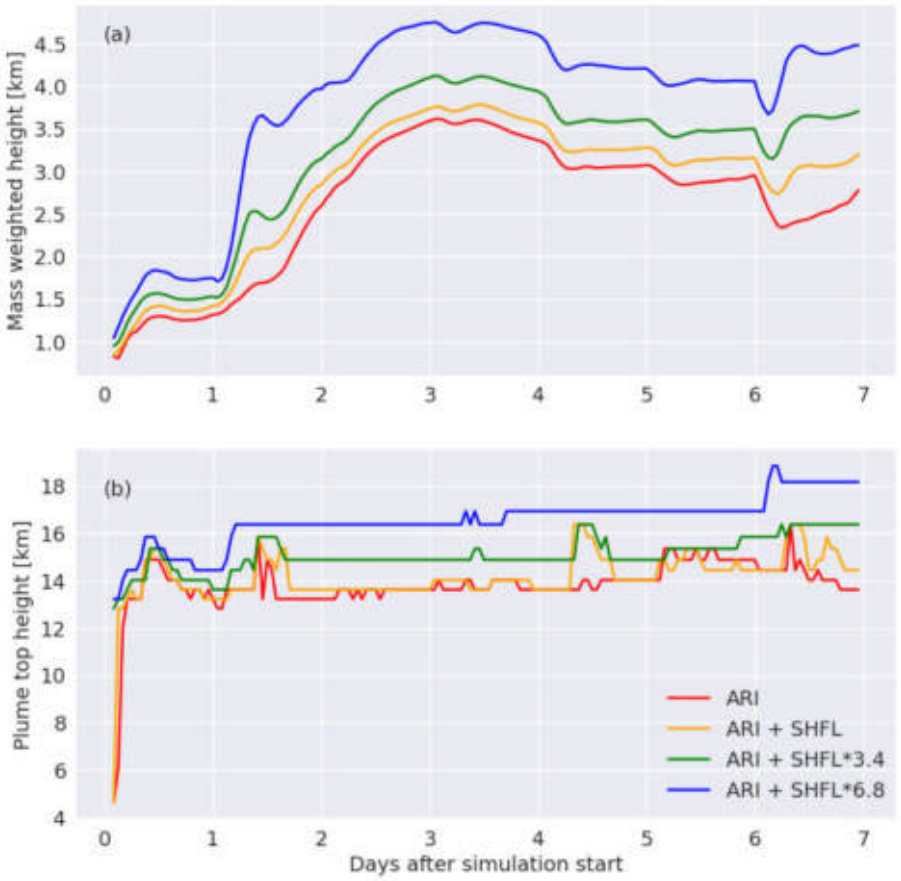

Figure 5.1: (a) Plume mass-weighted height where the plume is defined as points exceeding a threshold of 0.05 µg m^{-3} in the soot concentration, (b) plume top height where the threshold for the plume is a soot AOD at the 550 nm wavelength above 0.001. The different experiment setups are: ARI (red), ARI + SHFL (yellow), ARI + SHFL*3.6 (green), ARI + SHFL*6.8 (blue). All experiments were conducted with ARI enabled.

time.

In the ARI experiment, an elevated plume top height of up to 14.9 km is reached relatively quickly during the first day. A slight increase of the top heights over time is observed, likely due to lofting effects, which will be discussed in more detail later. However, the top height remains within a relatively narrow range, except for some short-time fluctuations in which it reaches 16.4 km. They can be attributed to the choice of the plume threshold.

Compared to the ARI experiment, the plume top height of the ARI + SHFL experiment is increased on average by only 2.8%, which is less than for the mass-weighted height. In the ARI + SHFL*3.4 experiment, the plume top is now significantly higher, with an average increase of 10.2% compared to ARI. It reaches values of 16.4 km around the end of the simulation, but unlike ARI it remains at this height for longer time periods. For ARI + SHFL*6.8, the plume top heights rise to over 18 km towards the end of the simulation. Especially compared to the other simulations, they seem to steadily increase. The mean increase of the top height compared to ARI is by 20.7%.

This sensitivity study shows that adding and tuning a sensible heat release due to the wildfire can increase both the plume mass-weighted and top heights. In the following sections, the impact of this height increase on the comparison with observations will be shown.

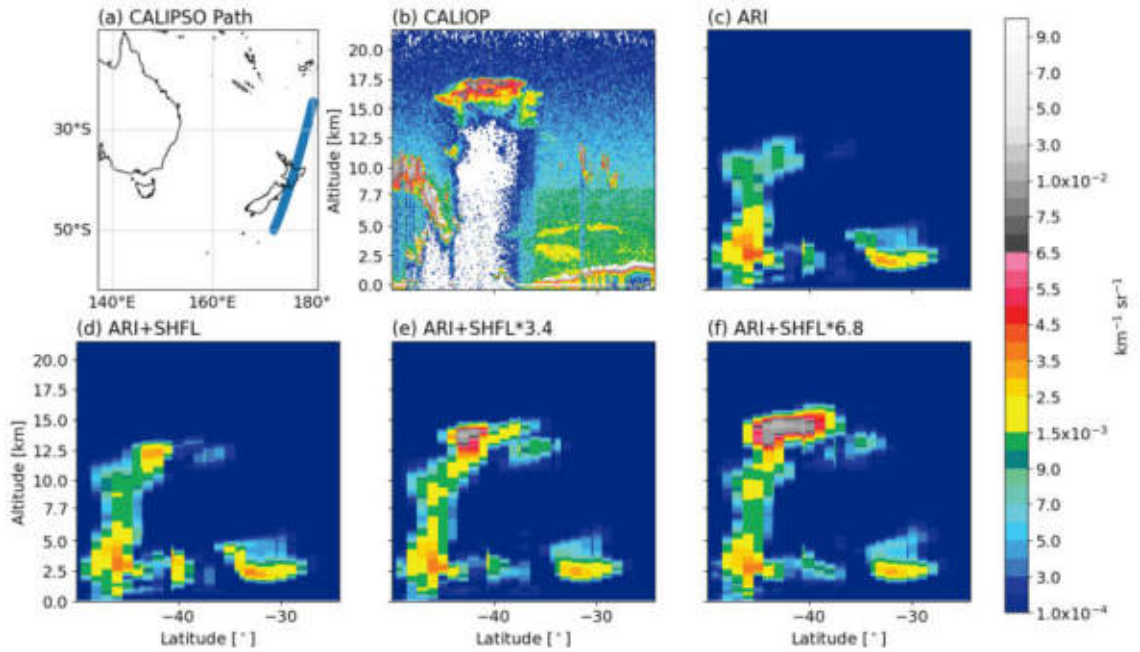

Figure 5.2: Attenuated backscatter at 532 nm measured by (b) CALIOP in comparison to the simulated attenuated backscatter at 532 nm for the different experiments: (c) ARI, (d) ARI + SHFL, (e) ARI + SHFL*3.4, (f) ARI + SHFL*6.8. The images were taken on the 1st January 2020 at 14:00 UTC. The CALIPSO path is shown in (a).

5.1.2 Comparison with CALIOP profiles

This section presents a comparison of cross-sections in the model results with CALIOP retrievals (Winker, 2022) with a focus on the plume heights. A cross-section through the plume which highlights the differences between the experiment setups particularly well is the image taken along a path across New Zealand on the 1st January 2020 at around 14:00 UTC, as shown in Figure 5.2. At this time, a signal is visible in the CALIOP image at heights between 15 and 17.5 km. Furthermore, some lower signals are depicted further north and at heights of up to 5 km, at lower attenuated backscatter values. All of these signals are classified as elevated smoke by the CALIOP aerosol subtype classification. The lower signals are reasonably well reproduced by the ARI and ARI + SHFL experiments in terms of location and height. However, the elevated signal of a smoke plume at around 40°S is missing in these simulations. In both cases, an uplift process is visible between 40 and 50°S, but it only reaches heights of around 13 km, underestimating the actual signals in terms of heights, but also in terms of attenuated backscatter values. In the ARI + SHFL*3.4 experiment, the elevated signal starts to become visible, although it remains below 15 km. The ARI + SHFL*6.8 experiment reproduces the observations best. The signal reaches heights of over 15 km, but it still remains slightly lower than the observations. The signal shape in this case is closer to what was observed by CALIOP compared to the previous cases. The attenuated backscatter signal of the elevated plume is slightly overestimated. In both cases where the sh_{fire} term is enhanced, the lower-level signals largely remain unchanged and still fit the observations reasonably well. To evaluate if this enhancement effect holds in general, further CALIOP comparisons were performed.

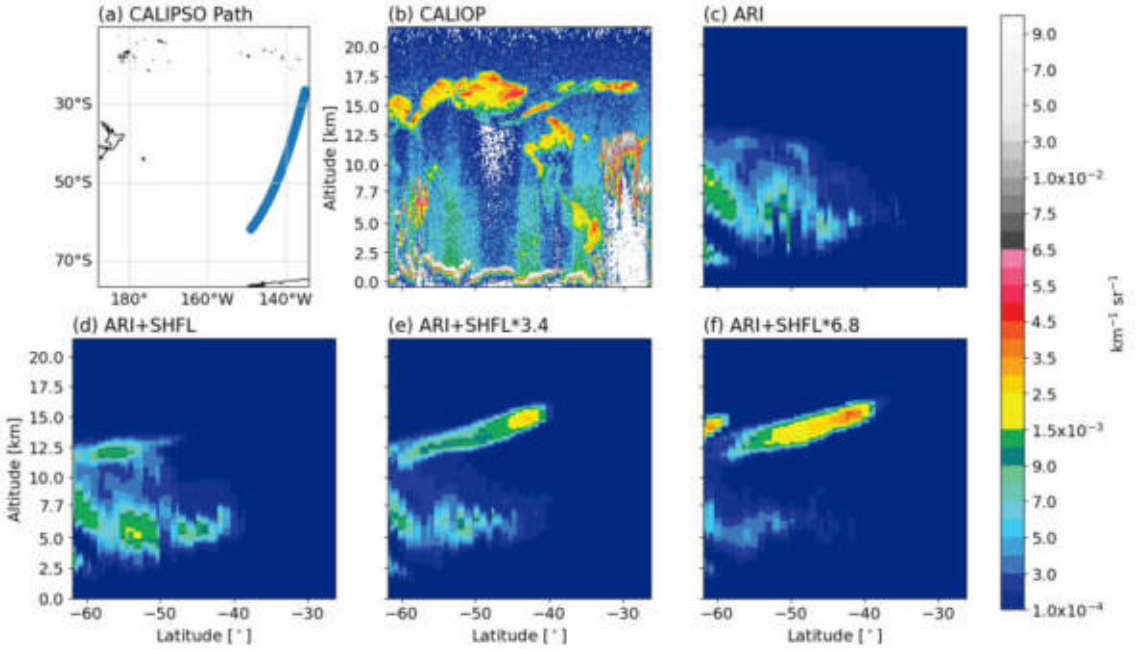

Figure 5.3: Attenuated backscatter at 532 nm measured by (b) CALIOP in comparison to the simulated attenuated backscatter at 532 nm for the different experiments: (c) ARI, (d) ARI + SHFL, (e) ARI + SHFL*3.4, (f) ARI + SHFL*6.8. The images were taken on the 4th January at 11:00 UTC. The CALIPSO path is shown in (a).

Figure 5.3 illustrates how the further transport and shape of the smoke plume signal better match the observations when the sh_{fire} term is added and enhanced by a factor. This image depicts the overpass on the 4th January at around 11:00 UTC over the Pacific, as shown in the upper left panel of Figure 5.3. This path is further away from the active fires in Southeastern Australia, indicating that the smoke has already traveled and distributed for some time. The CALIOP image shows elevated signals at heights between 15 and 17.5 km. These signals exhibit lower attenuated backscatter values and appear more diluted compared to the plume in Figure 5.2, they are also distributed wider in the latitudinal direction. The signal is fractioned into several subplumes. In the ARI case, none of the elevated signals are reproduced, with smoke signals only simulated at lower heights. For ARI + SHFL, an elevated signal is shown, but only with low attenuated backscatter values and at a height of around 12.5 km, so the heights are still underestimated. For ARI + SHFL*3.4 and ARI + SHFL*6.8, a distinct, elevated signal is simulated and the signals underneath decrease. This can be related to the amount of aerosols emitted or transported to the upper levels, which increases the signal above and reduces the signal below. The plume reaches heights of up to around 16 km, which is still lower than the observations. For ARI + SHFL*6.8, the intensities of the attenuated backscatter signal are reproduced the best and a second elevated plume appears towards the southernmost latitudes.

For the 4th of January, another comparison is shown in Figure 5.4. As the path in the upper left panel illustrates, this time the image was taken directly above the fires to capture the injection heights for the second phase of ANY. Here, the ARI experiment seems to match the observations best although in all experiments, the attenuated backscatter values of the plume seem to be severely overestimated. This indicates that the soot emission fluxes were overestimated for this day. Furthermore, the

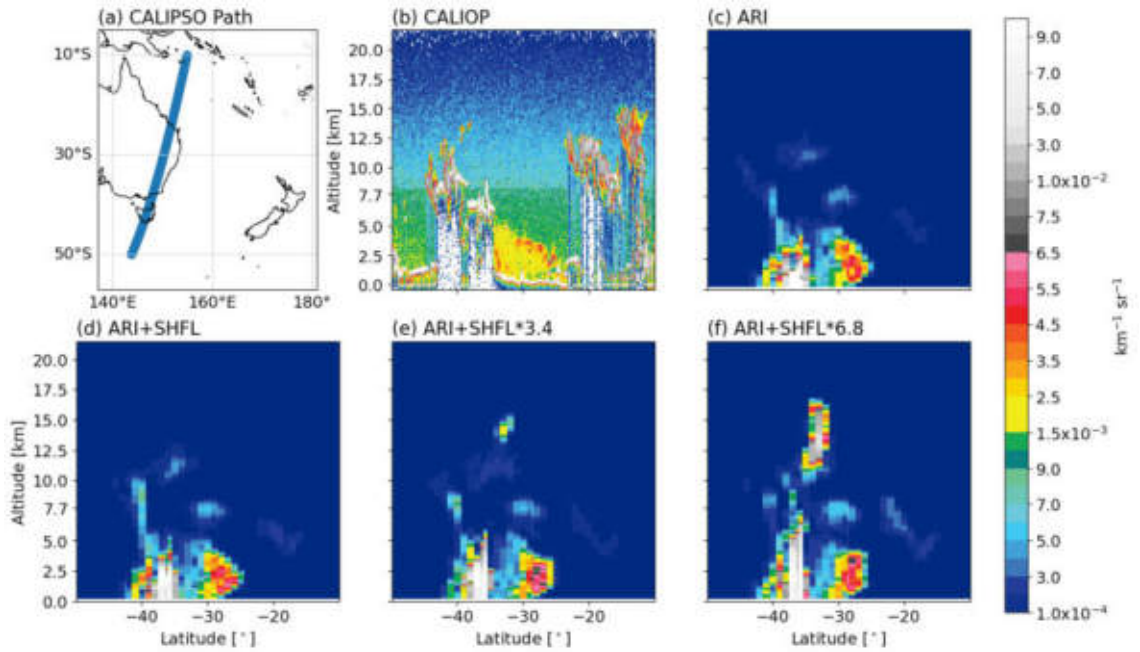

Figure 5.4: Attenuated backscatter at 532 nm measured by (b) CALIOP in comparison to the simulated attenuated backscatter at 532 nm for the different experiments: (c) ARI, (d) ARI + SHFL, (e) ARI + SHFL*3.4, (f) ARI + SHFL*6.8. The images were taken just above the fire regions on the 4th January at 16:00 UTC. The CALIPSO path is shown in (a).

ARI + SHFL*3.4 and ARI + SHFL*6.8 experiments overestimate the injection height, as smoke appears at around 15 km (or even higher until 17 km for ARI + SHFL*6.8) which cannot be identified in the observation data.

5.1.3 Comparison with MODIS cloud top height

To further investigate the impact of the enhancement factor on the plume top height, a comparison with the MODIS cloud top height measured onboard Aqua and Terra (MODIS Atmosphere Science Team, 2017a,b) is performed. Due to the extreme AOD and the interaction with clouds it is assumed that MODIS is not able to distinguish between cloud and plume top heights. The plume is therefore visible in the MODIS cloud top height and influences its values.

For this reason, both the cloud top height and the smoke top height are determined in the model data. In each grid column, the overall top height is set to the larger value between the two. The plume is identified by a threshold of 0.001 in the soot AOD at a wavelength of 550 nm, while clouds are defined by a threshold of 0.01 $\mathrm{g\,kg^{-1}}$ in the mass mixing ratio of cloud ice. Subsequently, the same area and point in time as in the MODIS image is selected in the model data. As the model time resolution is only 1 h, the hour closest to the MODIS image is selected. Furthermore, the resolutions vastly differ, from 1 km for the MODIS values to 1° for the ICON-ART output, therefore the points in the model data that are nearest to MODIS points are selected. Due to the resolution differences, this leads to model points being selected multiple times, so these duplicates are subsequently deleted. After creating the spatial plots for the direct comparison, the probability density function (PDF) for the heights is calculated for the observation and the model data.

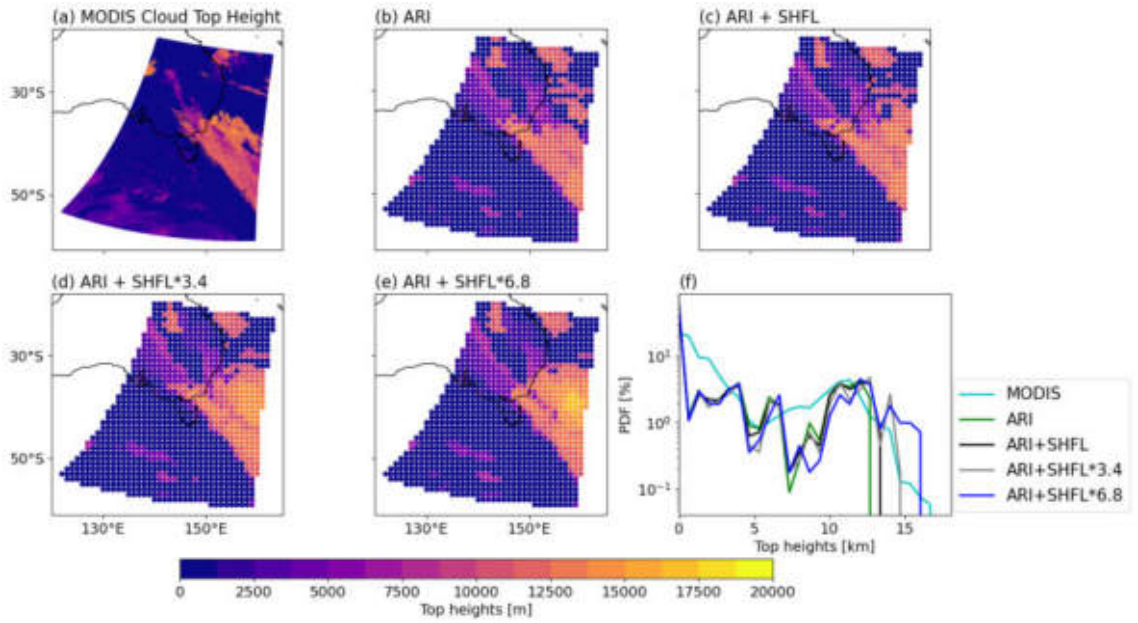

Figure 5.5: Comparison between (a) MODIS and ICON-ART top heights of both the plume and the clouds for the 31st December at 00:15 UTC for the experiments (b) ARI, (c) ARI + SHFL, (d) ARI + SHFL*3.4, (e) ARI + SHFL*6.8, (f) the probability density function for the plume top heights for direct comparison of the different experiments.

Figure 5.5 compares the MODIS cloud top height data with ICON-ART simulation results for the 31st December 2019 at 00:15 UTC, a time period where pyroCb activity was recorded (Peterson et al., 2021). In the MODIS image, the plume primarily originates in southeastern Australia, reaches high altitudes in close proximity to the sources and propagates in a southeastern direction. Overall, the horizontal shape of the clouds and smoke plume is relatively well reproduced by all experiments, especially considering the lower resolution. The ARI experiment displays a plume signal which matches the horizontal extent of the plume well but where some of the greatest heights are missing. In the ARI + SHFL plot, mostly the width of the plume increases but less so the top heights. In the ARI + SHFL*3.4 and even more so in the ARI + SHFL*6.8 experiment, the plume heights in the center of the plume are noticeably enhanced compared to the other two experiments.
This enhancement is also evident in the PDF comparison. The MODIS cloud top heights PDF starts at its largest values, then declines with height until around 5 km, rises until 12 km and then decreases again. The PDF for all three ICON-ART experiments show a similar decline until heights of around 7.5 km. Between around 7 to 10 km, the PDF for MODIS displays a larger frequency of points at this height range than the simulations. Then, the PDF for the three ICON-ART experiments increase again with height and their values start to diverge more. The largest difference between all functions is at the greatest top heights, where a cutoff in the PDF is observed. The observation data shows the largest height for the cutoff of around 16.7 km. The ARI + SHFL*6.8 gets closest to this, with a cutoff at around 16 km followed by the ARI + SHFL*3.4 experiment with 14.7 km. The ARI and ARI + SHFL experiments reach lower heights of around 12.7 km and 13.3 km, respectively. Therefore, the application of the tuned additional $sh_{\text{fire}} \cdot 6.8$ term shifts the maximum height by approximately 4 km compared to the ARI experiment. While the ARI + SHFL*6.8 experiment underestimates the top plume height cutoff, it overestimates the area of the plume which reaches elevated heights. This is visible in the map, where the diameter of the area with plume top heights

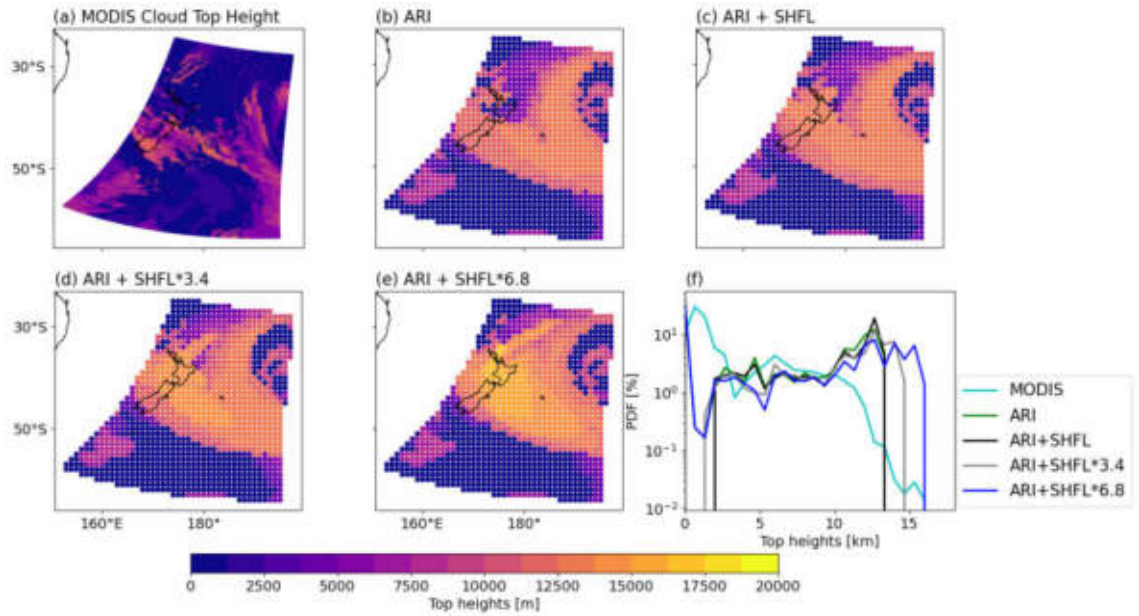

Figure 5.6: Comparison between (a) MODIS and ICON-ART top heights of both the plume and the clouds for the 1st January 2020 at 13:00 UTC for the experiments (b) ARI, (c) ARI + SHFL, (d) ARI + SHFL*3.4, (e) ARI + SHFL*6.8 (f) the probability density function for the plume top heights for direct comparison of the different experiments.

above 10 km appears significantly enlarged. Furthermore, the probability density function shows that there are more points at heights around 15 km for the ARI + SHFL*6.8 experiment compared to the observations.

Figure 5.6 shows the same analysis for the 1st January 2020 at 13:00 UTC, at the end of the first phase of ANY, where no more pyroCb activity was recorded. In this case, the image of the plume and cloud top height was taken further away from Australia, with New Zealand being located approximately at the center of the image. Therefore, the plume is already transported away from the sources and originates from the intense phase of ANY on the days before. The clouds and the smoke plume observed by MODIS are located over southern New Zealand, but also around the eastern border of the image. Some additional signals are visible in a southwest direction. The simulated shape of the smoke plume resembles these observations but appears even more enlarged horizontally than the previous example. The maps for the ARI and the ARI + SHFL experiments are very similar to each other, whereas, the ARI + SHFL*3.4 and ARI + SHFL*6.8 experiments exhibit an area of elevated heights located mostly over northern New Zealand.
The overestimated horizontal extent of the smoke plume is reflected by the PDF which has elevated values at heights above 10 km for all three experiments compared to the observations. The PDF functions for the ARI and ARI + SHFL experiments display very similar values throughout the entire height range and they have the same cutoff at 13.3 km. The height cutoff for the ARI + SHFL*3.4 experiment is located at 14.7 km. Again, the plume in the ARI + SHFL*6.8 experiment reaches the greatest heights out of all simulations. This time, it exhibits the same cutoff as the MODIS observations at 16 km.

5.1.4 Discussion

To understand the significant impact of the fire sensible heat release on the injection heights calculated by the plume rise model, it is important to note that in the plume rise model, the fire does not interact with its environment. While the model considers the atmospheric surroundings to calculate the plume heights, the fire itself does not affect the atmospheric state. As has been stated by Freitas et al. (2006), this is why the plume rise model is more applicable to lower-resolution models, where the feedback of the fire to the atmosphere is assumed to be negligible. However, the systematic underestimation of the plume heights suggests that, at least in more extreme cases such as the ANY event, the feedback of the fire to the atmosphere needs to be taken into consideration. The additional sensible heat release can correct this by increasing the temperature above the fires. This leads to more buoyancy, which increases the resulting aerosol plume height, as the plume rise model uses this modified atmospheric state to derive the injection heights.
The low resolution of the setup presented here leads to reduced vertical wind velocities, which consequently decreases the injection heights. We have shown that enhancing the sensible heat release with a factor increases of the mass-weighted heights. Additionally, the plume top heights then are significantly larger. Tuning the sensible heat release by a factor 6.8 counteracts the underestimation of the injection heights best. This is why the ARI + SHFL*6.8 experiment most closely simulates observations by CALIOP and MODIS.
In the comparison with MODIS cloud top height data, the model fails to correctly reproduce the horizontal extent of the plume, often overestimating the area which exhibits elevated plume heights. An issue with both cases that were presented in Figure 5.5 and Figure 5.6 is how much the plume top height depends on the threshold that defines which grid points belong to the plume. This threshold determines where the plume top height is located vertically. It is unclear at which concentrations MODIS recognizes the plume, and therefore which concentrations correspond to the measured top heights the best. Furthermore, the resolution differences between the simulation and observation data make the direct comparison more challenging. This is especially the case for the comparison of the PDF functions. As the PDF for the model data contains much less points overall, one data point has a much higher impact on the model data PDF than on the MODIS PDF. Furthermore, small-scale variations in height are not represented in the model data. This could explain the lower relative frequency of points between 5 and 10 km in the model compared to the MODIS observations, as the model might miss some smaller-scale clouds.

It is also important to note the uncertainties in the plume rise model that are related to the GFAS dataset. The presence of cloud or dense aerosol plumes directly above the wildfires can negatively impact the quality of the data. Another factor is the limited amount of satellite overpasses per day. Due to MODIS being located on polar-orbiting satellites, there are only around 3 to 4 measurements of a location available per day (Kaiser et al., 2012). This makes it likely that peak fire activities are missed in the FRP, which translates to an underestimation of the emission fluxes and the sensible heat release term.
To deal with this underestimation of emission fluxes, Kaiser et al. (2012) empirically derived an enhancement factor of 3.4 to reproduce the global distribution of soot aerosols. Such a global factor only has a limited applicability to the Australian region, which is the region of interest here.

This has several consequences on the comparisons to satellite data that have been performed. First, it limits how well plume top heights that are based on thresholds of soot concentrations can be compared quantitatively to the MODIS observations, since it is unclear how well the 3.4 factor reproduces the actual emission flux and, as a consequence, the soot concentrations.
Furthermore, it serves as an explanation why the ARI + SHFL*6.8 experiment fails to reproduce CALIOP observations for the 4th January 2020 in Figure 5.4, especially compared to previous days where model and observation data match well for this experiment in terms of heights and attenuated backscatter intensities. On this day, the comparison with CALIOP indicates overestimations of emission fluxes and injection heights, which also become visible in the form of abrupt increases in the plume mass-weighted and top heights (see Figure 5.1). Not only are the emission fluxes of all species enhanced by a factor 3.4, but also the sh_{fire} term which directly depends on another GFAS product, the FRP, was enhanced by different factors depending on the experiment. For the previous days, often clouds were located above the active fire and the enhancement likely counteracted an underestimation of FRP and emission fluxes that their presence caused. As an example, a MODIS true color corrected reflectance image of southeastern Australia on the 31st December 2019 is depicted in Figure 5.7 panel (a). For the 4th January, there much less clouds impacting the satellite view on the fires, as shown in Figure 5.7 panel (b). This indicates that for this day, the GFAS values already represent more realistic emission fluxes and FRP values. Therefore, their correction with enhancement factors is unnecessary and if done, leads to the overestimation that is visible in the CALIOP comparison.
Another source of uncertainty is whether the diurnal cycle of the fires is represented correctly. Zheng et al. (2021) determine a fire peak time of 15:00 local time or even later for the southeastern Australian wildfires between November 2019 and January 2020 using Himawari-8 FRP time series. In the simulations presented here, the peak in wildfire activity occurs earlier. Furthermore, as the entire diurnal cycle is multiplied by 3.4, the enhancement increases the emissions at the peak much more than at the other times. It is possible that this leads to a relative overestimation of the peak emission fluxes.
The variability of wildfires and the additional variability in how well they can be measured by satellites underlines that our assumptions, such as the global enhancement factors which were tested here, are not universally valid. We have shown that the enhancement factors of 3.4 and 6.8 for the emissions and the sensible heat release, respectively, have matched the MODIS and CALIOP measurements best for all days except for the 4th January. In the following parts of the thesis, mostly the two experiments SHFL*6.8 and ARI + SHFL*6.8 will be further analyzed. For further discussions, the simulation results for the 4th January are mostly left out.

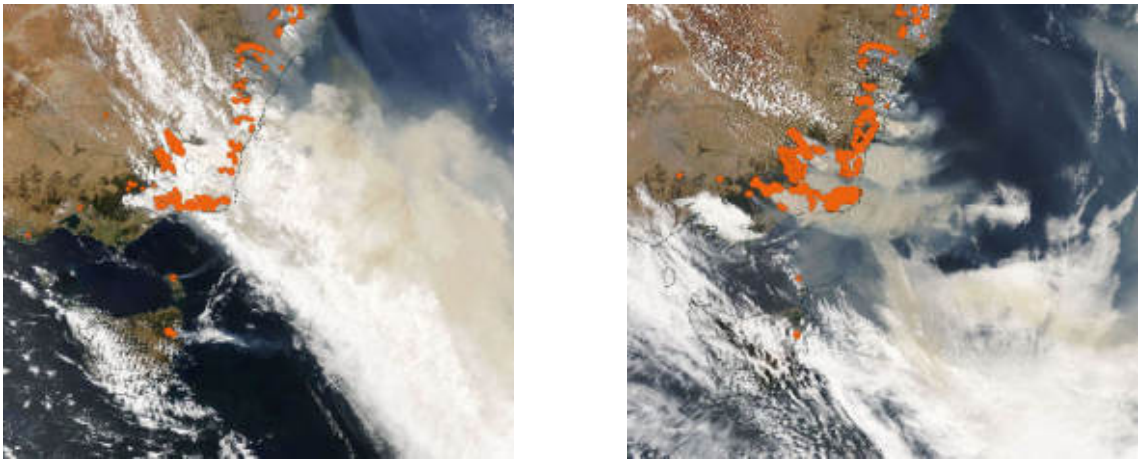

(a) (b)

Figure 5.7: Comparison of true color corrected reflectance images of southeastern Australia as seen by MODIS onboard the Aqua satellite for (a) the 31st December 2019 and (b) the 4th January 2020. The fires detected by Aqua are marked as orange dots (NASA Worldview Snapshot, ESDIS).

5.2 Validating the transport of chemical trace gas emissions

For this thesis, the plume rise model in ICON-ART was extended such that it can also emit chemical trace gases. To validate that this implementation works correctly and to investigate the horizontal and vertical transport of the smoke plume, the ARI + SHFL*6.8 experiment is used. In addition to soot, the wildfires here only emit CO as a trace gas. The CO is then treated with a lifetime chemistry and its horizontal and vertical distribution over time is compared to satellite retrievals from IASI and MLS.

5.2.1 Comparison with IASI retrievals

Figure 5.8 contains a comparison of the CO column load between model and observational data. The left side shows daily averaged CO data from the IASI satellite, with the image taken from Bègue et al. (2021). The right side depicts the column loads that were calculated by summing up the CO loads from the ARI + SHFL*6.8 simulation across all height levels. The rows represent the three days from the 31st of December to the 2nd of January, which lie within the simulated time frame. Since it is unclear when exactly the measurements that went into the daily average depicted in Figure 5.8 were performed by IASI, the column loads from the model are shown for 12:00 UTC of each day. This limits the comparability of the results.
For the 31st December, the modeled distribution of the CO column load matches relatively well, with its overall shape and its values that go up to above $9 \cdot 10^{18}$ molecules cm^{-2}. The plume width appears narrower horizontally in the simulations than in the satellite data. As the smoke plume moves away from the sources on the subsequent days, the modeled CO appears to dilute more quickly than that observed by IASI, which becomes especially visible for the 2nd of January. Furthermore, additional sources of CO that are located in southwestern Australia appear more

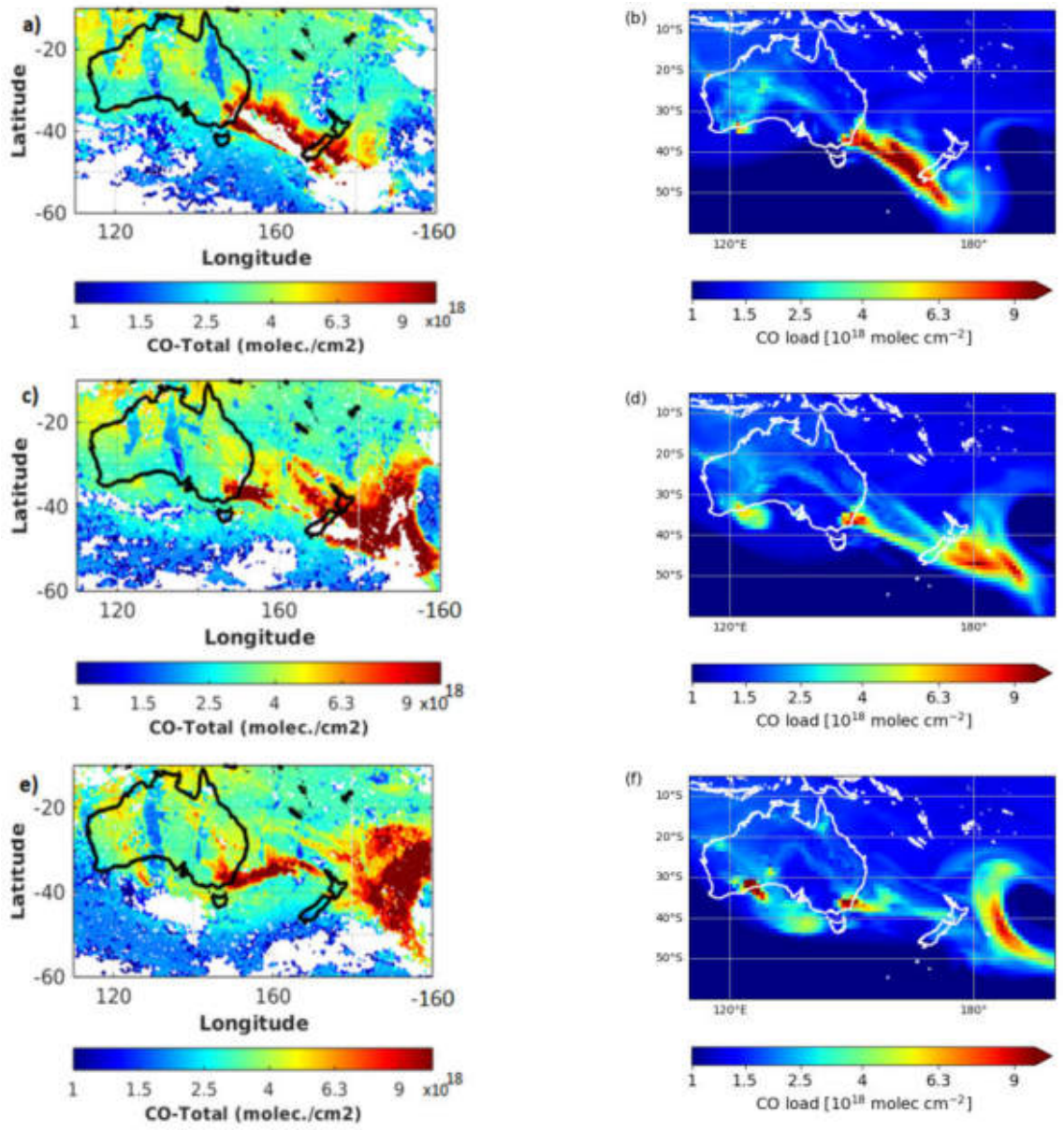

Figure 5.8: (a), (c), (e) show daily averaged CO column load data from the IASI satellite for the 31st December 2019, 1st January 2020 and 2nd January 2020, respectively. The image is from Bègue et al. (2021). (b), (d), (f) show the corresponding CO column load values from the ARI + SHFL*6.8 simulation for the same days at 12:00 UTC.

strongly in the modeled CO column load than in the observed one. Such regional differences in the CO distribution can be explained with limited overpass times or by clouds impacting the view for IASI.

Kaiser et al. (2012) recommend the use of the 3.4 enhancement factor only for the soot emission fluxes, not for the chemical trace gases and conclude that the low bias in their emission data only applies to aerosols. However, since we showed that the CO column load values match well with IASI when this factor is applied to the emission, we continued to use it for CO and also all other chemical trace gases throughout the thesis. Overall, this comparison shows that the emission implementation in ICON-ART works as intended and the horizontal transport of CO seems to be captured reasonably well by the model.

5.2.2 Comparison with MLS retrievals

The MLS can be used to observe the smoke plume that originated from the ANY event, particularly in terms of its vertical transport. This is illustrated in Figure 5.9 panel (a), which was created by Alexandra Laeng (personal communication). In this image, the onset of ANY is visible in time series data of CO concentrations. Around the 29th/30th December 2019, the CO concentrations quickly rise for the lowermost pressure levels of 316 hPa, 215 hPa and 146 hPa to around 1200, 900 and 550 ppbv, respectively. This increase is consistent with the first phase of pyroCb activity during ANY. A less pronounced second peak around one week later is visible, again in the 316 hPa, 215 hPa and 146 hPa pressure levels. This peak can be attributed to direct injection from the second phase of the ANY event on the 4th January. For the pressure levels higher up in altitude, the increase in CO concentrations happens with some time delay, and their respective peaks are shifted by several days. These peaks can be attributed to self-lofting effects, as described in 2.2.3. As this process is much slower than direct pyroCb injection, it is likely the reason for the time delays in the upward movement.
Panel (b) of Figure 5.9 shows a version of the plot that covers only the seven days that were also simulated in this thesis. In the observations, this time period mainly contains the effects of the first ANY phase, with its peak in concentrations for the two lowest pressure levels on the 31st December. Afterwards, the concentrations at 316 and 215 hPa reduce due to dilution of the plume and its distribution onto pressure levels above and below, but overall they stay at values that are elevated compared to before ANY. At the 146 hPa, 100 hPa and 68 hPa pressure levels, the mixing ratios further increase and remain stable between the 3rd and 4th January, with values around 500, 500 and 250 ppbv, respectively.

To compare the model results to these observations, the output is interpolated by ICON onto the same pressure levels as those shown in Figure 5.9. Then, at each pressure level and for each day the points that are the closest to points where MLS measurements were performed are selected for the respective time of the satellite overpass. Their ten highest concentrations between 10° and 60°S are identified for each day and pressure level. Lastly, the mean is calculated to be plotted as a time line for each pressure level.
As shown in Figure 5.10, the results only resemble the observations to a limited extent. The last simulation day exhibits very high mixing ratios of up to 1750 ppbv for the 100 hPa pressure level. The drastic increase indicates that the injection occurs directly into the large altitudes of the 100 hPa level. As we have shown, the emission fluxes and heights are overestimated on this day, which is why all values from this day are left out of further discussions here.
For the 316 hPa level, the maximum occurs later than in the observations and it is less prominent, reaching only 327 ppbv. The 215 hPa level exhibits a peak one day earlier than in the observations and it has higher mixing ratio values of 1670 ppbv. The peaks at 146 hPa and 100 hPa both develop later than in the observations and they are enhanced by 500 ppbv and reduced by 50 ppbv compared to their MLS observation counterparts, respectively. The concentration increase in the 68 hPa pressure level is not visible at all in the model data.

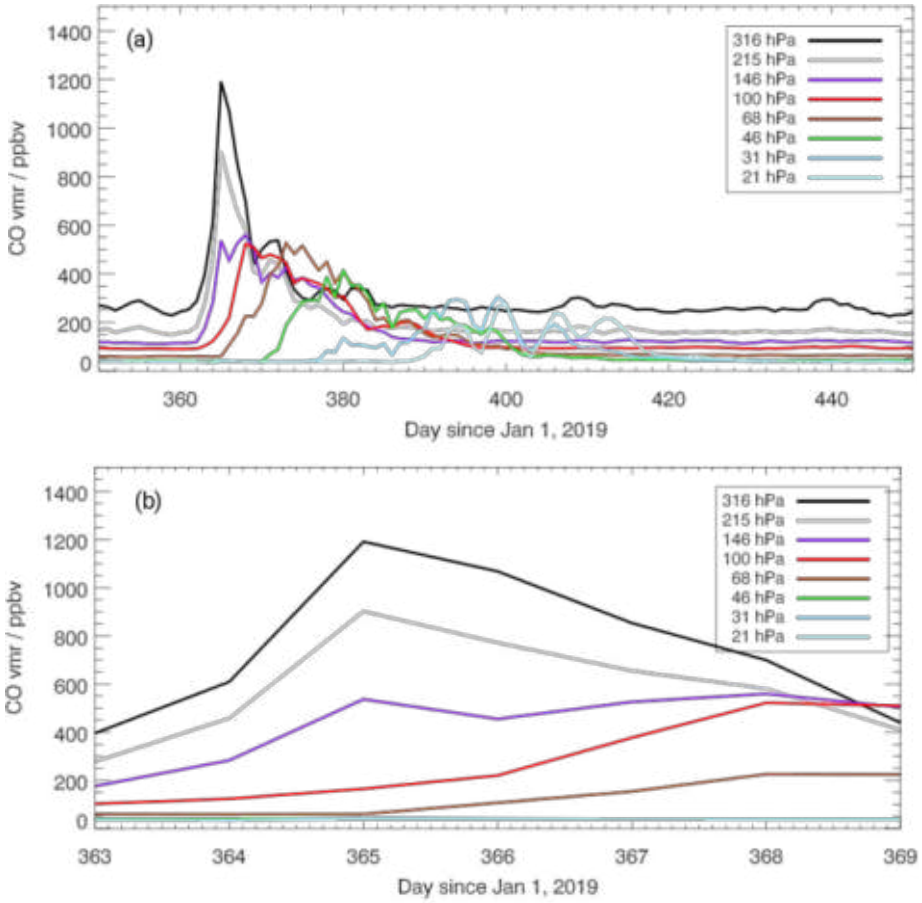

Figure 5.9: Timeline of the CO mixing ratio values during 2019 and 2020 for several pressure levels obtained from MLS data. For each pressure level and day, the mean of the 10 highest daily values between 10 and 60°S is taken. The values are shown for the pressure levels at 316 hPa, 215 hPa, 146 hPa, 100 hPa, 68 hPa, 46 hPa, 31 hPa and 21 hPa. Panel (b) shows a version of (a) that is zoomed in such that it only covers the days that were simulated in this thesis (Alexandra Laeng, personal communication).

The low spatial resolution of the MLS data plays a role in the poor comparability of both plots. If the simulated plume is shifted horizontally compared to the observations, the elevated CO values that it exhibits are missed in Figure 5.10, as only the points along the MLS track are taken into consideration. The fact that the modeled plume has a lower spatial extent than in the observations (as shown in Figure 5.8) makes it even more likely that the plume was missed. At least for the 316 hPa level, it can even be debated whether the simulation data should accurately reflect the behavior shown in Figure 5.9. CO data measured by MLS at this level is generally not recommended for scientific use as it contains contributions of values at 316 hPa, but also pressure levels located above (Livesey et al., 2022).

Another reason for the differences between the model and the observations is that the enhancement of the sensible heat release in the plume rise model possibly favors injection at high altitudes while suppressing it at low altitudes, which could explain why the peak is underestimated at 316 hPa but overestimated for 215 hPa and 146 hPa. This is in agreement with the CALIOP comparison in the previous section Figure 5.2, where the attenuated backscatter values of the most elevated plume were slightly overestimated by the model.

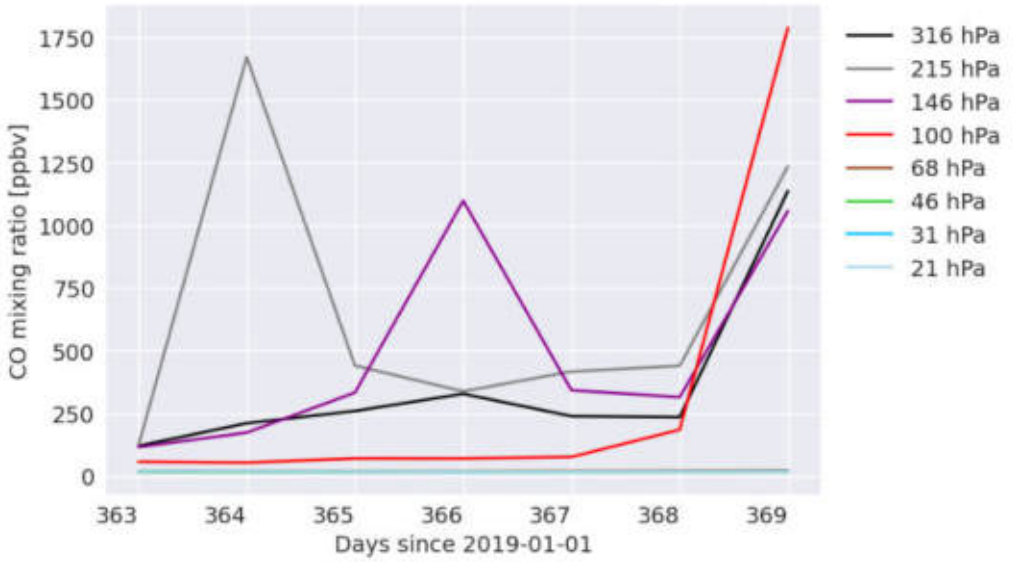

Figure 5.10: Timeline of the CO mixing ratio values during the simulation time period for the same pressure levels as in the MLS data. For each pressure level and day, the mean of the 10 highest daily values between 10 and 60°S is taken along the satellite track. The values are shown for the pressure levels at 316 hPa, 215 hPa, 146 hPa, 100 hPa, 68 hPa, 46 hPa, 31 hPa and 21 hPa.

The two comparisons of the model data with IASI and MLS show that the implementation of the CO emission works as intended. Whether the lofting rates of the plume are correct however exceeds the scope of these analyses. In the following chapters, it will be analyzed in more depth what influences the lofting rate, on how these processes can be modeled realistically.

6 Analysis of the self-lofting mechanism

Based on the ARI + SHFL*6.8 experiment, which matches the observations best, the focus shifts to the second part of the uplift which allows the plume to reach greater heights well after the initial injection: the self-lofting mechanism. The following chapters will analyze how well the self-lofting mechanism can be reproduced with the setup used in this thesis and assess its impact on the plume evolution.

6.1 Impact of aerosol-radiation interaction depending on the injection height

Switching on ARI enables self-lofting effects, as the plume absorbs solar radiation and warms as a consequence. Figure 6.1 panel (a) shows the temporal evolution of the mass-weighted heights. They are very similar during the first two days of the simulation for the experiments with and without ARI, respectively. Each MWH where ARI is enabled is located slightly above that without ARI during this time period, except for the second day and the case without additional sensible heat release, where the No ARI experiment reaches slightly higher mass-weighted heights than the ARI experiment during the ascent. The mass-weighted heights with and without ARI begin to differ more after a few days. In both cases with and without additional sensible heat release, the plume reaches greater heights when ARI is enabled. The plumes in the ARI and the ARI + SHFL*6.8 experiment begin to significantly rise up to 3.6 and 4.7 km during the third day that was simulated. Figure 6.1 panel (b) depicts the difference between the experiment versions with and without ARI, for both cases with and without sensible heat release, respectively. During the first day, the experiments without additional sensible heat release have a difference of up to 212 m due to ARI, whereas the difference between ARI + SHFL*6.8 and SHFL*6.8 is only 45 m. For all subsequent days, the difference between ARI + SHFL*6.8 and SHFL*6.8 is larger with a maximum value of 652 m than between ARI and No ARI, which have a maximum difference of 562 m.
The large similarity between the versions with and without ARI during the first two simulation days is because the self-lofting effect is less relevant at this timescale and the curve is dominated by pyroCb injection. In cases with ARI, a local stabilization of the atmosphere can occur due to radiation absorption and subsequent warming. Since the plume rise model takes atmospheric stability into consideration when calculating the plume height, this can reduce the mass-weighted heights. This is likely the reason why the No ARI experiment reaches larger MWH than the ARI experiment during the second simulation day. However, later in the simulation, the self-lofting

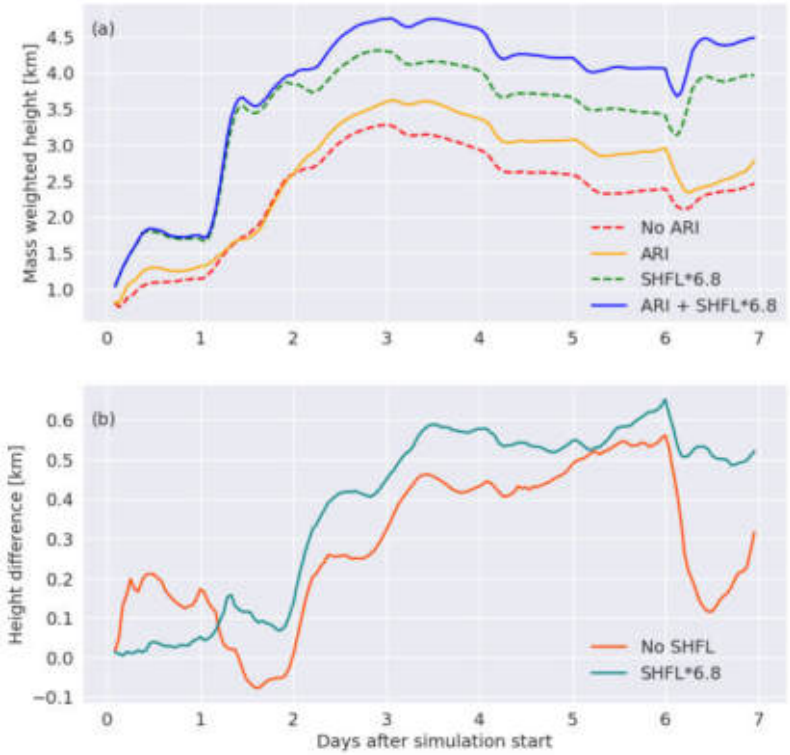

Figure 6.1: (a) Plume mass weighted height where the plume is defined as points exceeding a threshold of 0.05 µg m^{-3}. The different experiment setups are: No ARI (red), ARI (yellow), SHFL*6.8 (green), ARI + SHFL*6.8 (blue). Experiments were ARI is switched off are represented by dashed lines. (b) Differences in mass-weighted heights ARI - No ARI (orange) and ARI+SHFL*6.8 - SHFL*6.8 (turquoise).

effect which is slower than the pyroCb injection becomes relevant and plumes in simulations with ARI ascend further than those without ARI. The differences between the respective curves with and without ARI then increase. ARI has a larger impact on the MWH in the experiments with SHFL compared to without SHFL. This is because without SHFL, the initial injection heights are much lower. In this case, the plume is mostly located below the cloud tops. Clouds can inhibit solar radiation from reaching the plume and thus hinder its ascent. By creating greater injection heights in the SHFL*6.8 case, the plume reaches similar or even larger heights than the cloud tops and the absorption of radiation is less affected by their presence.

An example for this effect is given in Figure 6.2, which shows an arbitrarily selected cross section along the 156°E longitude through the plume and cirrus clouds on the 31st December 2019 at 12:00 UTC. In the cross section, the ARI and ARI + SHFL*6.8 experiments are compared with respect to the plume and cloud location. For ARI, the plume is located at heights below 5 km. The cirrus clouds are located above, at heights between 6 and 12 km, and can inhibit solar radiation from reaching it. For ARI + SHFL*6.8, the cloud is located at similar heights, but the cloud ice content at the maximum is 55.3 mg kg^{-1} higher than in the ARI case, with mixing ratios of up to 124.4 mg kg^{-1}. A part of the plume is still located below the clouds, but it is the part with lower soot concentrations. The majority of the plume, and especially the part with high soot concentrations, is located above the clouds and its absorption of solar radiation is therefore not impacted by them.

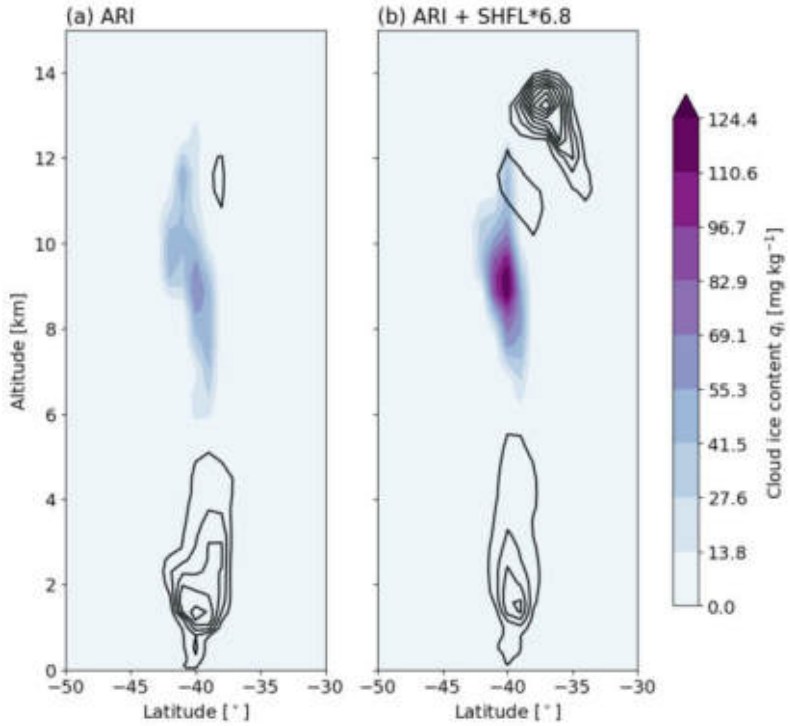

Figure 6.2: Cross-section through the plume and cirrus clouds for 31st December 2019 at 12:00 UTC along the longitude at 156°E. The cirrus clouds are represented by their cloud ice content q_i. The plume is marked by black contour lines that are based on the mixing ratio of soot in the insoluble accumulation mode in ($\mu g\,kg^{-1}$) to serve as an orientation of where the plume is located. The comparison is shown for (a) the ARI experiment (b) the ARI + SHFL*6.8 experiment.

To get a more complete picture which includes more time periods, more different plume locations and to additionally consider liquid water clouds, Hovmöller diagrams are created. They contain the sum of the cloud ice and the cloud water content $q_i + q_c$ and the soot mixing ratio. For each time step in the diagrams in Figure 6.3, height profiles are calculated, which are the mean profiles of $q_i + q_c$ and the soot mixing ratio between all grid columns that are classified as containing a plume. Plume columns are identified by their soot column load exceeding $0.05\,g\,m^{-2}$. This allows for a comparison of the height profiles of cirrus clouds and the smoke plume over time for both the ARI and ARI + SHFL*6.8 experiments.

Both experiments show liquid water clouds and cirrus clouds existing in grid columns where smoke plumes are present. Generally the cloud types can be differentiated in Figure 6.3 by the height at which they occur, but the same Hovmöller diagrams were also generated for q_i and q_c separately to know more specifically which signals belong to which cloud (not shown). In the ARI experiment, the majority of the cloud ice content is located above the smoke plume, which generally remains below the typical cirrus cloud height of around 10 km. The cloud water content remains at heights below 5 km, such that a part of the plume is located above. The mean q_c profile reaches maximum concentrations of up to $169\,mg\,kg^{-1}$. The most significant uplift of soot occurs during the second simulated day, where heights above 10 km are reached but only with low mixing ratios. At approximately the same time, the mean cloud ice content in plume columns reaches its maximum of $28.9\,mg\,kg^{-1}$.

In the ARI + SHFL*6.8 experiment, there are two plume signals. One part remains below heights

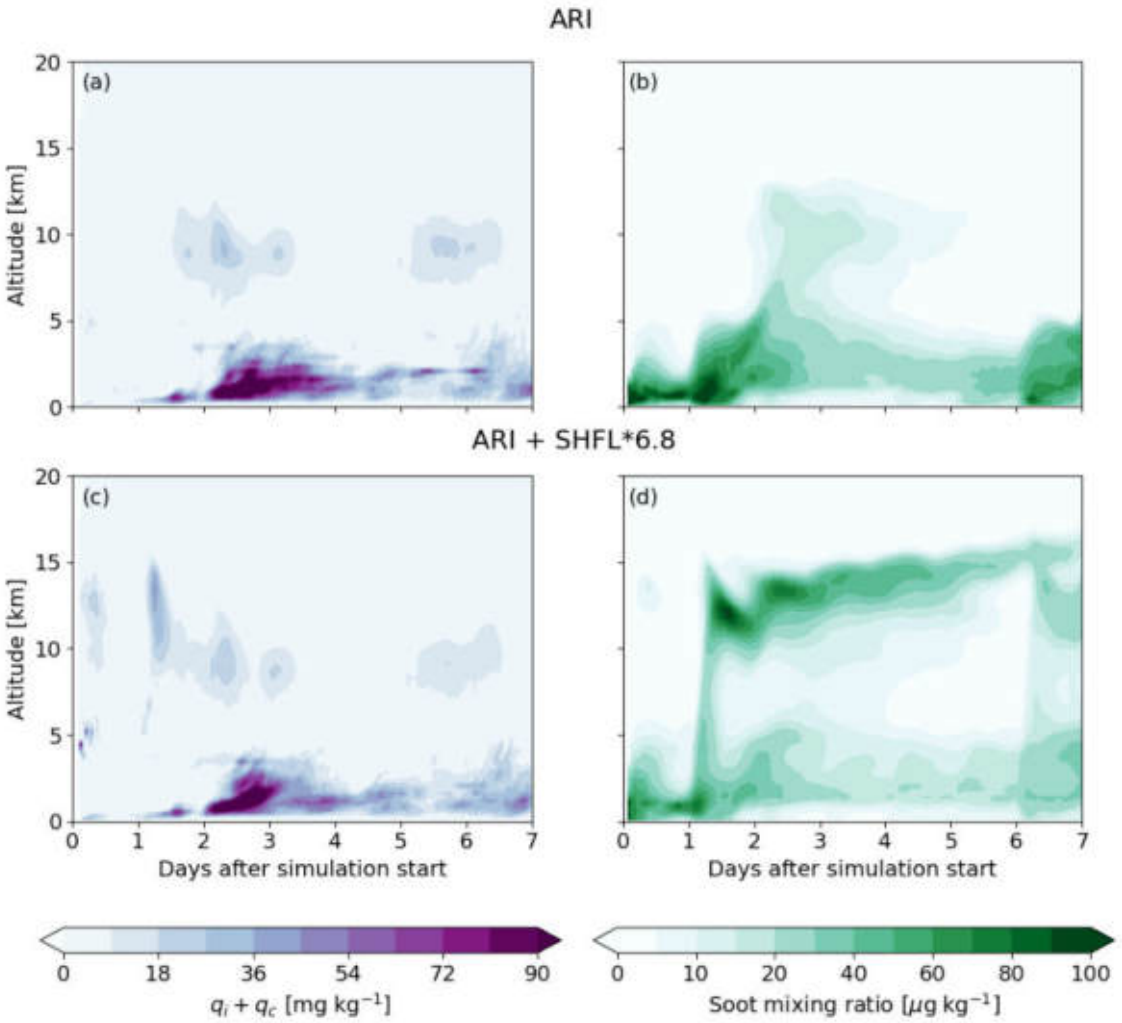

Figure 6.3: Hovmöller diagrams of the (a, c) cloud ice content and (b, d) the soot mixing ratio for the ARI experiment (upper row) and ARI + SHFL*6.8 experiment for columns which contain a plume. The plume columns are defined as those which contain a soot column load above 0.05 g m^{-2} and for each time step, their mean profile is calculated both for the cloud ice content and the soot mixing ratio.

of 5 km, below the cirrus clouds and within the height range of liquid water clouds. The other part originates from injection heights between 10 and 15 km on the second day. The height median of the elevated part of the smoke plume ascends from around 12.5 km to 15 km, which it reaches just before the seventh day. On this day, the 4th January, injection occurs again at heights which are probably overestimated. While the elevated plume rises due to lofting effects, it is also diluted and the mean mixing ratios in its center decrease from almost 100 µg kg^{-1} to around 20 µg kg^{-1}.
The plume top appears to move up only slightly from just below 15 km on the 30th December to around 16 km on the 4th January. It is rather the center part of the plume that shows the most evident uplift. This part is also where the largest soot concentrations are located.
Furthermore, an intense injection into elevated model heights is observed in the ARI + SHFL*6.8 experiment during the second day. This coincides in the Hovmöller diagrams with strong cirrus cloud formation. The mean cloud ice content reaches its maximum values, which are 48% higher

than in the ARI experiment. Additionally, cirrus clouds that form during this injection phase appear at greater heights of up to 15 km compared to those that appear later in the simulation when the uplift is weaker. The formation of liquid water clouds reaches its maximum value one day later, during the third simulation day, and it is only 6% higher than in the ARI experiment. Throughout the entire self-lofting process, the elevated smoke plume remains above both the cirrus clouds and the liquid water clouds.

The coexistence of liquid water and ice clouds inside plume columns suggests a possible connection between their formation and the soot uplift. Their maxima occur on days with strong smoke uplift, which shows that these clouds can be related to the pyroconvection. The observation that both the maximum cloud ice content and cloud water content are higher in the ARI + SHFL*6.8 experiment than in the SHFL*6.8 experiment can be attributed to the heat release triggering convective cloud formation despite the low resolution and the convection parameterization.
This analysis also shows that a major part of the self-lofting does not occur at the plume top. The center part of the plume where the highest concentrations are located contributes the most to self-lofting, which confirms the importance of the correct aerosol concentrations for the self-lofting rate.
To conclude, reaching elevated initial emission heights of wildfires due to pyroCb injection is crucial to get a large absorption of solar radiation. This is necessary to correctly reproduce the self-lofting of the plumes that are created in the process and it makes the results of chapter 5 even more important.

6.2 Identification of local heat anomalies

Due to the absorption of solar radiation, the plume heats up. This becomes visible in the form of local heat anomalies in the direct comparison of the SHFL*6.8 and ARI + SHFL*6.8 experiments. In Figure 6.4 panel (a), the radiative heating is depicted in the form of a Hovmöller diagram. The heating profiles are calculated again by identifying the grid columns with a soot column load above $0.05\,\mathrm{g\,m^{-2}}$, with the difference that only those columns are selected which exceed the column load threshold for both the SHFL*6.8 and the ARI + SHFL*6.8 experiment. Then, the temperature difference ΔT between both experiments, so with ARI minus without ARI, is calculated and the mean profile for each time step is plotted. For panel (c) on the right-hand-side, the soot mixing ratio is given to serve as an orientation for the plume height at each time step.
From the comparison of the two experiments, there is a positive heat anomaly visible inside the plume, and a negative anomaly above the plume. The anomalies are most evident between 2 and 5 days after simulation start. The positive differences in mean temperature are above 1.6 K, whereas the negative differences only reach up to 1.2 K. Between the areas of positive and negative values, the temperature difference changes its magnitude and also its sign within less than 1 km of height. The border between the heating and the cooling regions in the plot is between 13 and 14 km altitude depending on the time step, as it also shifts upward while the plume ascends. The relative cooling above the plume extends high up into the atmosphere until a height of around 20 km.
The heating occurs with some time delay compared to the soot emission. It becomes evident only

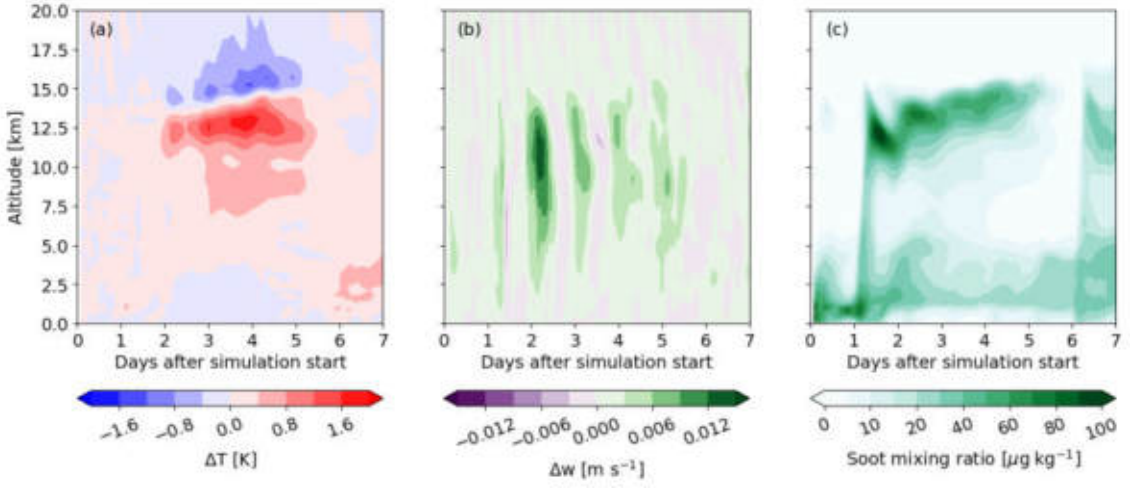

Figure 6.4: Hovmöller diagrams of (a) the temperature difference ΔT between the SHFL*6.8 and the ARI + SHFL*6.8 experiment, (b) the vertical wind velocity difference Δw and (c) the soot mixing ratio for the ARI + SHFL*6.8 experiment for columns which contain a plume in both experiments. Plume columns are defined as those which contain a soot column load above $0.05\,\mathrm{g\,m^{-2}}$ and for each time step, the spatial mean of their height profile over time is calculated for all three plots.

during the third day of the simulation, but not yet during the second day where the smoke plume has already been injected into elevated heights. Interestingly, the greatest heat difference between the experiments is reached around the end of the fourth day, where the plume has already become more diluted. In reference to the previous section, the most intense heating occurs above the heights of around 10 km and therefore in regions above cirrus clouds. Some smaller positive temperature difference occurs around the same height as the cirrus clouds, but below there is much less heating visible.

The heat anomalies result in additional vertical movement of the plume, which is evident in the vertical wind velocity w. To compare the vertical velocity to both the temperature difference and the soot mixing ratio distribution, another Hovmöller diagram in panel (b) of Figure 6.4 is created. The same plume columns are selected as before and the difference in vertical wind velocity between the ARI + SHFL*6.8 and the SHFL*6.8 experiments Δw is calculated. Its mean height profile is then derived for each time step.

The Hovmöller diagram for Δw shows upward signals in the vertical wind difference during the local daytime in Australia. These anomalies are visible to different extents for each day of the simulation time period. Between the second and the fifth day of the simulation, the signals are evident at an altitude range between around 5 to 15 km. The maximum vertical velocity difference occurs on the third day of the simulation, with mean values above $0.015\,\mathrm{m\,s^{-1}}$ inside the plume. Overall, there are more and higher positive differences between the vertical velocities than negative differences, which do not exceed an absolute mean value of $0.006\,\mathrm{m\,s^{-1}}$.

Δw displaying more positive than negative values suggests that there is an additional upward vertical transport within the plume columns that is caused by ARI. The day-to-night oscillation in the vertical wind differences is not observed in the temperature difference in panel (a), which remains more constant over time. This could be due to the more stable nighttime atmosphere, which hinders

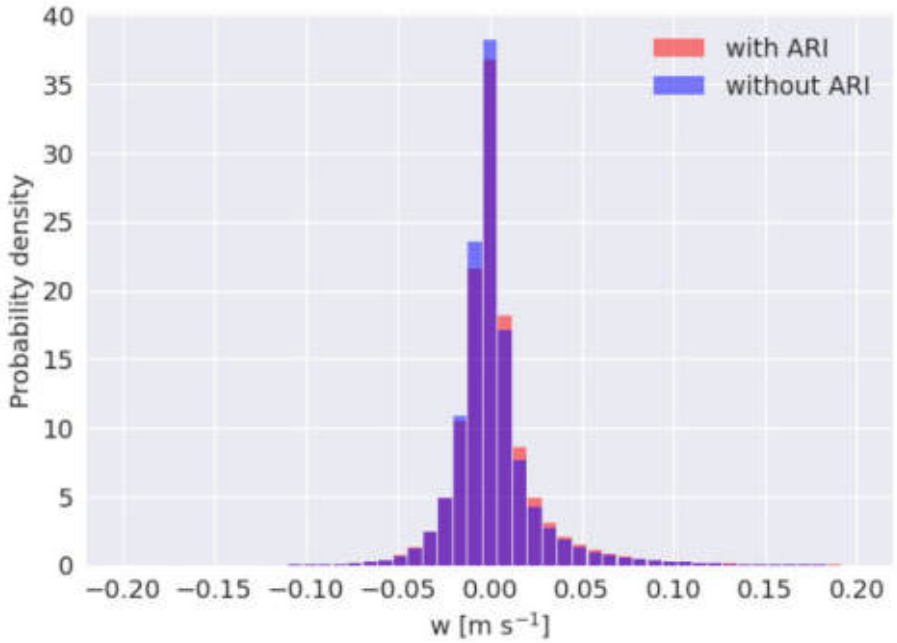

Figure 6.5: Histogram of vertical velocities inside plume columns for the ARI + SHFL*6.8 and the SHFL*6.8 experiments. The columns were again selected for each time step separately based on their soot column load being above 0.05 g m^{-2} in both experiments. Then, the histogram of the w values that the selected columns contain is calculated over all time steps for both experiments. Only the values in the column below a height of 20 km are taken into consideration.

the ascent of the plume despite an almost unchanged temperature difference. Furthermore, the maximum of Δw occurs earlier in the experiment than that of ΔT, which could also be caused by differences in atmospheric stability.

This tendency towards positive and larger vertical wind velocities is also supported by Figure 6.5. Instead of subtracting the two experiments, the histograms of their vertical velocities are calculated and overlaid semi-transparently to highlight the differences in each bin. The plume columns to be considered for the histogram are selected using the same criteria as the Hovmöller diagrams. Since w values far above the plume are not expected to be affected by its presence, all points within this column below a height of 20 km are included in the histogram. This process is repeated for each time step, such that the histogram encompasses points within the plume columns over the entire simulation timeline.
Both experiments lead to similar histograms, where the probability density is highest for vertical wind velocities around zero and it reduces as the absolute values of w increase. The direct comparison of both experiments however shows a tendency towards positive vertical wind velocities in the ARI + SHFL*6.8 experiment, as the bars on the right-hand-side of the plot are slightly larger for this experiment. This leads to the mean of the histogram with ARI being shifted to 0.0036 m s^{-1} compared to 0.0026 m s^{-1} without ARI. Towards the end of the histogram, more elevated positive velocities above 0.1 m s^{-1} also show an increase in frequency if ARI is enabled. For the experiment without ARI, the bin around zero vertical velocity is enhanced by 3.6% compared to the probability density with ARI. Additionally, the two bins directly below at negative vertical velocities display larger probability densities without ARI, whereas two bins around -0.05 m s^{-1} are enhanced with

ARI. Still, the differences between the two histograms are relatively small.
The histogram again shows that the presence of more and larger positive vertical wind velocities is related to ARI. The large similarity between the histograms is likely because the entire vertical columns (below 20 km) where a smoke plume is located are included. This inclusion leads to so many points being added to the histogram which are not directly affected by the plume and which are almost unchanged that the actual changes in the histogram are obscured. Only including points within the plume in terms of height does not seem to be a solution to this. As shown in Figure 6.4, many vertical velocity anomalies due to ARI occur below the plume and would not be captured when only selecting the actual plume location. Nevertheless, the differences in vertical wind velocities due to ARI can be identified and visualized.

6.3 Derivation of a lofting rate

For a more quantitative description of the lofting effects and a comparison with the literature, the lofting rate for the ARI + SHFL*6.8 experiment is derived. The mass-weighted height is not useful for this task, as it is heavily influenced by low-altitude emissions which have little impacts on the on the self-lofting as shown in Figure 6.3 panel (d) but reduce the overall mean of the heights. Therefore, we select values closer to the plume top. We have shown that the lofting is most evident not in the uppermost part of the plume but in that just below, where soot concentrations are higher. The AOD threshold that was previously used for the plume identification is set to a higher value to better catch this lower part of the plume. The threshold is multiplied by a factor 10 compared to the one before, such that points exceeding an AOD of 0.01 for the soot in the 550 nm wavelength are selected. The lofting is also less visible when using only the one highest point for each time step as the global plume top height, because the highest point tends to jump from one discrete height level to another (see Figure 5.1 panel (b) as an example for this). A better solution is to select a larger area along the plume top. Therefore, the largest height that includes a plume is calculated for each lon/lat point of the grid. The 100 highest such plume top heights are selected and their mean is calculated.
The self-lofting is illustrated in Figure 6.6. In panel (a), the difference of the mean of the 100 highest points is calculated for each time step compared to the next one. The result can be interpreted as an hourly lofting rate. The resulting curve includes many short-term fluctuations, but a daily oscillation between around $-0.03\,\mathrm{km\,h^{-1}}$ and $0.06\,\mathrm{km\,h^{-1}}$ becomes visible when smoothing the curve with a 6-hour moving average. The ascent of the plume top reaches its maximum velocity every day between 23:00 UTC and 04:00 UTC of the following day. This corresponds to 10:00 to 15:00 in Australian Eastern Daylight Time (AEDT). At these time around local noon, solar radiation is most intense and the atmosphere is most unstable. This diurnal oscillation reflects the pattern of the vertical velocities depicted in Figure 6.4 panel (b). This confirms that the mean of the 100 highest points shows a behavior which is in fact related to self-lofting and that we can use these points to derive a lofting rate.
Figure 6.6 panel (b) shows the mean of the 100 highest plume top heights. The curve exhibits a steep increase up to 13.1 km during the first two days, when pyroCb injection is the dominating

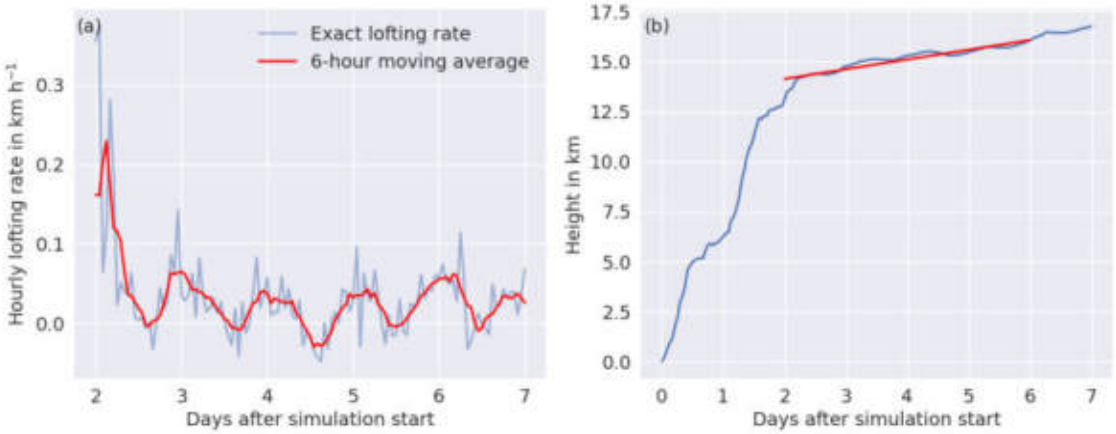

Figure 6.6: (a) Hourly lofting rate, defined as the difference between two consecutive mean heights of the 100 highest plume top heights (blue), with the 6-hour moving average (red). (b) Mean heights of the 100 highest plume top heights (blue), with a linear fit through the plume top heights between the 31st December and the 3rd January. The plume is defined here as points where the soot AOD in the 550 nm wavelength exceeds 0.01. Both plots are created from the ARI + SHFL*6.8 experiment results.

driver of the uplift. Then, an approximately linear increase with a lower slope manifests itself from day 3 to day 6. We attribute this effect to the self-lofting. We exclude the days 1, 2 and 7 due to the strong pyroCb activity on these days and perform a linear regression with scipy. With this linear fit, a lofting rate of $485 \pm 18\,\mathrm{m\,d^{-1}}$ can be derived.

Figure 13 in Ohneiser et al. (2023) depicts estimated self-lofting rates of around $350 \pm 50\,\mathrm{m}$ per day for the Australian wildfire plume during the first week of January 2020, which were derived from CALIOP images. This is lower than the value that was derived here. The differences between the lofting rates can be attributed to several uncertainties. First, Ohneiser et al. (2023) identified the layer center height of the Australian smoke layer to calculate their lofting rate from the CALIOP observations, which differs from the method to derive the lofting rate presented here. Second, our method produces varying lofting rates depending on which threshold is chosen to define the plume top. For example, if the threshold is reduced by 50% to an AOD of 0.005, the result for the lofting rate is only $448\,\mathrm{m\,d^{-1}}$. Lastly, there are several uncertainties about the plume optical properties in the model. The AOD of the plume depends on the soot emission flux. The issues related to this GFAS parameter and its enhancement factor have already been discussed. Additionally, the optical properties of the soot aerosol itself depend on assumptions about its composition, especially the BC/OC ratio.

Figure 6.7 illustrates the difference in the self-lofting between the ARI + SHFL*6.8 and the SHFL*6.8 experiment. It shows the mean and the standard deviation of the 100 highest plume top heights for both experiments. In the case without ARI, the mean height remains largely stable at around 13.5 km and even decreases down to 12.9 km after five simulation days. In the experiment with ARI, there is the almost linear increase between day 3 and day 6 which we have previously discussed.

The standard deviation is highest both with and without ARI during the first two simulation days, with mean values of 3.1 and 2.8 km, respectively. Over the next simulation days, the standard deviations decrease for both experiments, but more quickly when ARI is enabled. They reach a

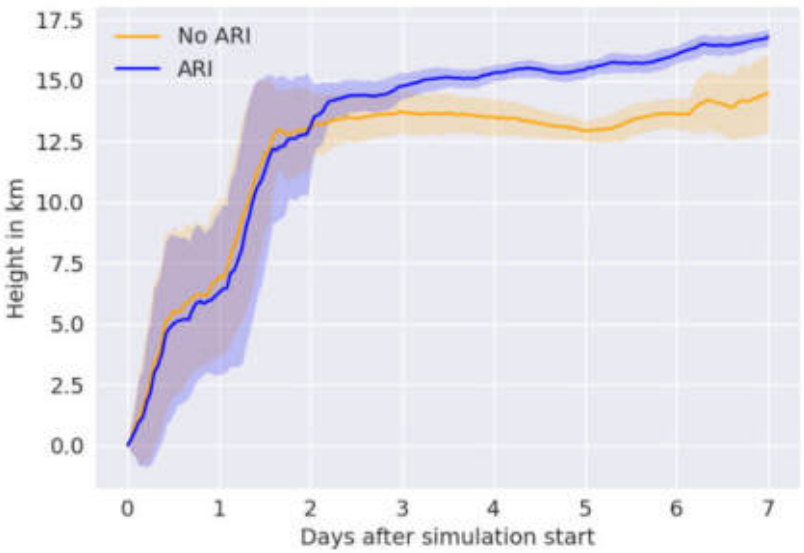

Figure 6.7: Mean (solid line) and standard deviation (semi-transparent bands) of the 100 highest plume top heights for the ARI + SHFL*6.8 experiment (blue) and the SHFL*6.8 experiment (orange). The plume is defined as points were the soot AOD in the 550 nm wavelength exceeds 0.01.

minimum value of 0.29 km in the ARI + SHFL*6.8 experiment and 0.39 km for the SHFL*6.8 experiment. During the seventh simulation day, the standard deviations increase again, mostly in the experiment without ARI where they reach 1.6 km at the end of the simulation time period.
The height decrease in the experiment without ARI is probably due to sedimentation. This is counteracted when ARI is enabled, which enables the plume to further ascend. A similar competition between lofting and sedimentation was observed by Muser et al. (2020) for the Raikoke plume. The standard deviations appear to be highest in time periods when the plume rise is dominated by pyroCb injection. As the plume height is calculated for each grid cell separately, this process likely varies on a more small-scale level. Conversely, when the smoke forms a distinct plume which moves up due to self-lofting, the standard deviation between the points inside it is decreased.

6.4 Impact of aerosol aging

In the following, the setup of the experiments is modified as described in section 4.5 to allow aerosol aging and to especially investigate the impacts the aging has on the aerosol optical properties and, in consequence, on the lofting rate. With the new setup the fires now emit the chemical trace gases CO, CH_4, NH_3, NO_2 and SO_2 and via chemical reactions, condensation and nucleation SO_4, NO_3 and NH_4 aerosols are produced.

6.4.1 Deriving new optical properties

Due to the newly produced species which condense onto the soot particles, a part of the soot shifts from the insoluble accumulation to the mixed accumulation mode. This means that the soot particles now have a liquid shell of the aforementioned species SO_4, NO_3 and NH_4 together with condensed water. The liquid shell impacts the aerosol optical properties. In Muth (2024), the optical properties of the mixed mode were derived based on a 10% coating fraction. In this thesis, both the additional emission of chemical trace gases and the simulation of a longer time period are expected to lead to more aging, so the coating fraction needs to be calculated again.
The coating fraction of an aerosol is defined as the diameter ratio between the coating and the entire particle. It is derived from the mass ratio

$$f_{\mathrm{m}} = \frac{m_{\mathrm{core}}}{m_{\mathrm{tot}}} \tag{6.1}$$

that can be converted to a volume ratio with the core and shell densities of the mixed particle. The core and shell densities are derived from the densities of their constituents with a volume averaging approach. The volume ratio is transformed into the diameter ratio $D_{\mathrm{core}}D_{\mathrm{tot}}^{-1}$, the coating fraction is then given by $1 - D_{\mathrm{core}}D_{\mathrm{tot}}^{-1}$.
To calculate the optical properties for the mixed accumulation mode, the median diameter d_{n} and the coating fraction are needed as input parameters. A preliminary simulation is run with aerosol aging to derive these two properties. Then, histograms for the coating fraction and the diameter of the plume points over all time steps are created. Points are part of the plume if they exceed a threshold soot (mixed + insoluble accumulation mode) concentration of $0.5\,\mu\mathrm{g\,m^{-3}}$. As shown in Figure 6.8, the median coating fraction is at around 14% and the median diameter is 151 nm.
It is important to note that the distribution of the coating fraction depends quite strongly on the choice of the threshold to identify the plume. As a test, the threshold was reduced to $0.05\,\mu\mathrm{g\,m^{-3}}$, which is the value that was chosen to analyze the plume mass weighted height such as in Figure 6.1. The coating fraction then has median values of around 19%. However, since areas of higher soot concentrations are more relevant for ARI processes and ultimately self-lofting, it is useful to mostly capture the part of the plume where higher concentrations are reached. For this reason, the plume threshold of $0.5\,\mu\mathrm{g\,m^{-3}}$ was chosen to derive the coating fractions for the plume optical properties.

The new optical properties for the soot mixed accumulation mode are derived from Mie calculations (Mätzler, 2002) for a coating fraction of 15% and a median diameter of 150 nm. The Mie

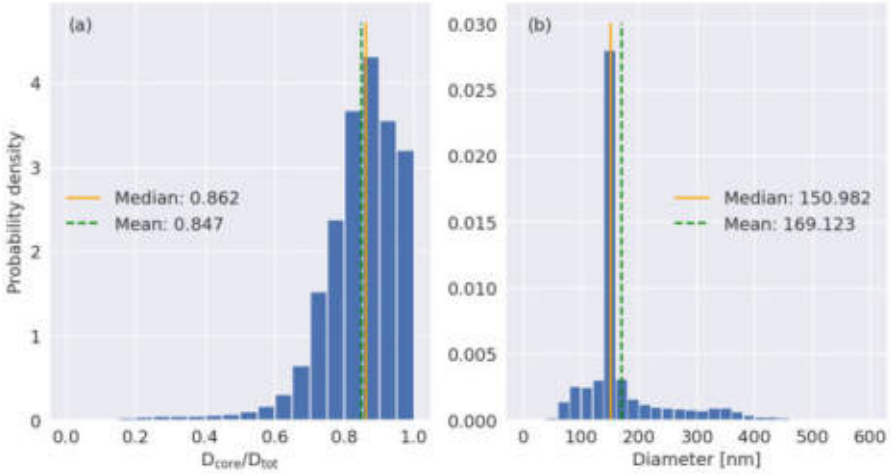

Figure 6.8: (a) Histogram of the (a) coating fraction and (b) size distribution of soot particles in the mixed accumulation mode after a first model run. Furthermore, the median (orange solid line) and the mean (green dashed line) value of each distribution is marked. Points from all time steps over the entire model run are included included into the histograms if they exceeded a threshold soot concentration above $0.5\,\mu g\,m^{-3}$. Soot is now the sum of the mixed accumulation and the insoluble accumulation mode.

calculations assume a core-shell state with the soot core BC/OC ratio of 3% and a shell of inorganic solution of sulfate-nitrate-water. The refractive indices are from the HITRAN 2022 dataset (Gordon et al., 2022). Figure 6.9 shows a comparison of the insoluble and the mixed accumulation mode with respect to the three radiative transfer parameters mass extinction coefficient k_{ext}, single scattering albedo ω and asymmetry parameter g.

The values for the extinction parameter start at $6.3\,m^2\,g^2$ for the mixed mode and $4.8\,m^2\,g^2$ for the accumulation mode at the smallest wavelengths between 263.2 and 200 nm and then decrease for larger wavelengths. k_{ext} is higher for the mixed accumulation mode across almost all wavelengths. This is consistent with the soluble shell enhancing the extinction of an absorptive core (Jacobson, 2000). The single scattering albedo first has values at around 0.8 for both modes, but it drops sharply between 10^3 and 10^4 nm wavelength. This means that at shorter wavelengths the light is more likely to be scattered, whereas in the infrared a large part is absorbed. At short wavelengths, the single scattering albedo of the mixed mode is above that of the insoluble mode, for longer wavelengths this order inverts. The asymmetry parameter has values of 0.76 for the mixed mode and 0.74 for the accumulation mode at the bin with the smallest wavelengths, then it declines as the wavelengths increase. This means that the short-wave radiation is predominantly forward-scattered, whereas the long-wave radiation is scattered more symmetrically into all directions. Both modes have very similar values for the asymmetry parameter across the entire wavelength spectrum.

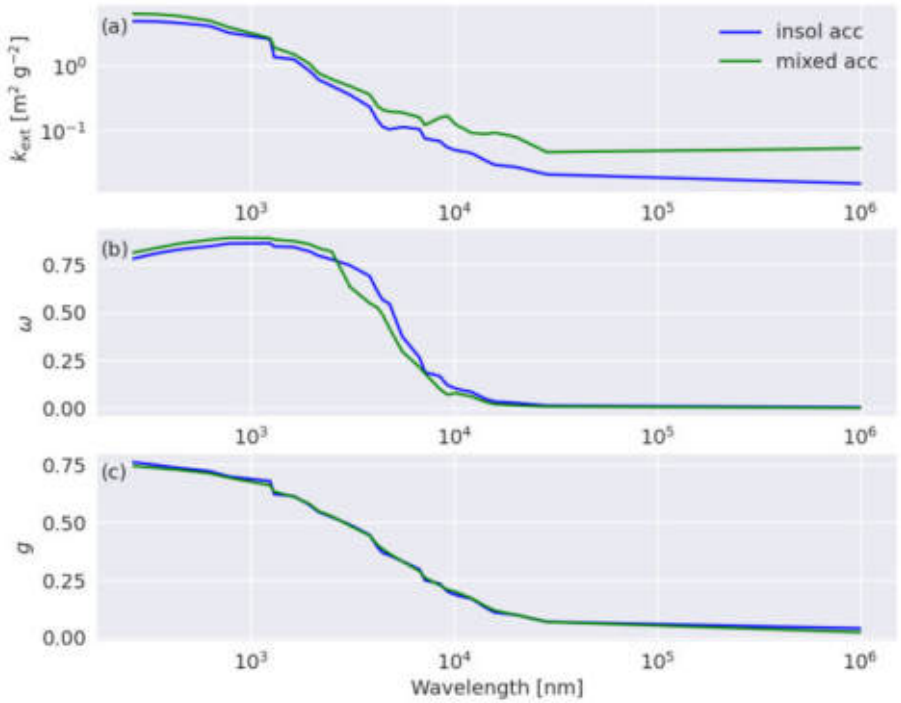

Figure 6.9: Optical properties of the soot insoluble and mixed accumulation modes, shown are (a) mass extinction coefficient k, (b) single scattering albedo ω and asymmetry parameter g at ecRad wavelengths. The curves in blue represent the insoluble accumulation mode and the ones in green the mixed accumulation mode.

6.4.2 Impact of new optical properties

When the new optical properties for the mixed mode are applied to the simulation, the self-lofting changes as a consequence of the modified absorption. Figure 6.10 illustrates this with the plume mass-weighted heights and top heights for the ARI + SHFL*6.8 experiment, where the two curves represent the setups with and without aerosol aging. The curve with aging displays a similar temporal evolution to the one without aging. Up to 29 h into the simulation, the MWH values are almost identical for both experiments. Starting from there, the experiment with aging exhibits continuously lower heights than the one without aging. The differences are on the order of magnitude of 100 m. On the fourth day of the simulation, the experiment with aging reaches its maximum value of 0.468 km, which is 70 m lower than in the experiment without aging.
In the plume top height, the two experiments appear even more similar. The top heights of both experiments rise to 18.2 km over the course of the simulation. Aside from some short-term fluctuations, the top heights for both experiments are often identical.
The lofting rate is calculated for the experiment with aerosol aging using the same strategy as described in 6.3 to serve as a comparison to the experiment without aging. We obtain a value for the self-lofting rate of 0.459 km d^{-1}. This is 5.4% lower than the previous result of 0.485 km d^{-1}.

The plume mass-weighted heights are very similar for both experiments during the first 1.5 days, which is expected because the changed radiative effects do not yet become very significant at this timescale. Although the extinction of soot in the mixed mode is higher than in the insoluble mode, the self-lofting and therefore the mass-weighted heights later in the experiment are reduced. A

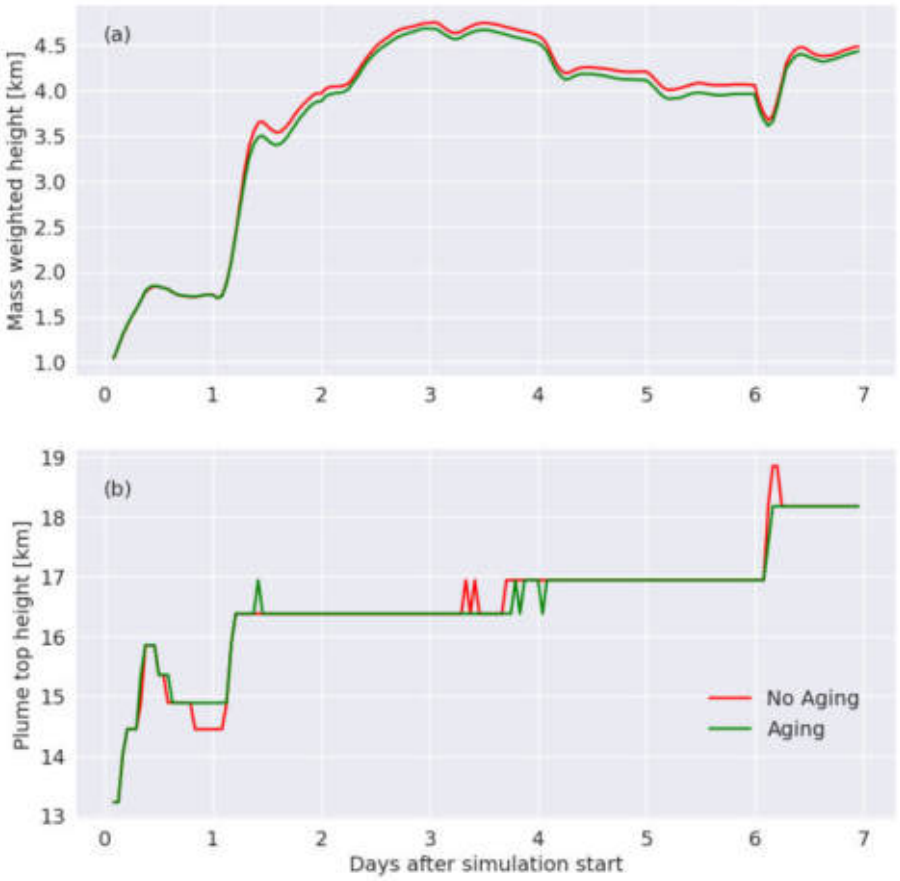

Figure 6.10: (a) Mass weighted height (b) top height of the plume for the ARI + SHFL*6.8 experiment with (green) and without (red) aging. For the mass weighted height, the plume is defined by a threshold of the sum of soot in the insoluble and mixed accumulation mode of 0.05 µg m^{-3}. For the top height, the plume is defined by the soot AOD of the 550 nm wavelength exceeding a value of 0.001.

possible explanation is the higher local stabilization of the atmosphere around the plume due to more warming caused by the increased extinction, which inhibits its ascent. However, the single scattering albedo is larger for the mixed mode than for the accumulation mode at short wavelengths, which could offset some of the effect of the extinction enhancement and reduce the warming due to ARI. The aging not only influences the optical properties of the aerosol, but it also leads to particle growth. Larger particles experience a faster sedimentation, which leads to a reduction in the mass-weighted heights.

The differences between the experiments with and without aging become even less visible when comparing the top heights. This is consistent with the Hovmöller diagram of the soot concentration Figure 6.3 that showed us that the largest part of the lofting does not happen at the plume top, but below. As a consequence, the plume top height is less influenced by changes in the aerosol optical properties. Additionally, the impact of the increase in sedimentation velocity is lower on the top height than on the mass-weighted height.

In conclusion, the addition of aerosol aging to the simulations reduces the ascent of the plume that is achieved via self-lofting, however this impact is not very significant.

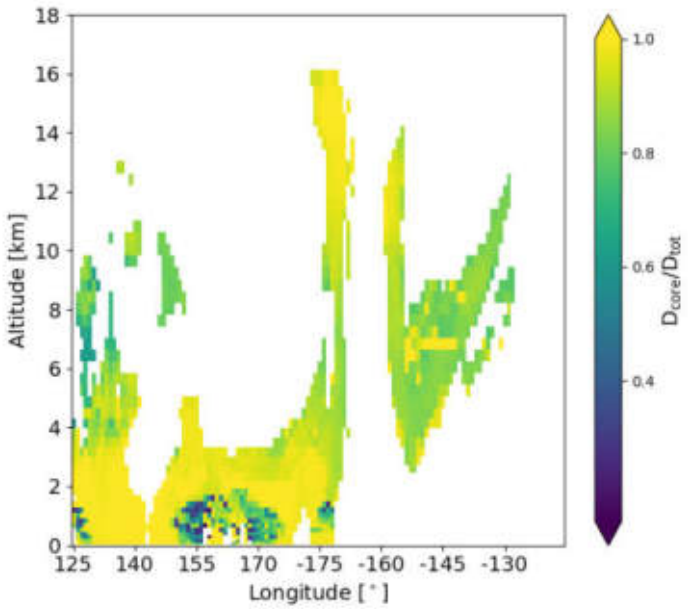

Figure 6.11: Cross section through the plume coating fractions at 36°S 120 h after simulation start. The plume was identified by the concentration of the sum of soot in the insoluble and mixed accumulation mode being above a threshold of 0.5 µg m^{-3}. The colors indicate the coating fraction $\frac{D_{\text{core}}}{D_{\text{tot}}}$ of the mixed soot particles inside the plume.

6.4.3 Height dependency of aerosol aging

Another aspect of simulating aerosol aging is to investigate the height dependency of the process. Figure 6.11 depicts an example of a plume cross section at 36°S 120 h after simulation start. The cross section contains the values of the coating fraction of plume points, which are points above the mixed and insoluble soot concentration threshold of 0.5 µg m^{-3}. For the lowermost heights below 4 km, the coating fraction values appear very noisy; they contain values from both ends of the range very closely together. In a height range between 4 and around 10 km, they are more homogeneous at values of around 15-20% coating fraction. Then, the highest part of the plume which extends to up to 16 km of height exhibits coating fractions close to 0%, which means that aerosol aging has not affected this part of the plume.

To get a more complete picture of this, high and low altitude plume points are selected for each time step. The high altitude plume points are assumed to be located between 300 and 150 hPa, whereas the low altitude points are between 700 and 500 hPa. Then, the coating fractions of the selected points are derived and their means and standard deviations are calculated for each time step.
Figure 6.12 shows the timeline of the mean coating fractions for plume points at higher versus lower altitudes together with their respective standard deviations. For all time steps the coating fractions at low altitudes exceed those at high altitudes, although the extent of this difference varies. The coating fraction curve reaches its minimum for the high altitude points at the end of the fourth day, where the coating fraction is below 10%. At the same time, the coating fraction of low altitude points is at 14%. Additionally, the standard deviation of the coating fractions for the lower altitude

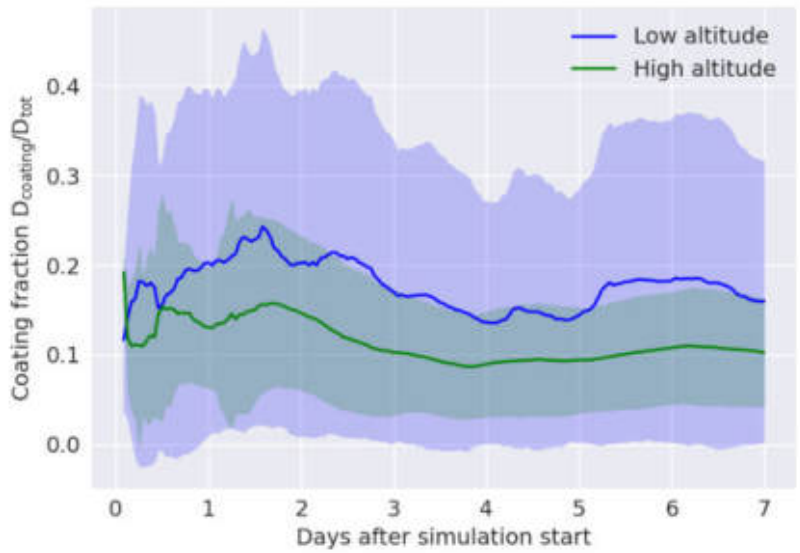

Figure 6.12: Mean coating fraction of plume points between 700 and 500 hPa (blue) and between 300 and 150 hPa (green). The plume is again identified by the concentration of the sum of soot in the insoluble and mixed accumulation mode being above a threshold of 0.5 µg m^{-3}. The standard deviations of both curves are shown as semi-transparent bands.

points are more than double those at higher altitudes.

It is important to note that the "low" altitude height range selected here already corresponds to altitudes between around 3 and 6 km. If a height range near the ground is selected, this part of the plume on average has lower coating fraction values than the high-altitude part. This is due to these points being located quite close to the emission sources and due to them containing the lowermost emissions which have not yet traveled for a long time and have not had a lot of time to age. So this trend of less aging at higher plume points is dependent on the definition of high and low plume points. The difference between the standard deviations of both curves reflects how the coating fraction values vary much more at lower heights in the cross section in Figure 6.11 and become more homogeneous with increasing height. This is probably also related to the close proximity of the low-altitude smoke to the emission sources.

The analysis confirms that the coating fraction is higher for the low-altitude points than for the high-altitude points. This is in agreement with Ohneiser et al. (2022) that identify a slow aging process of 2017 Canadian wildfire smoke due to dry conditions in the stratosphere and low availability of condensable gases.

7 Conclusions

In this thesis, I performed global simulations with a grid spacing of 80 km to analyze the emissions of aerosols and chemical trace gases during the Australian New Year event. Several simulations that differ in terms of whether and how much the sensible heat release due to the wildfire was enhanced were run. A new possibility for wildfires to emit chemical trace gases was implemented to ICON-ART and was validated against CO observations. Furthermore, the impact of aerosol-radiation interaction was investigated. A version of the experiment was created with emissions of several more trace gases, which react and contribute to aerosol aging.
The research questions can now be answered as follows:

1. The extreme injection heights of the 2019/2020 ANY event can be reached with the plume rise model in low-resolution simulations by adding the sensible heat release term developed by Muth (2024) and tuning it by a factor to counteract reductions in the vertical wind velocities due to the low resolution. A value of 6.8 has been empirically derived for the 80 km resolution, as it created results closest to satellite observations.

2. The aerosol-radiation interaction enables the smoke plume to further ascend after its initial injection. Its impact in the simulation depends critically on the injection height, which determines whether the smoke plume is located above or below cloud level. Differences in temperature and vertical wind can be detected in regions of the smoke plume by comparing experiments with and without aerosol-radiation interaction. A self-lofting rate of almost 500 m, which is larger than observations, was derived.

3. Due to aerosol aging, the soot particles exhibit a liquid coating. The coating fraction value of 15% and median diameter of 150 nm are derived to calculate new optical properties. The changes in the aerosol optical properties include, most notably, an enhanced extinction. The resulting self-lofting is lower than in a simulation without aerosol aging, which could be related to a faster sedimentation due to particle growth. Furthermore, we found the aging at large altitudes to be suppressed compared to lower altitudes.

The results were verified by comparisons with satellite data from several instruments. The model data showed good agreement compared to CALIOP cross sections and MODIS cloud top heights. The simulated column loads showed a stronger dilution compared to IASI CO column loads but matched the shape and distribution well. The comparison with MLS CO timelines for several pressure levels mostly failed, probably because the plume was shifted horizontally compared to observations. Considering the low spatial resolution of MLS, this makes it difficult to compare the model data along the satellite track with its observations.

7.1 Outlook

In this thesis, only seven days from the 29th December until the 4th January were simulated. This is sufficient to include both phases of ANY, but to really observe the effects of the second phase of ANY which occur with some time delay, it would be necessary to simulate a longer time period. Furthermore, this would enable to monitor the self-lofting of the plume originating from the first ANY phase for a longer time period and to observe how much the lofting rate is affected by the dilution of the plume over time. However, simulating a much longer time period would make it necessary to re-initialize the simulation. The reinitialization of the meteorological variables could reduce or eliminate the impact of aerosol radiation, especially on temperature and vertical wind, which are essential for lofting.

As the emission of chemical trace gases by wildfires has been added to ICON-ART, this sets a good foundation to emit more chemical trace gases - there are many more available in the GFAS dataset - and to apply a more complex chemistry mechanism than lifetime and OH chemistry which have been used in this thesis. For example, it would be interesting to focus on ozone depletion in the stratosphere. Since the injection heights have successfully been increased, this enables the smoke plume to actually reach the stratosphere and have impacts on stratospheric composition. This connects to the first point about simulating an extended time period, as the ozone chemistry occurring on a too large time scale was another reason why it was not possible to simulate this effect in the scope of this thesis.

The implementation of chemical trace gas emission to the plume-rise model also enables us to emit VOCs within simulations. Due to photochemical aging, these precursors can form secondary organic aerosol (He et al., 2024), which could then be investigated with ICON-ART.

The enhancement factor for the sensible heat release has so far only been empirically derived for the 80 km resolution. By comparing simulations with different ICON grids, the resolution-dependency can be further investigated to find a better way of deriving the optimal value for the enhancement factor than just testing several values and comparing them against satellite images. For example, the wildfire sensible heat release term could be tuned for experiments with 13 km or 40 km grids, which are less coarse and thus have higher vertical wind velocity values, but which are still unable to explicitly resolve convection. If our assumptions are correct, these experiments would need a lower enhancement factor to reproduce realistic injection heights. Maybe it would be possible to identify a link between the ratio of the different resolutions and the ratio of the respective enhancements that are required.

In future experiments, MieAI (Kumar et al., 2024) could be used to calculate the optical properties of the internally mixed aerosols that are produced by aerosol aging in the experiments from this thesis. MieAI uses a neural network to emulate Mie calculations online in the model. This permits to account for spatial and temporal variability in the coating fractions and particle sizes, compared to look-up tables from offline Mie calculations that contain fixed assumptions about these properties.

8 Abbreviations

ANY Australian New Year

AOD aerosol optical depth

ARI aerosol-radiation-interaction

ART Aerosol and Reactive Trace gases

BC black carbon

C2SM Center for Climate Systems Modeling

CALIOP Cloud-Aerosol Lidar with Orthogonal Polarization

CCN cloud condensation nuclei

DKRZ German Climate Computing Center

DWD German Weather Service, Deutscher Wetterdienst

FRP Fire Radiative Power

GFAS Global Fire Assimilation System

IASI Infrared Atmospheric Sounding Interferometer

ICON ICOsahedral Nonhydrostatic

IN ice nuclei

KIT Karlsruhe Institute of Technology

LINOZ linearized ozone chemistry

MLS Microwave Limb Sounder

MODIS Moderate Resolution Imaging Spectroradiometer

MPI-M Max Planck Institute for Meteorology

NWP Numerical Weather Prediction

OC organic carbon

PDF probability density function

pyroCb pyrocumulonimbus

RF radiative forcing

SSA single scattering albedo

UTLS upper troposphere - lower stratosphere

Bibliography

Akagi, S. K., R. J. Yokelson, C. Wiedinmyer, M. J. Alvarado, J. S. Reid, T. Karl, J. D. Crounse, and P. O. Wennberg, 2011: Emission factors for open and domestic biomass burning for use in atmospheric models. *Atmospheric Chemistry and Physics*, **11 (9)**, 4039–4072, https://doi.org/10.5194/acp-11-4039-2011.

Albrecht, B. A., 1989: Aerosols, Cloud Microphysics, and Fractional Cloudiness. *Science*, **245 (4923)**, 1227–1230, https://doi.org/10.1126/science.245.4923.1227.

Baum, B. A., W. P. Menzel, R. A. Frey, D. C. Tobin, R. E. Holz, S. A. Ackerman, A. K. Heidinger, and P. Yang, 2012: MODIS Cloud-Top Property Refinements for Collection 6. *Journal of Applied Meteorology and Climatology*, **51 (6)**, 1145–1163, https://doi.org/10.1175/JAMC-D-11-0203.1.

Bernath, P., C. Boone, and J. Crouse, 2022: Wildfire smoke destroys stratospheric ozone. *Science*, **375 (6586)**, 1292–1295, https://doi.org/10.1126/science.abm5611.

Boer, M. M., V. Resco De Dios, and R. A. Bradstock, 2020: Unprecedented burn area of Australian mega forest fires. *Nature Climate Change*, **10 (3)**, 171–172, https://doi.org/10.1038/s41558-020-0716-1.

Boers, R., A. T. De Laat, D. C. Stein Zweers, and R. J. Dirksen, 2010: Lifting potential of solar-heated aerosol layers. *Geophysical Research Letters*, **37 (24)**, 2010GL045 171, https://doi.org/10.1029/2010GL045171.

Boucher, O., 2015: *Atmospheric Aerosols: Properties and Climate Impacts*. Springer Netherlands, Dordrecht, https://doi.org/10.1007/978-94-017-9649-1.

Bowman, D. M. J. S., and Coauthors, 2009: Fire in the Earth System. *Science*, **324 (5926)**, 481–484, https://doi.org/10.1126/science.1163886.

Bradstock, R. A., 2010: A biogeographic model of fire regimes in Australia: current and future implications. *Global Ecology and Biogeography*, **19 (2)**, 145–158, https://doi.org/10.1111/j.1466-8238.2009.00512.x.

Buchholz, R. R., L. K. Emmons, S. Tilmes, and The CESM2 Development Team, 2019: CESM2.1/CAM-chem Instantaneous Output for Boundary Conditions. UCAR/NCAR - Atmospheric Chemistry Observations and Modeling Laboratory, accessed 25.09.2024, https://doi.org/10.5065/NMP7-EP60.

Bègue, N., and Coauthors, 2021: Transport and Variability of Tropospheric Ozone over Oceania and Southern Pacific during the 2019–20 Australian Bushfires. *Remote Sensing*, **13 (16)**, 3092, https://doi.org/10.3390/rs13163092.

Campbell, P. C., D. Tong, R. Saylor, Y. Li, S. Ma, X. Zhang, S. Kondragunta, and F. Li, 2022: Pronounced increases in nitrogen emissions and deposition due to the historic 2020 wildfires in the western U.S. *Science of The Total Environment*, **839**, 156 130, https://doi.org/10.1016/j.scitotenv.2022.156130.

Cascio, W. E., 2018: Wildland fire smoke and human health. *Science of The Total Environment*, **624**, 586–595, https://doi.org/10.1016/j.scitotenv.2017.12.086.

Chand, D., R. Wood, T. L. Anderson, S. K. Satheesh, and R. J. Charlson, 2009: Satellite-derived direct radiative effect of aerosols dependent on cloud cover. *Nature Geoscience*, **2 (3)**, 181–184, https://doi.org/10.1038/ngeo437.

Clerbaux, C., and Coauthors, 2009: Monitoring of atmospheric composition using the thermal infrared IASI/MetOp sounder. *Atmospheric Chemistry and Physics*, **9 (16)**, 6041–6054, https://doi.org/10.5194/acp-9-6041-2009.

Copernicus Atmosphere Monitoring Service, 2021: CAMS global biomass burning emissions based on fire radiative power (GFAS). URL https://ads.atmosphere.copernicus.eu/datasets/cams-global-fire-emissions-gfas?tab=overview, accessed 25.09.2024.

Di Virgilio, G., J. P. Evans, S. A. P. Blake, M. Armstrong, A. J. Dowdy, J. Sharples, and R. McRae, 2019: Climate Change Increases the Potential for Extreme Wildfires. *Geophysical Research Letters*, **46 (14)**, 8517–8526, https://doi.org/10.1029/2019GL083699.

Edwards, D. P., and Coauthors, 2006: Satellite-observed pollution from Southern Hemisphere biomass burning. *Journal of Geophysical Research: Atmospheres*, **111 (D14)**, https://doi.org/10.1029/2005jd006655.

Emmons, L. K., and Coauthors, 2020: The Chemistry Mechanism in the Community Earth System Model Version 2 (CESM2). *Journal of Advances in Modeling Earth Systems*, **12 (4)**, e2019MS001 882, https://doi.org/10.1029/2019MS001882.

Fisher, J. A., S. R. Wilson, G. Zeng, J. E. Williams, L. K. Emmons, R. L. Langenfelds, P. B. Krummel, and L. P. Steele, 2015: Seasonal changes in the tropospheric carbon monoxide profile over the remote Southern Hemisphere evaluated using multi-model simulations and aircraft observations. *Atmospheric Chemistry and Physics*, **15 (6)**, 3217–3239, https://doi.org/10.5194/acp-15-3217-2015.

Fountoukis, C., and A. Nenes, 2007: ISORROPIA II: a computationally efficient thermodynamic equilibrium model for K-Ca-Mg-NH4-Na-SO4-NO3-Cl-H2O aerosols. *Atmos. Chem. Phys.*, **7**, 4639–4659.

Freitas, S. R., K. M. Longo, and M. O. Andreae, 2006: Impact of including the plume rise of vegetation fires in numerical simulations of associated atmospheric pollutants. *Geophysical Research Letters*, **33 (17)**, 2006GL026 608, https://doi.org/10.1029/2006GL026608.

Freitas, S. R., and Coauthors, 2007: Including the sub-grid scale plume rise of vegetation fires in low resolution atmospheric transport models. *Atmospheric Chemistry and Physics*, **7 (13)**, 3385–3398, https://doi.org/10.5194/acp-7-3385-2007.

Gassmann, A., and H. Herzog, 2008: Towards a consistent numerical compressible non-hydrostatic model using generalized Hamiltonian tools. *Quarterly Journal of the Royal Meteorological Society*, **134 (635)**, 1597–1613, https://doi.org/10.1002/qj.297.

Gordon, I., and Coauthors, 2022: The HITRAN2020 molecular spectroscopic database. *Journal of Quantitative Spectroscopy and Radiative Transfer*, **277**, 107 949, https://doi.org/10.1016/j.jqsrt.2021.107949.

Hansen, J., M. Sato, and R. Ruedy, 1997: Radiative forcing and climate response. *Journal of Geophysical Research*, **102**, 6831–6864.

He, Y., and Coauthors, 2024: Formation of secondary organic aerosol from wildfire emissions enhanced by long-time ageing. *Nature Geoscience*, **17 (2)**, 124–129, https://doi.org/10.1038/s41561-023-01355-4.

Heinold, B., and Coauthors, 2022: Important role of stratospheric injection height for the distribution and radiative forcing of smoke aerosol from the 2019–2020 Australian wildfires. *Atmospheric Chemistry and Physics*, **22 (15)**, 9969–9985, https://doi.org/10.5194/acp-22-9969-2022.

Hogan, R. J., and A. Bozzo, 2018: A Flexible and Efficient Radiation Scheme for the ECMWF Model. *Journal of Advances in Modeling Earth Systems*, **10 (8)**, 1990–2008, https://doi.org/10.1029/2018MS001364.

Holton, J. R., 2004: Chapter 2 Basic conservation laws. *An Introduction to Dynamic Meteorology*, International Geophysics, Vol. 88, Elsevier, 28–56, https://doi.org/10.1016/S0074-6142(04)80036-6.

Jacob, D. J., 1986: Chemistry of OH in remote clouds and its role in the production of formic acid and peroxymonosulfate. *Journal of Geophysical Research: Atmospheres*, **91 (D9)**, 9807–9826, https://doi.org/10.1029/JD091iD09p09807.

Jacobson, M. Z., 2000: A physically-based treatment of elemental carbon optics: Implications for global direct forcing of aerosols. *Geophysical Research Letters*, **27 (2)**, 217–220, https://doi.org/10.1029/1999GL010968.

Jaffe, D. A., and N. L. Wigder, 2012: Ozone production from wildfires: A critical review. *Atmospheric Environment*, **51**, 1–10, https://doi.org/10.1016/j.atmosenv.2011.11.063.

Jones, P. W., 1999: First- and Second-Order Conservative Remapping Schemes for Grids in Spherical Coordinates. *Monthly Weather Review*, **127 (9)**, 2204–2210, https://doi.org/10.1175/1520-0493(1999)127<2204:FASOCR>2.0.CO;2.

Kablick, G. P., D. R. Allen, M. D. Fromm, and G. E. Nedoluha, 2020: Australian PyroCb Smoke Generates Synoptic-Scale Stratospheric Anticyclones. *Geophysical Research Letters*, **47 (13)**, e2020GL088 101, https://doi.org/10.1029/2020GL088101.

Kahn, R. A., W. Li, C. Moroney, D. J. Diner, J. V. Martonchik, and E. Fishbein, 2007: Aerosol source plume physical characteristics from space-based multiangle imaging. *Journal of Geophysical Research: Atmospheres*, **112 (D11)**, 2006JD007 647, https://doi.org/10.1029/2006JD007647.

Kaiser, J. W., and Coauthors, 2012: Biomass burning emissions estimated with a global fire assimilation system based on observed fire radiative power. *Biogeosciences*, **9 (1)**, 527–554, https://doi.org/10.5194/bg-9-527-2012.

Khaykin, S., and Coauthors, 2020: The 2019/20 Australian wildfires generated a persistent smoke-charged vortex rising up to 35 km altitude. *Communications Earth & Environment*, **1 (1)**, 22, https://doi.org/10.1038/s43247-020-00022-5.

Kloss, C., and Coauthors, 2021: Australian Fires 2019–2020: Tropospheric and Stratospheric Pollution Throughout the Whole Fire Season. *Frontiers in Environmental Science*, **9**, 652 024, https://doi.org/10.3389/fenvs.2021.652024.

Koch, D., and A. D. Del Genio, 2010: Black carbon semi-direct effects on cloud cover: review and synthesis. *Atmospheric Chemistry and Physics*, **10 (16)**, 7685–7696, https://doi.org/10.5194/acp-10-7685-2010, publisher: Copernicus GmbH.

Kumar, P., H. Vogel, J. Bruckert, L. J. Muth, and G. A. Hoshyaripour, 2024: MieAI: a neural network for calculating optical properties of internally mixed aerosol in atmospheric models. *npj Climate and Atmospheric Science*, **7 (1)**, 110, https://doi.org/10.1038/s41612-024-00652-y.

Levin, N., M. Yebra, and S. Phinn, 2021: Unveiling the Factors Responsible for Australia's Black Summer Fires of 2019/2020. *Fire*, **4 (3)**, 58, https://doi.org/10.3390/fire4030058.

Livesey, N., and Coauthors, 2022: Aura Microwave Limb Sounder (MLS) Version 5.0x Level 2 and 3 data quality and description document. Jet Propulsion Laboratory, URL https://mls.jpl.nasa.gov/data/v5-0_data_quality_document.pdf.

Lohmann, U., and J. Feichter, 2005: Global indirect aerosol effects: a review. *Atmospheric Chemistry and Physics*, **5 (3)**, 715–737, https://doi.org/10.5194/acp-5-715-2005.

Luderer, G., J. Trentmann, T. Winterrath, C. Textor, M. Herzog, H. F. Graf, and M. O. Andreae, 2006: Modeling of biomass smoke injection into the lower stratosphere by a large forest fire (Part II): sensitivity studies. *Atmospheric Chemistry and Physics*, **6 (12)**, 5261–5277, https://doi.org/10.5194/acp-6-5261-2006.

McLinden, C. A., S. C. Olsen, B. Hannegan, O. Wild, M. J. Prather, and J. Sundet, 2000: Stratospheric ozone in 3-D models: A simple chemistry and the cross-tropopause flux. *Journal of Geophysical Research: Atmospheres*, **105 (D11)**, 14 653–14 665, https://doi.org/10.1029/2000JD900124.

MODIS Atmosphere Science Team, 2017a: MODIS/Terra Clouds 5-Min L2 Swath 1km and 5km. NASA Level 1 and Atmosphere Archive and Distribution System Distributed Active Archive Center, URL https://ladsweb.modaps.eosdis.nasa.gov/missions-and-measurements/products/MOD06_L2, accessed 29.08.2024, https://doi.org/10.5067/MODIS/MOD06_L2.061.

MODIS Atmosphere Science Team, 2017b: MYD06_l2 MYD06_l2 MODIS/Aqua Clouds 5-Min L2 Swath 1km and 5km. NASA Level 1 and Atmosphere Archive and Distribution System Distributed Active Archive Center, URL https://ladsweb.modaps.eosdis.nasa.gov/missions-and-measurements/products/MYD06_L2, accessed 29.08.2024, https://doi.org/10.5067/MODIS/MYD06_L2.061.

Morgan, G. W., and Coauthors, 2020: Prescribed burning in south-eastern Australia: history and future directions. *Australian Forestry*, **83 (1)**, 4–28, https://doi.org/10.1080/00049158.2020.1739883.

Morgan, M. G., P. J. Adams, and D. W. Keith, 2006: Elicitation of Expert Judgments of Aerosol Forcing. *Climatic Change*, **75 (1-2)**, 195–214, https://doi.org/10.1007/s10584-005-9025-y.

Murphy, B. P., and Coauthors, 2013: Fire regimes of Australia: a pyrogeographic model system. *Journal of Biogeography*, **40 (6)**, 1048–1058, https://doi.org/10.1111/jbi.12065.

Muser, L. O., and Coauthors, 2020: Particle aging and aerosol–radiation interaction affect volcanic plume dispersion: evidence from the Raikoke 2019 eruption. *Atmospheric Chemistry and Physics*, **20 (23)**, 15 015–15 036, https://doi.org/10.5194/acp-20-15015-2020.

Muth, L. J., 2024: Numerical Simulations of the Black Summer Fires: Impact of Moisture, Sensible Heat Release and Aerosol-Radiation Interaction on the Smoke Plume and Cloud Formation. Karlsruher Institut für Technologie (KIT), https://doi.org/10.5445/IR/1000175467.

Mätzler, C., 2002: MATLAB functions for Mie scattering and absorption, version 2. *IAP Res Rep*, **8**, 1–24.

NASA Earth Science Data and Information System (ESDIS), ????: NASA Worldview Snapshot. URL https://worldview.earthdata.nasa.gov/?v=111.74239759111286,-62.376971713447006,220.90985540823465,-10.37950427436904&l=Coastlines_15m,MODIS_Combined_Thermal_Anomalies_All,MODIS_Aqua_CorrectedReflectance_TrueColor&lg=true&t=2019-12-31-T11%3A40%3A45Z, accessed 18.12.2024.

Novakov, T., S. Menon, T. W. Kirchstetter, D. Koch, and J. E. Hansen, 2005: Aerosol organic carbon to black carbon ratios: Analysis of published data and implications for climate forcing. *Journal of Geophysical Research: Atmospheres*, **110 (D21)**, 2005JD005 977, https://doi.org/

10.1029/2005JD005977.

Ohneiser, K., A. Ansmann, J. Witthuhn, H. Deneke, A. Chudnovsky, G. Walter, and F. Senf, 2023: Self-lofting of wildfire smoke in the troposphere and stratosphere: simulations and space lidar observations. *Atmospheric Chemistry and Physics*, **23 (4)**, 2901–2925, https://doi.org/10.5194/acp-23-2901-2023.

Ohneiser, K., and Coauthors, 2022: Australian wildfire smoke in the stratosphere: the decay phase in 2020/2021 and impact on ozone depletion. *Atmospheric Chemistry and Physics*, **22 (11)**, 7417–7442, https://doi.org/10.5194/acp-22-7417-2022.

Paugam, R., M. Wooster, S. Freitas, and M. Val Martin, 2016: A review of approaches to estimate wildfire plume injection height within large-scale atmospheric chemical transport models. *Atmospheric Chemistry and Physics*, **16 (2)**, 907–925, https://doi.org/10.5194/acp-16-907-2016.

Peterson, D. A., J. R. Campbell, E. J. Hyer, M. D. Fromm, G. P. Kablick, J. H. Cossuth, and M. T. DeLand, 2018: Wildfire-driven thunderstorms cause a volcano-like stratospheric injection of smoke. *npj Climate and Atmospheric Science*, **1 (1)**, 30, https://doi.org/10.1038/s41612-018-0039-3.

Peterson, D. A., E. J. Hyer, J. R. Campbell, J. E. Solbrig, and M. D. Fromm, 2017: A Conceptual Model for Development of Intense Pyrocumulonimbus in Western North America. *Monthly Weather Review*, **145 (6)**, 2235–2255, https://doi.org/10.1175/MWR-D-16-0232.1.

Peterson, D. A., and Coauthors, 2021: Australia's Black Summer pyrocumulonimbus super outbreak reveals potential for increasingly extreme stratospheric smoke events. *npj Climate and Atmospheric Science*, **4 (1)**, 38, https://doi.org/10.1038/s41612-021-00192-9.

Radke, L. F., J. H. Lyons, P. V. Hobbs, and R. E. Weiss, 1990: Smokes from the burning of aviation fuel and their self-lofting by solar heating. *Journal of Geophysical Research: Atmospheres*, **95 (D9)**, 14 071–14 076, https://doi.org/10.1029/JD095iD09p14071.

Raes, F., R. V. Dingenen, E. Vignati, J. Wilson, J.-P. Putaud, J. H. Seinfeld, and P. Adams, 2000: Formation and cycling of aerosols in the global troposphere. *Atmospheric Environment*, **34 (25)**, 4215–4240, https://doi.org/10.1016/S1352-2310(00)00239-9.

Raschendorfer, M., 2001: The new turbulence parameterization of LM. *COSMO Newsletter*, **1**, 89–97.

Reid, J. S., R. Koppmann, T. F. Eck, and D. P. Eleuterio, 2005: A review of biomass burning emissions part II: intensive physical properties of biomass burning particles. *Atmospheric Chemistry and Physics*, **5 (3)**, 799–825, https://doi.org/10.5194/acp-5-799-2005.

Rickly, P. S., and Coauthors, 2022: Emission factors and evolution of SO2 measured from biomass burning in wildfires and agricultural fires. *Atmospheric Chemistry and Physics*, **22 (23)**, 15 603–15 620, https://doi.org/10.5194/acp-22-15603-2022.

Rieger, D., and Coauthors, 2015: ICON–ART 1.0 – a new online-coupled model system from the global to regional scale. *Geoscientific Model Development*, **8 (6)**, 1659–1676, https://doi.org/10.5194/gmd-8-1659-2015.

Rodriguez, B., N. P. Lareau, D. E. Kingsmill, and C. B. Clements, 2020: Extreme Pyroconvective Updrafts During a Megafire. *Geophysical Research Letters*, **47 (18)**, e2020GL089 001, https://doi.org/10.1029/2020GL089001.

Rosenfeld, D., M. Fromm, J. Trentmann, G. Luderer, M. O. Andreae, and R. Servranckx, 2007: The Chisholm firestorm: observed microstructure, precipitation and lightning activity of a pyrocumulonimbus. *Atmospheric Chemistry and Physics*, **7 (3)**, 645–659, https://doi.org/10.5194/acp-7-645-2007.

Schreier, S. F., A. Richter, J. W. Kaiser, and J. P. Burrows, 2014: The empirical relationship between satellite-derived tropospheric NO2 and fire radiative power and possible implications for fire emission rates of NOx. *Atmospheric Chemistry and Physics*, **14 (5)**, 2447–2466, https://doi.org/10.5194/acp-14-2447-2014.

Schröter, J., and Coauthors, 2018: ICON-ART 2.1: a flexible tracer framework and its application for composition studies in numerical weather forecasting and climate simulations. *Geoscientific Model Development*, **11 (10)**, 4043–4068, https://doi.org/10.5194/gmd-11-4043-2018.

Seinfeld, J. H., and S. N. Pandis, 2016: *Atmospheric chemistry and physics: from air pollution to climate change*, third edition ed., John Wiley & Sons, Hoboken, New Jersey, p.18–54, 448–449, 544, 635.

Sellitto, P., R. Belhadji, C. Kloss, and B. Legras, 2022: Radiative impacts of the Australian bushfires 2019–2020 – Part 1: Large-scale radiative forcing. *Atmospheric Chemistry and Physics*, **22 (14)**, 9299–9311, https://doi.org/10.5194/acp-22-9299-2022.

Tarshish, N., and D. M. Romps, 2022: Latent Heating Is Required for Firestorm Plumes to Reach the Stratosphere. *Journal of Geophysical Research: Atmospheres*, **127 (18)**, e2022JD036 667, https://doi.org/10.1029/2022JD036667.

Thornhill, G. D., and Coauthors, 2021: Effective radiative forcing from emissions of reactive gases and aerosols – a multi-model comparison. *Atmospheric Chemistry and Physics*, **21 (2)**, 853–874, https://doi.org/10.5194/acp-21-853-2021.

Trentmann, J., G. Luderer, T. Winterrath, M. D. Fromm, R. Servranckx, C. Textor, M. Herzog, and M. O. Andreae, 2006: Modeling of biomass smoke injection into the lower stratosphere by a large forest fire (Part I): reference simulation. *Atmos. Chem. Phys.*

Twomey, S., 1974: Pollution and the planetary albedo. *Atmospheric Environment*, **8 (12)**, 1251–1256.

Val Martin, M., R. A. Kahn, J. A. Logan, R. Paugam, M. Wooster, and C. Ichoku, 2012: Space-based observational constraints for 1-D fire smoke plume-rise models. *Journal of Geophysical*

Research: Atmospheres, **117 (D22)**, 2012JD018 370, https://doi.org/10.1029/2012JD018370.

Val Martín, M., R. E. Honrath, R. C. Owen, G. Pfister, P. Fialho, and F. Barata, 2006: Significant enhancements of nitrogen oxides, black carbon, and ozone in the North Atlantic lower free troposphere resulting from North American boreal wildfires. *Journal of Geophysical Research: Atmospheres*, **111 (D23)**, 2006JD007 530, https://doi.org/10.1029/2006JD007530.

Viegas, D. X., 1998: Convective Processes in Forest Fires. *Buoyant Convection in Geophysical Flows*, E. J. Plate, E. E. Fedorovich, D. X. Viegas, and J. C. Wyngaard, Eds., Springer Netherlands, Dordrecht, 401–420, https://doi.org/10.1007/978-94-011-5058-3_17.

Voulgarakis, A., M. E. Marlier, G. Faluvegi, D. T. Shindell, K. Tsigaridis, and S. Mangeon, 2015: Interannual variability of tropospheric trace gases and aerosols: The role of biomass burning emissions. *Journal of Geophysical Research: Atmospheres*, **120 (14)**, 7157–7173, https://doi.org/10.1002/2014jd022926.

Walter, C., S. R. Freitas, C. Kottmeier, I. Kraut, D. Rieger, H. Vogel, and B. Vogel, 2016: The importance of plume rise on the concentrations and atmospheric impacts of biomass burning aerosol. *Atmospheric Chemistry and Physics*, **16 (14)**, 9201–9219, https://doi.org/10.5194/acp-16-9201-2016.

Waters, J., and Coauthors, 2006: The Earth observing system microwave limb sounder (EOS MLS) on the aura Satellite. *IEEE Transactions on Geoscience and Remote Sensing*, **44 (5)**, 1075–1092, https://doi.org/10.1109/TGRS.2006.873771.

Weimer, M., and Coauthors, 2017: An emission module for ICON-ART 2.0: implementation and simulations of acetone. *Geoscientific Model Development*, **10 (6)**, 2471–2494, https://doi.org/10.5194/gmd-10-2471-2017.

Whitby, K. T., 1978: The physical characteristics of sulfur aerosols. *Atmospheric Environment (1967)*, **12 (1-3)**, 135–159, https://doi.org/10.1016/0004-6981(78)90196-8.

Winker, D., 2022: CALIPSO Lidar Level 1B profile data, V4-51. NASA Langley Atmospheric Science Data Center Distributed Active Archive Center, URL https://asdc.larc.nasa.gov/project/CALIPSO/CAL_LID_L1-Standard-V4-51_V4-51, accessed 26.06.2024, https://doi.org/10.5067/CALIOP/CALIPSO/CAL_LID_L1-STANDARD-V4-51.

Winker, D. M., M. A. Vaughan, A. Omar, Y. Hu, K. A. Powell, Z. Liu, W. H. Hunt, and S. A. Young, 2009: Overview of the CALIPSO Mission and CALIOP Data Processing Algorithms. *Journal of Atmospheric and Oceanic Technology*, **26 (11)**, 2310–2323, https://doi.org/10.1175/2009JTECHA1281.1.

Zheng, Y., J. Liu, H. Jian, X. Fan, and F. Yan, 2021: Fire Diurnal Cycle Derived from a Combination of the Himawari-8 and VIIRS Satellites to Improve Fire Emission Assessments in Southeast Australia. *Remote Sensing*, **13 (15)**, 2852, https://doi.org/10.3390/rs13152852.

Zängl, G., D. Reinert, P. Rípodas, and M. Baldauf, 2015: The ICON (ICOsahedral Non-hydrostatic) modelling framework of DWD and MPI-M : Description of the non-hydrostatic dynamical core. *Quarterly Journal of the Royal Meteorological Society*, **141 (687)**, 563–579, https://doi.org/10.1002/qj.2378.

Acknowledgments

This study contains modified Copernicus Atmosphere Monitoring Service information [2023]. We acknowledge the use of imagery from the NASA Worldview application (`https://worldview.earthdata.nasa.gov`), part of the NASA Earth Science Data and Information System (ESDIS). The MODIS Cloud Top Height datasets are available from the Level-1 Atmosphere Archive and Distribution System (LAADS) Distributed Active Archive Center (DAAC), located in the Goddard Space Flight Center (`https://ladsweb.modaps.eosdis.nasa.gov/`). The CALIPSO datasets were acquired from the Atmospheric Science Data Center (ASDC) of the NASA Langley Research Center (`https://asdc.larc.nasa.gov/`).
I would like to thank Alexandra Laeng from IMKASF for providing me with the CO timeline data from MLS measurements and for providing me with useful insights on ways to compare the data with my model results.

Special thanks

First of all, I would like to thank the entire working group for being so welcoming towards me, I really enjoyed my time with you! Hervorheben möchte ich Dr. Julia Bruckert, Katerina Kusakova und Dr. Sven Werchner, die mir bei mehreren Fragen sehr gut weiterhelfen konnten. Außerdem danke an Prof. Dr. Corinna Hoose und Prof. Dr. Peter Braesicke, für die Übernahme der Rollen als Referentin bzw. Koreferent und ihren wertvollen Input nach meinem Spezialisierungsphasen-Vortrag.
Ein ganz besonders großes Dankeschön geht an Dr. Lisa Muth, die mir so oft bei Fehlersuchen in meinem Code weiterhelfen konnte und an Dr. Ali Hoshyaripour, der mich in seiner Gruppe aufgenommen hat und dank dem ich bei meiner Arbeit den Überblick behalten habe. Danke für eure Rückmeldungen sowie euer Korrekturlesen meiner Arbeit. Die Diskussionen mit euch haben mir immer weitergeholfen und ich konnte viel lernen.
Thank you also to the friendly group of students who shared the office with me, you made this time much more fun! Zu erwähnen sind natürlich auch die tollen Kommilitonen, die ich im Studium kennenlernen durfte, sowie mein Freund, meine Familie, meine Mitbewohner und sonstige Freunde für ihre beständige Unterstützung in dieser Zeit und auch immer sonst.

Erklärung

Ich versichere wahrheitsgemäß, die Arbeit selbstständig verfasst, alle benutzten Hilfsmittel vollständig und genau angegeben und alles kenntlich gemacht zu haben, was aus Arbeiten anderer unverändert oder mit Abänderungen entnommen wurde sowie die Satzung des KIT zur Sicherung guter wissenschaftlicher Praxis in der jeweils gültigen Fassung beachtet zu haben.

Karlsruhe, den 20.12.2024

(Tabea Unser)